POLITECNICO DI TORINO

College of Electronic Engineering, Telecommunications and Physics

Master of Science in Electronic Engineering

Master Thesis

Microwave Imaging Technology for Food Contamination Monitoring

Advisor:
Prof. Vipiana Francesca

Co-Advisors:
Prof. Casu Roberto Mario
Prof. Savorani Francesco

Candidate:
Alessandro Giordano

Academic year 2017-2018

A mio padre e a mia madre che mi hanno sostenuto e che hanno fatto fin troppi sacrifici per permettermi di terminare gli studi

A mio fratello e mia sorella per esserci

Alla mia fidanzata Sabrina che ha sempre creduto in me,

Alla sua famiglia che mi è stata vicino

A chi da lassù veglia sempre su di me

Al mio gruppo di cari amici del C.U.C. che ha condiviso con me le notti passate a studiare ed i giorni passati a giocare

Acknowledgements

I want to express my gratitude to my advisor and co-advisors to let me participate to this important project. Thanks to Dott. Tobon that has helped me so much and has answered to every mail of mine. They supported me with a lot of tips and ideas to continue my thesis work. I also want to thanks my friends that i've found at ISMB too, who had shared and made enjoyable the days working at our respective thesis.
Thanks to ISMB and Politecnico, which gave me the knowledge to be a better engineer and gave me the possibility to encounter many other interesting peoples.

Abstract

Nowadays food contamination is one of the major source of complaints against food manufacturers. Food is any substance used to provide nutritional support for the human body. On the other hand a foreign body is defined as an object that is not intended to be present. When food is contaminated, consumers lose faith in producers leading to a business decrease. With the rapid consumer's rising demand for safe food and better quality, food manufacturers work hard to eliminate foreign bodies. This is the reason why producers invest capitals in contamination detecting technologies, that are low cost, non destructive detection based and easy to embed into their production lines.
Food contaminations can include parts of packaging materials, such as plastic,metals, glass, or can derive from poor production conditions and chemical agents. Food hazard can be classified into[7]:

- physical hazards
- chemical hazards
- environmental pollution and human activity one

The constant application of rules that prevent foreign bodies presence helps to avoid incidents and so the consumer dissatisfaction. These are grouped under Good manufacturing practice[1] and Hazard Analysis and Critical Control Point[2] that represent the best way to cover food security[12] across all of its production steps. Unfortunately these aren't enough to ensure foreign bodies absence, so it has become necessary the introduction of technologies to detect its and isolate contaminated products.
Chosen detection and removal methodologies vary by foreign bodies types, which influence technical realization problems, costs and health consumer's risks. The most common separation techniques are based on the different physical or electrical properties between the intrusion and food. Detection, and any subsequent removal, processes are systems projected to identify a specific contaminant, based on electronic technologies to simplify it, reducing the costs and to speed up the entire revelation process in order to make it compatible with production line's speed and imposed reliability parameters.
The content of this thesis is centered on the simulations and laboratory test validation of a Microwave Imaging System applied on food safety problems, that provides non-destructive and contact-less real time analysis, completely safe for operators. The importance of it, it's underlined by the fact that foreign material inside food can lead some injuries to the clients and high compensation from the manufacturers.

Imaging technologies are based on the different dielectric properties of materials, in terms of conductivity σ and electric permittivity ϵ_r. σ factor conditions the field attenuation inside the medium, since the water content is higher then the attenuation will be stronger, representing

[1] GMP

[2] HACCP

the marmalade situation. On other hands the hazelnut cream has a low water content and it is ruled by oily behavior leading to a lower conductivity. Permittivity is a complex quantity, which real term (ϵ_r) defines the dielectric constant and imaginary term ϵ_i, the loss factor. Perhaps the dielectric constant defines the contrast between two different materials: higher is the ϵ_r difference, simpler the detection algorithm will discern them.

Microwaves are chosen because are totally safe for operators being low power and without ionizing radiations, which are source of safety food complaints.

The thesis focuses on applying the microwave imaging technology on orange marmalade and hazelnut cream jars, that showed two diametrically opposed behaviors, due to different water content, conditioning the EM waves penetration capability. Thesis work can be divided in the following main phases:

- Preprocessing steps where 3D CAD models and respective meshes are created;
- Full wave simulation with Finite Element Methods (FEM);
- Application of the reconstruction algorithm (TSVD) and 3D reconstruction/visualization;
- Laboratory testing at LACE;
- Ultra wide band monopole prototyping.

The system is composed by n antennae located around the target at fixed radius, depending on the considered monopole (12 for the narrow band monopoles, 6 and nearer for the UWB ones because bigger). An example is shown in the figure 1. Tetrahedral mesh, suitable for 3D

(a) LACE MWI system: target positioning

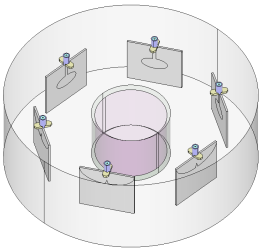

(b) 3D CAD example without inclusion

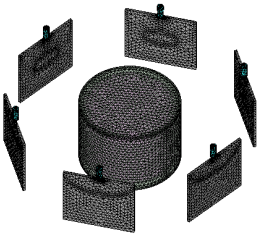

(c) Mesh example with background layer off

Figure 1

reconstruction, which dimensions are calculated in according to the higher working frequency and after the application of boundaries conditions, are then created and used to solve the propagation problem on each tetrahedron by FEM for each antenna, one in transmission and the others in reception, in the situation without inclusion and with it. These solutions are the propagating field inside the model and the scattering parameters. The reconstruction algorithm is based on the *truncated singular value decomposition (TSVD)*, a differential methods used to solve the inversion scattering reconstruction problem, starting from the field calculated in no inclusion situation and scattering parameters of the two cases, obtained before. The quality of the reconstruction depends on the number of considered antennae, which is a constrains on the acquired information quantity, and on the difference of the medium and inclusion permittivities. During the simulation analysis the TSVD inputs are obtained completely from FEM, while in experimental testing the scattering parameters are measured with the Vector Network Array (VNA). The generated TSVD output is

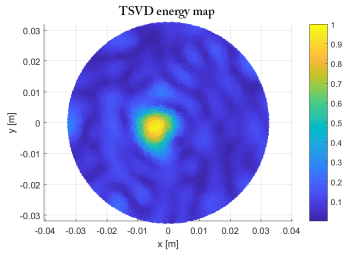

Figure 2: TSVD output example of correct detection

a normalized map plot where in ideal conditions, the peak position matches the inclusion location, as reported in figure(2). In order to increase the sensitivity and detection capability of the MWI system, an *ultra wide band antenna* with elliptic geometry, which simulated bandwidth extends to 3 GHz to $\approx$ 20 GHz is proposed (fig.3). Anyway because the higher water content of the marmalade, which didn't allow the field to penetrate, it wasn't possible make correct detection at frequencies higher than 3 GHz. While with the cream there was the need to increase the frequency to get correct detection. The results are pretty encouraging, but with a lower number

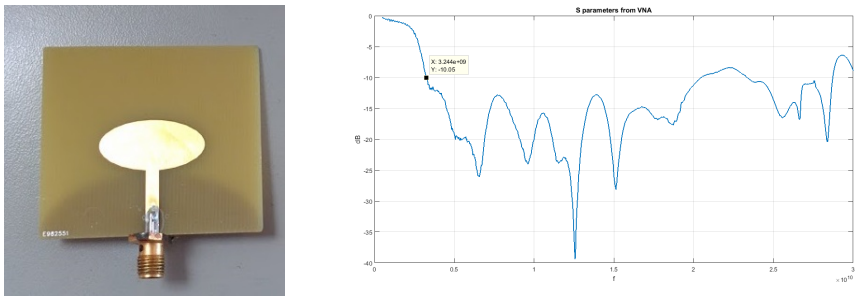

(a) Prototype of UWB antenna

(b) Measured S_{11} of the new antenna

Figure 3: Proposed monopole

of antennae, the detection quality decreases too much. So a brief study on the sub-sampling detection problem due to their low number is made, using the previous measured cases with more antennae. Here only the informations of some antennae were selected and the results gave the same errors in the detections. Also false-positive study was performed in order to give a feedback on the robustness and correctness of the detections. This analysis was made measuring the same jars at different times and two different jars. These results shown that to get the best results the antennae have to be in a number greater than 6 and with a good adaptation in the frequency range of interest.Throughout the thesis, the system showed encouraging capability during the simulation and the laboratory steps, despite the high noise level due to all the non ideal behavior of its components.

Future challenges will be the optimization of the entire system for integration on a real manufacture production line, producing a new antenna with suitable adaptation to work in the desired frequency range to increase the system sensibility.

Contents

Chapter 1

Introduction

Food quality management is becoming increasingly important because food manufacturers heaviest problem is the consumer complaints about foreign object in their products, that can lead severe implication both health users and foodstuff industry.

The growth of this incident type has made the consumer more aware about food quality, having as a consequence the technologies development for food safety. Together with this, it has been necessary a better contaminants classification in order to build ad-hoc detection systems.
There are a lot of contaminant types[13]such as:

- Wood
- Plastic
- Metal
- Glass
- Paper
- Animal/Plant origin
- etc

By the way they can have endogenous origin, that is part of the food itself, or an exogenous one, that are the introduced material during production steps, conservation and packaging. Earlier test methodologies were based on chemical and mechanical measurements usually time consuming, built on subjective and not well defined standards. Food safety and quality field was instead subject to expensive and invasive chemical analysis, impossible to perform in *loco* moreover without be destructive.
Up this moment, every analysis relied on the inspection of difference in properties such as weight, color, density, between food and potential foreign objects. However a lot of contaminants aren't detected yet. This problem is been partially solved with the introduction of new technologies and high capacity hardware processing and detection systems. So some parameters must be take into account:

- cost of the device

- users friendly and simple to add to the production line
- sensitivity of the detection
- capability to distinguish more contaminant
- speed, that is conditioned by the throughput of food line

Nowadays the majority of detection system uses electromagnetic waves measurements across specified region of the electromagnetic spectrum(Fig.1.1). In the literature[13],

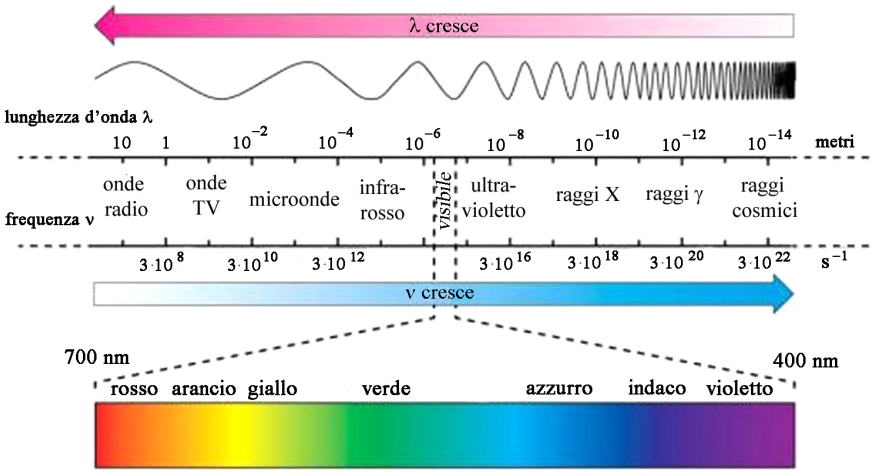

Figure 1.1: Electromagnetic spectrum

technologies are divided into two categories:

- On-line techniques → they can be used directly on site
- Off-line techniques → laboratories exclusive

1.1 Main imaging and detection techniques

In this paragraph the most common systems are presented in order to give information about imaging system state of the art.

1.1.1 Off-line techniques

Nuclear magnetic resonance

Nuclear magnetic resonance(NMR) is a non invasive method that measures the magnetic properties of spin under a magnetic field, that are related to the chemical proprieties of materials sample. The NRM signals are produced by the radiation absorption of the nucleus at a certain frequency. Under a magnetic field the average magnetic moment of many protons aligned themselves with its direction, then a small radio frequency impulse is briefly turned on, causing a variation on particle's spins. At its shutdown the protons

relaxation makes the spins returning at their original equilibrium. This relaxation produces a radio frequency signal used to generate the image, two or three dimensional based on how many fields were applied.

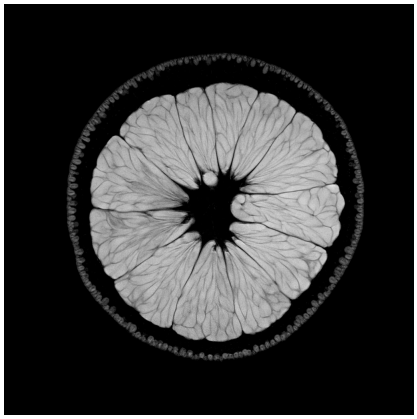

Figure 1.2: Orange MRN Imaging

The imaging is possible because every detected signals vary in terms of intensity and phase relying on the material proprieties. Due to the use of high magnetic fields, NMR industrial usage is conditioned by the high equipment costs.
Even though the precision of this method, the equipments cost and the temporal one are too much expensive.

Electronic microscopy

Microscopy uses an electron or light beam to scan a sample volume, which resolution comes down to type of microscope. Light usage has two main advantages:

- it's a not destructive method
- it is able to directly scan the object

Anyway light wave length imposes a physical limit to the minimal dimensions that considered foreign object can have(fig.(1.3)).

That's why the electronic beam is more efficiency. It allows nanoscale detection thanks to the smaller electron wave length, that is between 0.1Å and 0.005Å. When the sample surface is enlightened by the high energy electron beam, mainly two signals are produced by secondary and backscattering electrons.
Secondary electrons are defined as ones that come out from the object with an energy less than or equal to $50eV$. They are generated from the primary beam, backscatter particles and sample ones interaction. These electrons give information about surface topography, magnetic and electric field distributions, drawing a three-dimensional image.
Backscattering electrons are those with energy greater than $50eV$ and are generated from the interaction between beam and object atom's nucleus. So they collect data about average atomic number of the reflection region, topography and crystalline structure. These interaction products are collected by sensors and then processed to obtain the image. It's

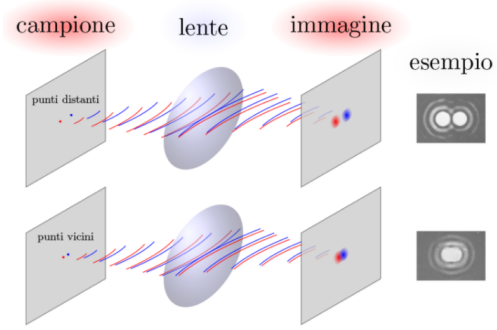

Figure 1.3: Resolution example: more the two points are close more the output image will be affected from the diffraction, that make them indistinguishable.

important that during the process the Unfortunately with this method only a small portion of the entire surface can be inspected.

Mass spectrometry

Mass spectrometry measures molecule characteristics, ionizing them with high energy electrons followed by their separation thanks to magnetic fields. This process makes possible to analyze sample spectrum weight$[m/Z]$, that is unique to it and quite accurate to give information about contaminants. The field effect is based on:

- ions or charge particles path can be modified by that field and the deflection is proportional to mass/charge ratio→ with the same charge, particles with lower mass will have a higher deflection.
- Accelerated ions or charge particles gain different speed based on their masses → with the same charge, higher mass atoms gain lower speed

The mass spectrum gives quantitative informations of sample's components, so it is used too detect its contaminants level.
The ionizing step classifies this technique as a destructive one and it is necessary work off-line in vacuum conditions to avoid the unwanted atmospheric gas effects. This make difficult using mass spectrometry in food manufacture.

Chromatography

Chromatography is a destructive method used to separate a mixture in its individual components. It is taking advantage that different substances move with different speeds into a mobile phase. It is used to separate chemicals components. For example a solid phase doesn't move into a liquid ones, making then the separation. Extracted informations identify the exact quantity of carbohydrate, lipids etc.., carry out too the right contaminant identification.
This process require a soluble sample, characterizing it as destructive, and specific laboratories equipment.

1.1.2 On-line techniques

X-rays imaging

The X-ray consolidation is due to its ability to inspect internal structure of food and organic tissues. This type of wave is characterized from a small wave length(around $\leq 10^{-9}m$) and an high energy, making them able to identify contaminants with different density and material. X-rays imaging is based on absorption and transmission of their energy through the sample. Image is produced thank to capability to run through organic material almost unchanged and not in high density, such as stones, insects, bones, metals, plastic, etc.. .
At the same time, because X-rays ionizing nature, there are some damage to molecular structures that can lead to organoleptic defects and healthcare problems for accidentally exposed operators. This aspect tells that X-rays should be used only for a small time interval in order to not get significant damage.

Raman spectroscopy

Raman spectroscopy is based on a monochromatic light beam and not elastic scattering. First of all the difference between the two type of scattering has to be listed:

- elastic scatter (*Rayleigh scattering*) doesn't have any variation in energy and frequency
- not elastic scatter gets some variations in energy and then in frequency, after the interaction with sample

When a surface reflects the light, not the entire wave experiences an elastic scattering, but there is a small portion that comes with a not elastic one. Photons are absorbed and re-emitted with variable frequency, different from the original, depending unpon the molecular structure and atomic mass of the object. This is called *Raman effect*. The difference in frequency comes from the specific vibrational state where the electron return after the virtual promotion due to the beam. Then the energy shift makes possible build a substance unique spectrum, that is used to identify structure, composition and contaminants of the material under test.
In conclusion it is a non destructive method with great accuracy, but it needs expensive equipment cost, that as always is an obstacle for manufactures utility.

Visual inspection

Visual control makes use of human operator to detect any defected object along the production line. It's important than to establish a standard , in order to be ready in case of food defects and expel it. The standard has to define the most important qualitative and quantitative characteristics that usually shall meet client requirements about aspects (forms, color...) and recipe's ingredients. This means constrains for packages, storage and transport condition too. Despite its simplicity, visual inspection doesn't have a great accuracy and it is resource expensive compared with offered results.

Optical techniques

This methods class uses a light beam that can be divided in four categories based on wave length:

- single wave length → it measures optical reflection at one wavelength
- different wave length → the reflection is measured using more frequency
- ratio measurements → it is based on two wavelength measures ratio
- combined measures of above mentioned ones

Limitations of this method are represented by the fact that only surface defects can be detected, greater wavelength usage can heats up food sample modifying its organoleptic proprieties and for different food material it needs different frequencies.

Infrared techniques

Infrared techniques are considered absorption spectroscopy based on different absorption modes of materials. This modes give information about the different elements which the food sample is composed. This methodologies, since infrared wavelength extends between $800\,nm$ and $2500\,nm$, are mainly used for organic compounds analysis, such as protein or grass content, and don't function with inorganic elements. Particular mention must be done to FT-IR spectroscopy[1], because is a more robust and precise method thanks to the memorization and Fourier transformation post-processing of collected data. As result the spectrum of sample content is obtained.
Its use is limited by the short penetration length due to the considered wavelength region and because infrared wavelengths are strongly absorbed by water blocking its fresh food field applications.

Hyperspectral imaging

Hyperspectral imaging(HIM) is a technique based on traditional spectroscopy and digital imaging to obtain detailed data on the entire chosen range of electromagnetic spectrum[7]. In this way it collects spatial and spectral information across various EM bandwidths, but high storage capabilities are needed. Obtained two or three-dimensional images are called *hypercubes* are data about each spatial position of the enlightened target, which are unique for every objects. So each position's spectra can be used to map the composition and the surface for its specific coordinates, making possible the detection of some defects.
HIM is a non destructive technique able to investigate large surface and it is very precise to identity organic components, stones, etc... , but as mentioned above, it produces a large amount of data which implies a large memory-storage consumption, that can be quite expensive.

Terahertz imaging

Terahertz technique[18] is a non invasive, non destructive technology, using non ionizing waves with frequency into the microwave and far-infrared region of the EM spectrum(0.3 to 3 THz). They are able to penetrate non conductive object and are very sensible to water

[1] Fourier transform infrared spectroscopy

contents that makes possible to use it in food and medical fields, because in that frequency range each of those materials gets a specific spectrum.
In this case a great obstacle for commercial use is the slow data elaboration, that can last until a minute for acquired bandwidth, because the presence across the acquisition path of some parasitic low-pass filters that slow the entire process. To make it faster with an acceptable signal to noise ratio, equipment costs must increase.
By the way the elevated instrumentation costs and the non-transparency of the water make difficult for manufactures to use this method.

Ultrasound imaging

Ultrasound imaging uses high frequency mechanical waves, usually above 20 kHz, region out of the audible human range, in order to exploit the difference in the acoustic impedance of different materials during its propagation[10][12], depending on its density and elastic properties. The acoustic impedance is defined as the ratio between acoustic pressure and vibrational speed of particles or can be defined as the product of density and sound velocity. It is based on mechanical transmission and reflection along various medium, because a variation in the wave energy means a change in the acoustic impedance caused by a different materials. This effect allows to detect foreign objects analyzing these discontinuities. Real time results can be obtained and can be used in production lines because it is classified as non-invasive and non destructive technology. There are four main categories for an acoustic wave:

- compressive → particles displacement is parallel to wave propagation
- shear → particles displacement takes place in any direction, but it is perpendicular to the propagation
- Rayleigh → displacement is only at the surface, cause the amplitude decreases exponentially with the depth
- Lamb → propagation leads only across a plane transverse dimension of about some millimeters

Their velocities are different and show high dependence on various physical, chemical factors and used with different aims. Rayleigh waves are used to find damage on a metallic surface, lamb ones on a thin sheet instead. Compressive wave are used to find the intrusion in solids, liquid and gas phase materials.
Ultrasound imaging can be used in real time detections, but each sensors shall be created ad hoc for the considered food sample to be effective and viable in its production line. This constrain can raises cost sensors.

Microwave imaging

Microwave imaging is a detection technique based on electromagnetic waves (*EM waves*) standing in frequency range between 10^{10} Hz and 10^{12} Hz. Mechanism is based on transmission across the food sample in order to exploit the local dielectric proprieties variation that means a foreign object detection. Microwave are low power and non ionizing signals

differently from similar X-ray technique, then more suitable for food applications. Traditionally a microwave imaging system is composed by hardware and software elements (example in figure (1.4)), where the first collects data and the second process them to generate the output.

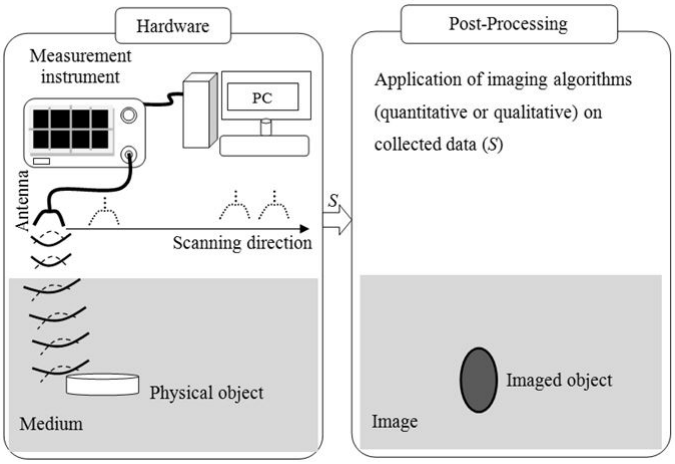

Figure 1.4: Example of single antenna microwave imaging system

Transmitted antenna generates EM waves toward the sample, that in food ambient it can be reasonably considered an homogeneous material, and a receiver antenna collects them. Greater is the difference in terms on proprieties of medium and foreign object, greater will be the reflected field towards the receiver antennae. Obtained data represents the field distribution into the sample, which resolution is directly proportional to the number of used antennae, depending on food proprieties and chosen frequency too. In addition the mutual inductance effect in near antenna should not be forgotten because can influence the received signal quality. After their acquisition a dedicated software processes the data to generate the outputs where the detected intrusion is reported.
Based on antenna, this method is non invasive and doesn't require any contact with the sample, that is important for an hygienic aspect and for the integrity of it too. There are two main approaches:

- tomography: it provides the dielectric profile of the object
- backscattering: it try to directly locate the intrusion position

Anyway the software part has to manage highly computational steps that consist in the resolution of a inverse, non linear and ill-posed scattering problem for which ad-hoc code is used. So microwave imaging is well suitable for food inspection because, as already written, doesn't require any contact and has the capability to identify a wide range of contaminants, if a minimal contrast is ensured.

1.2 Thesis focus

The content of my thesis describes modeling and simulation steps of a microwave imaging system for food inspection. The study is based on two type of foods:

1. oranges marmalade
2. hazelnuts cream

Water content of these two food samples will strongly influence the detection capability of the system, which resolution is depending from working frequency too, because, as later explained, it gives constrains to the foreign object minimal dimensions that can be detected. The study will start from an ideal and elementary model, where the jar is modeled as an entire full medium cylinder and the intrusion as a full air cylinder to get a well defined contrast, as in figure (1.5). Evaluated the correct functionality, the model is gradually complicated from making smaller the foreign objects, changing its material, introducing the jar thickness with its component, in relation to frequency change.

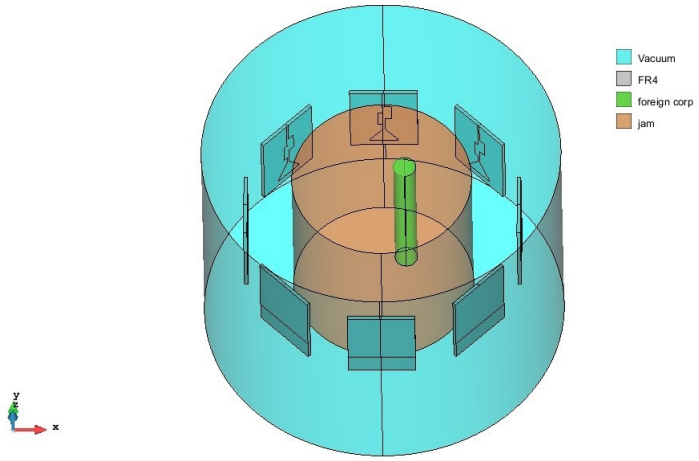

Figure 1.5: Starting three-dimensional model

The system approach is a backscattered one with the aim to reconstruct the intrusion position starting from the internal electromagnetic fields of the sample in the *gold case*, with no intruder, and the scattering parameters of cases with and without the intrusion. The following is a software elaboration of their difference using a reconstruction imaging algorithm. The correct detection is obtained when wavelength of microwave is comparable with dimension of the foreign object and it gets enough penetration depth to carry to the receiver antennae the right information amount. This is possible when the material is characterized by a not high water contents, which increases the fields attenuation, and from the presence of difference between the dielectric proprieties.
The project sees the model creation using GiD[8], where each component of the system is described with its material and boundary conditions to get the correct simulation. Here a tetrahedral mesh, with order dimension of about $\lambda/15$, defined from the material permittivity at chosen frequency. $\lambda/15$ is been chosen because it can ensure to get a correct

evaluation of every propagation problem applied from a *finite element method* to find field into the system.
Next step involves the solution of the propagation problem with the finite element method (FEM), which aim is to resolve Maxwell equation for the unknowns, that are the tetrahedrons. Each field for every antenna is saved to .VTK extension file. This type of file can be read using a reader called Paraview[29] where fields of the system can be seen.
The software processing is assigned to MATLAB[24]. Used algorithm is the truncated singular value decomposition (TSVD), which generates, starting from fields and scattering parameters, an energy map where in case of foreign object detection a maximum is located, that as free property of the system, matches its position(showed in figure (1.6b)).

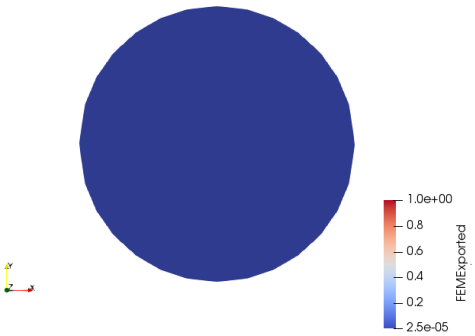

(a) FEM output file visualization in case of no foreign object

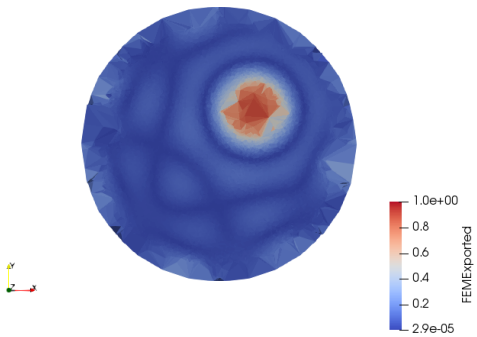

(b) TSVD output file visualization in case of detection

Figure 1.6: FEM and reconstructed TSVD output examples

The system study is started using a narrow band monopole because already available in laboratory. However to increase the capacity and particularly the resolution of the system, higher frequencies are needed and with this aim an ultra wide band antenna has been proposed. Higher frequencies are needed because smaller is the intruder smaller should be the wavelength. That antenna has been singularly and into the MWI system modeled and simulated, before its production.
Finally laboratory tests are been performed using an available prototype, that have validated simulations, giving excellent results.

1.3 Thesis outline

This thesis is divided in some main topics, including the microwave imaging technologies brief presentation, electromagnetic main principles descriptions and used tools, the CAD design and ultra wide band antenna project and simulation, the system simulations and the laboratory tests, ending with the conclusion and future improvements.

The first chapter describes the main imaging and detection technologies. Chapter 2 and 3 defines the basics theory of electromagnetism and electromagnetic properties useful

to understand the presented microwave imaging technologies. In chapter 4 the system and ultra wide band antenna modeling are described. Chapters 5 and 6 briefly describe the finite element method utilized to simulate the propagation problems and the TSVD algorithm used to solve the inverse scattering problem to reconstruct the detection, with some proposed calibration methods and a multi-frequencies approach to its resolution. Chapter 7 contains the simulations results, exploring the orange marmalade and hazelnut cream, at various frequencies and with different inclusions, gradually complicating the model. Chapter 8 resumes the laboratory prototype tests with different inclusions and number of antennae in order to evaluate the system capabilities in real situations. In Chapter 9 a brief study of the implications of a too lower monopoles number have on the detection. Inside the appendix A is reported the code optimization on reading the field FEM outputs, in B the false positive test is performed in order to understand if the detection are surely correct and in C a three dimensional reconstruction of a sample case is described. Finally the conclusion is given in its respective chapter.

Chapter 2

Electromagnetic fields

In this chapter some electromagnetic fields hints are reported, such as quantities ed fundamental equations that rule their behavior. Electromagnetic field theory is a science that studies charges, at rest and in motion, currents and electric/magnetic fields.

2.1 Basis of electromagnetism

In electromagnetism every equation and quantity is based on the field concept. It is a set of rules and variables that define a quantity behavior in a space region. Every points of it can be experimentally measured of mathematically obtained. So a lot of scalar and vectorial equations are defined to describe the quantities in a reference domain, that are listed in tabular (2.1), (2.2) e (2.3).

Table 2.1: Some electromagnetic quantities

Symbol	Quantity	Unit	Short
Y	admittance	siemen	S
ω	angular frequency	radiant/second	rad/s
C	capacity	farad	F
ρ	charge density	coloumb/meter^3	C/m^3
G	conductance	siemen	S
σ	conductivity	siemen/meter	S/m
W	energy	joule	J
F	force	newton	N
f	frequency	hertz	Hz
Z	impedance	hom	Ω
L	inductance	henry	H
μ	permeability	henry/meter	H/m
ϵ	permittivity	farad/meter	F/m

Table 2.2: Some scalar and vectorial quantities

Variable	Definition	Typology	Unit
$\vec{A}$	magnetic potential vector	vector	Wb/m
$\vec{H}$	magnetic intensity	vector	A/m
$\vec{B}$	magnetic flux density	vector	Wb/m^2 (T)
$\vec{D}$	electric flux density	vector	C/m^2
$\vec{E}$	electric field intensity	vector	V/m
$\vec{F}$	Lorentz field	vector	N
I	electric current	scalar	A
$\vec{J}$	current density	vector	A/cm^2
q	free charge	scalar	C
$\vec{S}$	Poynting vector	vector	W/m^2
$\vec{u}$	free charge velocity	vector	m/s
V	electric potential	scalar	V

Table 2.3: Partial list of principal equations

$\vec{D} = \epsilon\vec{E}$	permittivity (ϵ)
$\vec{B} = \mu\vec{H}$	permittivity (μ)
$\vec{J} = \sigma\vec{E}$	conductivity (σ) Ohm law
$\vec{F} = q(\vec{E} + \vec{u} \times \vec{B})$	Lorentz force equation
$\nabla\vec{D} = \rho$	Gauss law I
$\nabla\vec{B} = 0$	Gauss law II
$\nabla\vec{J} = -\frac{\partial\rho}{\partial t}$	continuity equation
$\nabla \times \vec{E} = -\frac{\partial\vec{B}}{\partial t}$	Faraday law
$\nabla \times \vec{H} = \vec{J} + \frac{\partial\vec{D}}{\partial t}$	Ampère law

Furthermore the material characteristics must been considered, that in a vacuum space are:

$\mu_0 = 4\pi * 10^{-7}$ H/m

$\epsilon_0 = 8{,}851 * 10^{-12} \approx 10^{-9}/36\pi$ F/m

$c = (\mu_0\epsilon_0)^{-\frac{1}{2}} \approx 3 \cdot 10^8$ m/s

where c is the field propagation velocity in vacuum equals to the light's one.

2.1.1 From magnetostatic and electrostatic to electrodynamic

The theory that describes the relation between physical phenomenas, stationary charge and charge space distribution is called *electrostatic*. This part of EM theory is based on some hypothesis:

- charges fixed in space region

- charge densities are constant in time
- charge itself is the field source

Its aim is to evaluate the field intensity for each domain point, interaction force between particles, the electric and potential energy distribution using for example equations listed in table(2.4).

Table 2.4: electrostatic principle equations

Coulomb law	$\vec{F} = q\vec{E}$
Electric field	$\vec{E} = \frac{Q\vec{a_R}}{4\pi\epsilon R^2}$ o $\vec{E} = \frac{1}{4\pi\epsilon}\int_v \frac{\rho\vec{a_R}}{R^2}dv$
Gauss law	$\nabla\vec{D} = \rho$ o $\oint_s \vec{D}\vec{ds} = Q$
Electric field conservativity	$\nabla \times \vec{E} = 0$ o $\oint_c \vec{E}\vec{dl} = 0$
Potential	$\vec{E} = -\nabla V$
Poisson equation	$\nabla^2 V = -\frac{\rho}{\epsilon}$
Laplace equation	$\nabla^2 V = 0$
Ohm law	$\vec{J} = \sigma\vec{E}$
Constitutive relation	$\vec{D} = \epsilon\vec{E}$

Starting point for the electrostatic is the Coulomb law that rules the interaction between charge particle(see figure 2.1), expressed as[41] in eq.(2.1) where $|x - x'|$ is the particles distance.

$$F(x) = \frac{qq'}{4\pi\epsilon_0}\nabla'\left(\frac{1}{|x - x'|}\right) \tag{2.1}$$

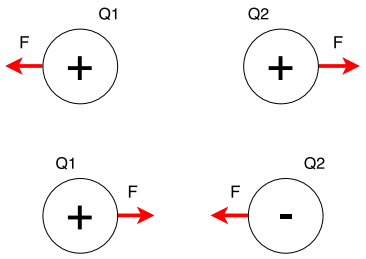

Figure 2.1: Coulomb law: it describes interaction between charge particles

Obtained Coulomb force formulation the static electric field is given by

$$E^{static} = \lim_{q\to 0}\frac{F}{q} \tag{2.2}$$

Another field type is the magnetic one, defined as the interaction generated by charges with constant velocity, which are known as current. It is studied by the so called *magnetostatic*. By the way it has a similar aim: to define intensity, flux of that fields using its equations(2.5)[41].

Table 2.5: Magnetostatic main equations

Electromagnetic force	$\vec{F} = q\vec{u} \times \vec{B}$
Bios-Savart law	$d\vec{B} = \frac{\mu}{4\pi}\frac{I\vec{dl}\times\vec{a}_r}{r^2}$
Ampère law	$\nabla\vec{H} = \vec{J}$ o $\oint_c \vec{H}\vec{dl} = I$
Gauss law	$\nabla \cdot \vec{B} = 0$ o $\oint_s \vec{B}\vec{ds} = 0$
Magnetic potential	$\vec{B} = \nabla \times \vec{A}$ o $\vec{A} = \frac{\mu}{4\pi}\int_c \frac{I\vec{dl}}{r}$
Magnetic flux	$\phi = \int_s \vec{B} \cdot \vec{ds}$ o $\phi = \oint_c \vec{A} \cdot \vec{dl}$
Poisson equation	$\nabla^2\vec{A} = -\mu\vec{j}$
Constitutive relation	$\vec{B} = \mu\vec{H}$

In this case the analysis starting point for magnetic calculation is the Ampère law stated as

$$F(x) = \frac{\mu_0 II'}{4\pi}\oint_C dl \times \oint_C' dl' \times \frac{(x-x')}{|x-x'^3|} = I\oint_C dl \times B^{static}(x) \tag{2.3}$$

Together with the electrostatic, since studies of dynamic field have to be done, the *electrodynamics* should be introduced. This union can be summarized as[41]

- electrical charge movement generates the current and the charge is a conservative variable →it becomes displacement current in Maxwell equations
- an electromagnetic field is induced in a coil when a variation of the magnetic field takes place → Faraday law

2.2 Maxwell equations

Introduced electric and magnetic field, their variations and associated quantities are stated by the four *Maxwell equations*. They come with two formulation: differential, that is more used, and integral.
The differential form(table below) is used in electromagnetic boundary problems to describe quantities in every points of the domain.

Coulomb or electric Gauss equation	$\nabla \cdot E = \frac{\rho_e}{\epsilon_0}$
Farady law	$\nabla \times E = -\frac{\partial B}{\partial t}$
Magnetic Gauss equation	$\nabla \cdot B = \frac{\rho_m}{\mu_0}$
Ampère law	$\nabla \times B = \epsilon_0\mu_0\frac{\partial E}{\partial t} + \mu_0 j_{total}(t,x)$

Table 2.6

In that table ρ represents the total electric or magnetic charge and $j(x,t)$ the electric current density. Every quantity is assumed to be time varying and function of space and

time. Anyway they can't be used to described discontinuity in fields unless *boundary conditions* are applied. So these equations can completely describe the fields with initial and boundary conditions of the under test domain.
Integral form of Maxwell equations([**?**]) is usually used for symmetric electromagnetic problems only, but in this case field can have discontinuous distributions.

Electric Gauss equation	$\oint \vec{E} \cdot d\vec{A} = \frac{q}{\epsilon_0}$
Farady law	$\oint \vec{E} \cdot d\vec{s} = -\frac{d\Phi_B}{dt}$
Magnetic Gauss equation	$\oint \vec{B} \cdot d\vec{A} = 0$
Ampère law	$\oint \vec{B} \cdot \vec{ds} = \mu_0 i + \frac{1}{c^2} \frac{\partial}{\partial t} \int \vec{E} \cdot d\vec{A}$

Constitutive equations should be considered when medium has not negligible effects on the electromagnetic fields, because it can influences polarizations and conduction. They are expressed as:

1. $D = \epsilon E \rightarrow$ time domain relation between electric flux density D and electric field
2. $B = \mu H \rightarrow$ time domain relation between magnetic flux density B and magnetic field
3. $J_{conduction} = \sigma E \rightarrow$ current density proportional to the electric field through the conductivity

where ϵ is the permittivity, μ the permeability of the medium and σ the conductivity. These parameters generally describe material dielectric proprieties that are function of frequency and material type. If they are constant across the media, it can be defined as homogeneous. That is the case of analyzed oranges marmalade and hazelnut cream.

The first constitutive equation takes into account the electric polarization, that is the effect on medium molecules caused by an electric field. The second is used to represent the magnetization, which is the magnetic field effect on the medium. Last one represents the electric conduction, that happens in a material when there are free charges.

2.2.1 Boundaries conditions

As already written, differential form of Maxwell equations can' t be used in discontinuous fields problems, that may take place on interface between two materials(called for simplicity 1 and 2) with different dielectric proprieties. Then integral form of Maxwell equation can be used to derive it[21][4].
Let's take an interface between two material and a rectangular box that cross them, with dimension Δx and Δy, which will lead ideally to 0, because there is only interest along the interface. In that case the following integral can be written:

$$\oint_{C_0} E dx = -\frac{\partial}{\partial y} \iint_{S_0} B ds \tag{2.4}$$

where C_0 is the box perimeter and S_0 its surface. Making Δy smaller, the surface also becames much minimal that the surface integral is negligible, obtaining:

$$E_1 \cdot \hat{a_x}\Delta x - E_2 \cdot \hat{a_x}\Delta x = 0 \tag{2.5}$$

$$E_{1t} - E_{2t} = 0 \Rightarrow E_{1t} = E_{2t} \tag{2.6}$$

The electric field boundary condition is

$$\hat{n} \times (E_2 - E_1) = -M_s \quad \text{with } M_s \text{ as surface magentic current density} \tag{2.7}$$

which explain that the tangential component of the electric field on interface surfaces, in case no magnetic current, is continuous.
The magnetic condition is carry out in the same manner obtaining:

$$\hat{n} \times (H_2 - H_1) = J_s \quad \text{with } J_s \text{ as surface electric current density} \tag{2.8}$$

explaining that tangential components of magnetic fields, on an interface where no perfect conductors are used, are continuous.
There are also boundaries condition for normal components of fields which are summarized as:

$$\hat{n} \cdot (D_2 - D_1) = q_{es} \rightarrow \text{normal component of electric flux density is continuous} \tag{2.9}$$

$$\hat{n} \cdot (\epsilon_2 E_2 - \epsilon_1 E_1) = 0 \rightarrow \text{normal component of electric field is discontinuous} \tag{2.10}$$

$$\hat{n} \cdot (B_2 - B_1) = q_{ms} \rightarrow \text{normal component of magnetic flux density is continuous} \tag{2.11}$$

$$\hat{n} \cdot (\mu_2 H_2 - \mu_1 H_1) = 0 \rightarrow \text{normal component of magnetic field is discontinuous} \tag{2.12}$$

It's important introduce the case when a medium is a perfect electric conductor (PEC), meaning that on its surface can be surface electric charge and current. Then equations (2.7), (2.8), (2.9), (2.11) become

$$\hat{n} \cdot (D_2 - D_1) = \rho_{es} \tag{2.13}$$

$$\hat{n} \times (E_2 - E_1) = 0 \tag{2.14}$$

$$\hat{n} \cdot (B_2 - B_1) = 0 \tag{2.15}$$

$$\hat{n} \times (H_2 - H_1) = J_s \tag{2.16}$$

2.3 Electromagnetic wave equations

Solving Maxwell equation, electric and magnetic wave equation can be obtained.

2.3.1 Electric field wave equation

This equation is obtained starting from Faraday law rotor and Ampère law:

$$\nabla \times (\nabla \times E) = -\frac{\partial(\nabla \times B)}{\partial t} = -\mu_0 \frac{\partial(j + \epsilon_0 \frac{\partial E}{\partial t})}{\partial t} \tag{2.17}$$

It should be noted that

$$\nabla \times (\nabla \times E)) = \nabla(\nabla \cdot E) - \nabla^2 E$$

where $\nabla \cdot E = 0$ since $\rho = 0$ and writing $E * \Delta V = 0$(ΔV is the electromotive force: electric potential difference), Ohm law becomes:

$$j = \sigma E \tag{2.18}$$

As a consequences the equation(2.17) is rewritten as

$$\nabla^2 E - \mu_0 \frac{\partial(\sigma E + \epsilon_0 \frac{\partial E}{\partial t})}{\partial t} = 0 \tag{2.19}$$

and making the right substitutions the *homogeneous electric field wave equation* is obtained in eq.(2.20).

$$\nabla^2 E - \mu_0 \sigma \frac{\partial E}{\partial t} - \frac{1}{c^2} \frac{\partial^2 E}{\partial t^2} = 0 \tag{2.20}$$

2.3.2 Magnetic field wave equation

Magnetic field wave equation is obtained following the same steps:

$$\nabla \times (\nabla \times B) = \mu_0 \nabla \times j + \epsilon_0 \mu_0 \frac{\partial(\nabla \times E)}{\partial t} = \mu_0 \sigma \nabla \times E + \epsilon_0 \mu_0 \frac{\partial(\nabla \times E)}{\partial t} \tag{2.21}$$

Knowing that $\nabla \cdot B = 0$ for every medium and substituting in eq.(2.21), the *homogeneous magnetic field wave equation* is obtained:

$$\nabla^2 B - \mu_0 \sigma \frac{\partial B}{\partial t} - \frac{1}{c^2} \frac{\partial^2 B}{\partial t^2} = 0 \tag{2.22}$$

Time invariant wave equations notation

Now that field are defined as functions of space (x,y,z) and time, usually it is preferable use an exponential notation related to the frequency ω:

$$E = E_0(x, y, z) e^{-i\omega t} \tag{2.23}$$

where $E_0(x, y, z)$ is the spatial dependence and $e^{-i\omega t}$ the temporal one.

Considering for simplicity the x variable, the expression (2.23) can be write in (2.20) to get

$$\nabla^2 E_0(x)e^{-i\omega t} - \mu_0\sigma\frac{\partial E_0(x)e^{-i\omega t}}{\partial t} - \frac{1}{c^2}\frac{\partial^2 E_0(x)e^{-i\omega t}}{\partial t^2} \tag{2.24}$$

$$=\nabla^2 E - \mu_0\sigma(-i\omega)E_0(x)e^{-i\omega t} - \frac{1}{c^2}(-i\omega)^2 E_0(x)e^{-i\omega t} \tag{2.25}$$

$$=\nabla^2 E - \mu_0\sigma(-i\omega)E - \frac{1}{c^2}(-i\omega)^2 E \tag{2.26}$$

$$=\nabla^2 E + \frac{\omega^2}{c^2}\left(1 + i\frac{\sigma}{\epsilon_0\omega}\right)E = 0 \tag{2.27}$$

Introducing the *relaxation time* in the medium as

$$\tau = \epsilon_0\sigma$$

the result is

$$\nabla^2 E + \frac{\omega^2}{c^2}\left(1 + \frac{i}{\tau w}\right)E = 0 \tag{2.28}$$

which for $\tau \to \infty$ is simplified as

$$\nabla^2 E + \frac{\omega^2}{c^2}E = 0 \tag{2.29}$$

Equation (2.29) defines the *electric wave equation* with no dependence from time.

Instead if *tau* is small enough, it is obtained the *diffusion equation of the electric field.*

$$\nabla^2 E + i\omega\mu_0\sigma E = 0 \tag{2.30}$$

With same steps equations of magnetic field can be found:

$$\nabla^2 B + i\omega\mu_0\sigma B = 0 \tag{2.31}$$

2.3.3 General solution for the wave equation

Defining[21] the propagation constant as

$$\gamma^2 = j\omega\mu(j\omega\epsilon + \sigma) \tag{2.32}$$

and considering

$$\nabla \times E = -j\omega\mu H \tag{2.33}$$

$$\nabla \times H = j\omega\epsilon E + \sigma E \tag{2.34}$$

each component of them satisfies the Helmholtz equation, that for a single coordinate can be written as

$$\nabla^2 E_x - \gamma^2 E_x = 0 \tag{2.35}$$

The solution for this equation is obtained by separation of variables method, getting for the electric field

$$E(r) = E_0 e^{\pm \gamma r} \tag{2.36}$$

and for the magnetic field

$$B(r) = B_0 e^{\pm \gamma r} \tag{2.37}$$

where

$r = x\hat{x} + y\hat{y} + z\hat{z}$

$\gamma = \gamma_x \hat{x} + \gamma_y \hat{y} + \gamma_z \hat{z}$

However γ can be written as $\alpha + j\beta$ vectors, which can define the type of wave:

- if α and β have the same direction, it is an uniform plane wave
- if α and β don't have same direction, it is a non uniform plane wave

To generalize equations (2.36) and (2.37), linear superposition of all possible solutions can be applied leading to

$$E(r) = \int_{-\infty}^{+\infty} \int_{-\infty}^{+\infty} E_0(\gamma_x, \gamma_y) e^{\pm \gamma r} d\gamma_x d\gamma_y \tag{2.38}$$

$$H(r) = \int_{-\infty}^{+\infty} \int_{-\infty}^{+\infty} H_0(\gamma_x, \gamma_y) e^{\pm \gamma r} d\gamma_x d\gamma_y \tag{2.39}$$

So it's important define the quantities that are to be considered with an electromagnetic waves:

- period T
- wavelength λ
- velocity $v = \frac{\lambda}{T}$
- wave number $k = \frac{2\pi}{\lambda}$
- frequency $f = 1/T$ and $\omega = 2\pi f$

In addition the *wave impedance* must be introduced as the electric and magnetic field ratio:

$$Z_w = \frac{|E|}{|B|} = \frac{\omega\mu}{\beta} = \frac{\beta}{\omega\epsilon} = \sqrt{\frac{\mu}{\epsilon}} \tag{2.40}$$

where β is the phase constant.

2.3.4 Wave velocity and attenuation

Considering a plane wave propagating in a vacuum space without any losses, its propagation velocity is exactly the one of light $\approx 3 * 10^8[m/s]$. The phase velocity, that is a measure plane wave movement calculated as:

$$v_p = \frac{\omega}{\beta} \tag{2.41}$$

where in this case $\beta = \omega\sqrt{\mu\epsilon}$.
Anyway considering a loss conduction material the propagation constant becomes $\gamma = \alpha + j\beta$ where

$$\alpha = \omega\sqrt{\frac{\mu\epsilon}{2}}\sqrt{\sqrt{1+\left(\frac{\sigma}{\omega\epsilon}\right)^2}-1} \tag{2.42}$$

$$\beta = \omega\sqrt{\frac{\mu\epsilon}{2}}\sqrt{\sqrt{1+\left(\frac{\sigma}{\omega\epsilon}\right)^2}+1} \tag{2.43}$$

where α is the attenuation parameter and β the constant phase.

Propagation quantities

During the wave propagation its magnitude is attenuated because material losses. So The propagation constant (eq.(2.32)) can be defined also as the following equation:

$$\gamma = \sqrt{(R + j\omega L)(G + j\omega C)} = (-)\alpha + j\beta \tag{2.44}$$

Attenuation sources include a lot of element such as:

- conductor losses (skin effect)
- dielectric losses
- hysteresis losses
- mismatch between materials
- radiation losses

The first three sources absorb energy by definition, while the lasts are due to propagation reflection in case of discontinuities between different materials. An important parameter to take in consideration when thinking at electromagnetic wave reflection is the *VSWR*, *Voltage standing wave ratio*, expressed as the maximum and the minimal wave voltage ratio, which describes the mismatch.

$$VSWR = \frac{|V_{max}|}{|V_{min}|} = \frac{1+\rho}{1-\rho} = \frac{1+\Gamma}{1-\Gamma} \tag{2.45}$$

In this equation each of these parameters has real and imaginary part. As written in eq.(2.45), it can be also expressed with a coefficient reflection dependence Γ. Talking

about wave power another quantity can be defined: the *power standing wave ratio*, $PSWR$, useful to refer waves with a power view point.

$$PSWR = \sigma^2 \tag{2.46}$$

Information about losses of propagating wave is provide from the *return loss*

$$return\ loss[dB] = -20\log(\rho) \tag{2.47}$$

with $\rho = \frac{VSWR-1}{VSWR+1}$.
Instead the *mismatch loss* describes the irradiated power absorbed from a termination, that for example it can be an antenna.

$$mismatchloss[dB] = -10\log(1-\rho^2) \tag{2.48}$$

2.3.5 Skin depth

Taking about propagation, the skin effect has to be introduce. It is the phenomena that explains because at higher frequencies the current seeks to flow on the surface proximity, decreasing it inside. This effect is due to the electromagnetic induction (Lenz law), thereby a variable magnetic field is always coupled with an induced electric field. This field generates a variable current and a magnetic field. This last induced field is opposed to the original field, decreasing the total one(figure(2.2)).

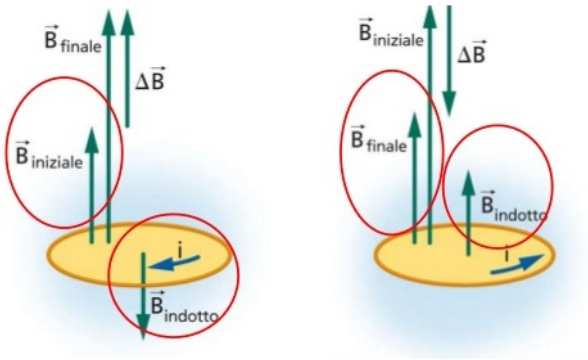

Figure 2.2: Lenz law

For instance, a semi-infinite plane is considered with extension from z=0 to z=∞, the field can be written as:

$$E(z) = E_0 e^{-\gamma z} \tag{2.49}$$

which exponentially decreases towards the propagation direction because the attenuation, that points out the penetration capability of the field inside the material. It depends on the frequency, dielectric properties fo the medium.

$$|E| = E_0 e^{-\alpha z} \tag{2.50}$$

With aim to better describe field penetration, penetration depth, *delta* is introduced. It is defined as the depth where the absolute value of the field is attenuated to $1/e \approx 0.37$ of its superficial value. Considering a plane wave the absolute value of the field is described from the equation (2.50), while the depth parameter is

$$\sigma = \frac{1}{\alpha}$$

Hiigh losses materials, characterized by a small δ, the field decrease is so fast to nto be able to penetrate the medium. By the way for lower losses materials, with higher δ, the penetration capability will be higher.

In microwave application refers usually to power, so the *power penetration depth*, δ_p can be introduced. It is defined as the depth where the wave power decreases at $1/e$ times respect of its surface value. The power is expressed by:

$$Q = \frac{1}{2}\omega\epsilon_0\epsilon_{eff}^N|\hat{E}_0|^2e^{-2\alpha z} = Q_0e^{-z/\delta_p} \tag{2.51}$$

$$\delta_p = \frac{1}{2\alpha} = \frac{\delta}{2} \tag{2.52}$$

where Q_0 is the surface density power and δ_p the power penetration depth.
Usually food isn't made of magnetic materials ($\mu_r = 1$), so the equation (2.42) can be simplified and using it in (2.52), it is obtained:

$$\delta_p = \frac{c}{\omega\sqrt{2\epsilon'}(\sqrt{1+(\epsilon''/\epsilon')^2}-1)^{1/2}} \tag{2.53}$$

It's important to note that these equations are valid in case of sample dimensions quite bigger than the penetration depth. When the two quantities can be compared the field distribution doesn't decrease exponentially because resonance effects.

2.3.6 General behavior of incident waves

Incident wave are defined as those that have an "impact" on a surface. As a consequence portion of its energy is reflected and another is transmitted inside the material by the Snell law(fig.(2.3)).

$$\sin\theta_t = \sin\theta_i\frac{n_i}{n_r} = \sin\theta_i\frac{\sqrt{\mu_1\epsilon_1}}{\sqrt{\mu_2\epsilon_2}} \tag{2.54}$$

$$\theta_r = \theta_i \tag{2.55}$$

Snell law explains that a plane wave with an incident angle θ_i with the electric field parallel to the surface, it is transmitted through the material and refracts with a θ_r angle.

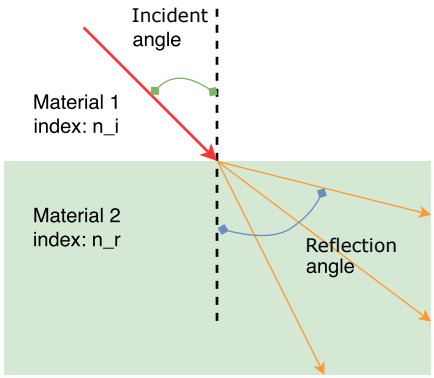

Figure 2.3: Snell representation. Wave reflection and transmission.

n_i and n_r are the refractive index of the materials, which electromagnetically talking are the electric permittivity. Also the reflection coefficient of an electric field is calculated by Fresnel law as

$$\Gamma = \frac{E_r}{E_i} = \frac{\sqrt{\epsilon_r}\cos\theta - \sqrt{\epsilon_r}\cos\phi}{\sqrt{\epsilon_i}\cos\theta + \sqrt{\epsilon_i}\cos\phi} \tag{2.56}$$

Furthermore the power is proportional to the square of field, the transmitted power inside the material is:

$$|T| = 1 - |\Gamma|^2 \tag{2.57}$$

An important case is the incident angle equal to the *Brewster angle*, that is the value where the surface reflection is nulled and incident wave is entirely transmitted inside the domain.

2.4 Propagation mode

Propagation inside a material is influenced by dielectric proprieties of it and the wavelength of the field, which is inversely proportional to its frequency. At the point where it is comparable with the wavelength of line dimension, more propagation mode can take place. Main mode transport energy at all frequencies range, while the upper order ones have got energy only at certain frequencies. Their propagation frequencies are called *cut-off frequency*.

Considering for example parallel transmission lines, while there is a voltage difference, there is an electric field too. At the same way, while there is a current, a magnetic field also exists. Their main characteristic is the fact that they are perpendicular and transversal to the propagation direction. These wave are called *transversal electromagnetic wave*, with propagation mode *TEM*.

As already written, increasing the frequency, propagation mode with at least one component along the propagation increases in number too. BAsed on the component parallel to the movement, they are defined as wave propagation H or E. It is type H if at least one component of the magnetic field is along the propagation (*transversal electric mode ,*

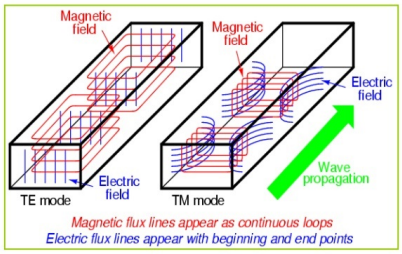

Figure 2.4: Example of propagation mode of electric and magnetic fields

TE), on the other hand if the component is one the electric field it is type E, *magnetic transversal mode, TM* .

Chapter 3

Food electromagnetic properties

Food electromagnetic properties are known as dielectric properties, that have high importance in studying the interaction between electromagnetic fields and the materials. These parameters, with the field characteristics, physical and chemical ones, have high impact on the propagation inside the medium. For example in a microwave frequencies range, considering a high water content material such as the orange marmalade, the penetration is simpler at low frequencies, but harder at higher because water content, but if it is much smaller, that's the case of hazelnut cream, the penetration need higher frequency to be acceptable.
Each of these parameters can be a constrains for a microwave imaging system project, varying the interaction, the penetration capability, the resolution and the working frequency.

3.1 Basic principles

3.1.1 General dielectric properties

Dielectric properties measure the interaction between material and the electromagnetic field. The most important parameter is the relative complex permittivity ϵ_r given by[11]

$$\epsilon_r = \epsilon' - j\epsilon'' \tag{3.1}$$

where ϵ' is known as the dielectric constant and ϵ'' as the dielectric loss factor (real and imaginary part respectively), or it can be written as

$$\epsilon_r = |\epsilon_r| e^{-j\delta} \tag{3.2}$$

where δ is the dielectric loss angle. In addition the loss tangent, the dissipation factor $\tan\delta$ is defined as

$$\tan\delta = \frac{\epsilon''}{\epsilon'} \tag{3.3}$$

There is also the absolute permittivity in a void space ϵ_0 that is determined by light speed c_0 and magnetic constant μ_0:

$$c_0^2 \mu_0 \epsilon_0 = 1 \tag{3.4}$$

The conductivity, σ, of the dielectric is related to the loss factor by

$$\sigma = \omega \epsilon_0 \epsilon'' \ \ [S/m] \tag{3.5}$$

where $\omega = 2\pi f$ is the angular frequency $[rad/s]$.

The dielectric constant represents the material capacity to store electric energy, influencing the field propagation. In vacuum it is assumed to be 1. The imaginary component of the permittivity describes the energy dissipation in the medium characterizing the wave attenuation. In a material without losses it is considered 0.
So the dielectric proprieties are constrains on the behavior of microwave fields inside the materials. A measure of it is the power dissipation per unit volume that is written as:

$$P = \sigma E^2 = 55.63 f \epsilon'' E^2 \times 10^{-12} \ \ [W/m^3] \tag{3.6}$$

Obtained the dielectric properties the penetration depth (introduced in equation (2.52)) can be calculated too and in case of non magnetic material it is simplified as

$$\delta_p = \frac{\lambda_0}{2\pi\sqrt{2\epsilon'}} \left[\sqrt{1 + \left(\frac{\epsilon''}{\epsilon'} \right)^2} - 1 \right]^{-\frac{1}{2}} \text{where } \lambda_0 \text{ is the wavelength in vacuum} \tag{3.7}$$

Considering instead a low losses material $\frac{\epsilon''}{\epsilon'} \ll 1$, the penetration depth can be again simplified in

$$\delta_p = \frac{\lambda_0 \sqrt{\epsilon'}}{2\pi\epsilon''} \tag{3.8}$$

As already discussed, the wave propagation depends on the dielectric and thermal properties that influence the energy distribution. As far as the real component of the electric permittivity decreases with the wave speed, its wavelength inside the medium is surely smaller than the vacuum one. This variation occurs at interface between materials with different ϵ' which is the cause of non-zero reflections. It is described by the wave impedance η in equation(3.9).

$$\eta = \frac{\eta_0}{\sqrt{\epsilon'}} \tag{3.9}$$

In the eq.(3.9), η_0 is the characteristic wave impedance in vacuum $\approx 377\Omega$.
It's important to consider the reflections on different materials interface because can lead to inaccurate or wrong system detections.

3.1.2 Dielectric polarization

Dielectric proprieties are defined by the polarization capability of material molecule. The polarization is the ability to store electromagnetic energy that is followed by a distortion of the charges distribution when under an electromagnetic field and it is different based on frequency and material.
There are mainly three mechanisms[4]:

- spatial or electronic charge polarization
- dipoles or oriental polarization
- ionic or molecular polarization

The dipoles polarization is relevant at lower frequencies with material with randomly oriented permanent dipole moments. When an electric field is applied, their orientation tends to align with it, polarizing the material. In this case an increase of the temperature can be seen.
Spatial polarization is characterized by materials where an applied electromagnetic field displaces the positive and negative charge clouds from the relative centers.
Ionic polarization instead is evident in materials that have positive and negative ions that are displaced by the applied field.

Dipole alignment

Generally dielectric molecule are neutral, but the asymmetry due to the non coincidence of negative and positive charge centers are the cause of the permanent dipole moments, explained by the equation(3.10).

$$\vec{p} = q\vec{l} \tag{3.10}$$

where $\vec{l}$ is the distance between two charges. Non polar molecules don't have a permanent moments, but it can be induced under a electromagnetic field. In order to calculate it, the polarization factor α', that is a measure of the inducted dipole moment by a unitary field, expressed as:

$$\vec{p} = \alpha' \vec{E_{loc}} \tag{3.11}$$

where $\vec{E_{loc}}$ it is used to describe the field around a particle. Anyway this alignment is opposed to the thermal agitation, so the equilibrium is reached when aligned molecules number N for volume unit is constant. So the total dipole moment can be characterized by the polarizability $\vec{P}$:

$$\vec{P} = N\alpha' \vec{E_{loc}} = \chi E \text{ where E is the applied field} \tag{3.12}$$

In vacuum, the electric field and the induction are linked by

$$\vec{D} = \epsilon_0 \vec{E} \tag{3.13}$$

In vacuum the equation (3.13) becomes

$$\vec{D} = \epsilon_0 \vec{E} + \vec{P} = (\epsilon_0 + \chi)\vec{E} = \epsilon \vec{E} \tag{3.14}$$

where χ is the absolute magnetic susceptibility reported in equation (3.15), while the relative one is in eq.(3.16).

$$\chi = \epsilon_r \epsilon_0 - \epsilon_0 = \epsilon_0(\epsilon_r - 1) \tag{3.15}$$

$$\chi_r = \frac{\chi}{\epsilon_0} = \epsilon_0(\epsilon_r - 1) \tag{3.16}$$

Using these equations a relation can be established between relative permittivity, propagation characteristic of the medium, polarizzation and the molecules properties:

$$\frac{N\alpha'}{\epsilon_0} = \epsilon_r - 1 \tag{3.17}$$

The equation for the local field is described by *Mossotti field equation* in eq.(3.18).

$$\vec{E_{loc}} = \vec{E} + \frac{\vec{P}}{3\epsilon_0} = \vec{E}\left(1 + \frac{\chi}{3\epsilon_0}\right) = \frac{\epsilon_r + 2}{3}\vec{E} \tag{3.18}$$

Rewriting the polarization(eq.(3.10)) as

$$\vec{P} = N\alpha' \frac{\epsilon_r + 2}{3}\vec{E} \tag{3.19}$$

it can be substituted in the local field equation(3.18), getting the *Clausius-Mossotti formula* (3.20).

$$\frac{N\alpha'}{3\epsilon_0} = \frac{(\epsilon_r - 1)}{(\epsilon_r + 2)} \text{ It connects the dielectric constant and polarizability} \tag{3.20}$$

A way to calculate dipole moment is based on the *Onsager* model, that represents a molecule as a center point of a cavity with comparable dimensions, volume $\frac{1}{N}$ and radius $(\frac{4}{3}\pi N)^{\frac{1}{3}}$. Then it is possible to calculate the dipole moment inside the cavity using:

$$\vec{p} = Volume \times P = \frac{4}{3}\pi\alpha^3\epsilon_0(\epsilon_r - 1)E \tag{3.21}$$

Followed by the electric field:

$$E = \frac{3\vec{p}}{4\pi\alpha^3\epsilon_0(\epsilon_r - 1)} \tag{3.22}$$

In case the applied field has smaller energy than the one dues to the thermal agitation, the medium polarization can be approximed by *Langevin* equation (3.23).

$$\vec{P} = \frac{N\vec{p}^2\vec{E_{loc}}}{3\kappa T} \tag{3.23}$$

where

κ is the Boltzmann constant

T applied field period

So the field inside an empty cavity is

$$\vec{E_{loc}} = \frac{3\epsilon_r}{2\epsilon_r + 1}\vec{E} \quad \textit{Onsager field} \tag{3.24}$$

The difference between the Mossotti field and the Onsager one is the field answer to the dipole moment, by a subtraction between eq.(3.24) and eq.(3.18):

$$\vec{E_R} = \frac{2(\epsilon_r - 1)^2}{3(2\epsilon_r + 1)}\vec{E} \tag{3.25}$$

Using the electric field expression(3.22) it is obtained:

$$\vec{E_R} = \frac{p}{4\pi\alpha^3\epsilon_0} 2\frac{\epsilon_r - 1}{2\epsilon_r + 1} = \frac{2pN}{3\epsilon_0}\frac{\epsilon_r - 1}{2\epsilon_r + 1} \tag{3.26}$$

The field in eq.(3.26) has no effect on dipole behavior since they are parallel, so that the only force on it is due by the Onsager field. Under these hypothesis the dipole moment in function of the Onsager field is obtained in equation(3.27).

$$p^2 = \frac{\kappa T\epsilon_0}{N}\frac{(\epsilon_r - 1)(2\epsilon_r + 1)}{\epsilon_r} \tag{3.27}$$

It's important underline that each presented field is static.

Considering now a non static field, the dipole moment orientation varies with the field orientation during its period T. A distinction based on the applied frequency must be done: at lower frequencies dipoles orientation is instantaneous with the applied field, while increasing the frequencies molecules bonds become dominant. So the polarization doesn't participate to the dielectric properties and the relative static permittivity tends to the otical one, ϵ_{rs}, depending on refraction index of the material(eq.(3.28)).

$$\epsilon_{r\infty} = n^2 \quad \text{with } n = \text{is the refraction index} \tag{3.28}$$

In this situation the equation (3.20) can be used to get the relative optic permittivity:

$$\frac{N\alpha'}{\epsilon_0} = \epsilon_{r\infty} - 1 \tag{3.29}$$

Then with same steps the following equations are obtained:

$$\epsilon_{rs} - 1 = \frac{N}{\epsilon_0}\left(\alpha' + \frac{p^2}{3\kappa T}\right) \rightarrow \text{ Relation between relative permittivity and polarizzability} \tag{3.30}$$

$$\epsilon_{rs} - \epsilon_{r\infty} = \frac{N}{\epsilon_0}\frac{p^2}{3\kappa T} \rightarrow \text{ Permanent dipole contribution to the static permittivity} \tag{3.31}$$

$$\frac{N}{3\epsilon_0\left(\alpha' + \frac{p^2}{3\kappa T}\right)} = \frac{\epsilon_{rs} - 1}{\epsilon_{rs} + 2} \rightarrow \text{Clausius-Mossotti formula} \tag{3.32}$$

In the end dipole moment is obtained as

$$p^2 = \frac{9\kappa T\epsilon_0}{N} \frac{(\epsilon_{rs} - \epsilon_{r\infty})(2\epsilon_{rs} + \epsilon_{r\infty})}{\epsilon_{rs}(\epsilon_{r\infty} + 2)^2} \tag{3.33}$$

Turning off the electric field, the material returns to its equilibrium after a time interval, called *relaxation time* τ. This constant, typical for each material, gives a measure of how much time the polarization uses, to decrease of e^{-1} factor.

Defining the polarization components as:

$P_f \rightarrow$ component due to dipoles formation

$P_a \rightarrow$ component due to dipoles alignment

and a $E = E_0 e^{j\omega t}$ is turned-on, P_a tends to its maximum value given by

$$P_a = (P - P_f)(1 - e^{-1/\tau}) \tag{3.34}$$

where P and P_f are

$$P = (\epsilon_{rs} - 1)E \tag{3.35}$$

$$P_f = (\epsilon_{r\infty} - 1)E \tag{3.36}$$

Using these equation in (3.34) it is obtained the following equation:

$$\frac{\partial P_a}{\partial t} = \frac{(\epsilon_{rs} - \epsilon_{r\infty})}{\tau} E_0 e^{j\omega t} - \frac{P_a}{\tau} \tag{3.37}$$

where its solution consists in

$$P_a = \frac{(\epsilon_{rs} - \epsilon_{r\infty})E}{1 + j\omega\tau} \tag{3.38}$$

The equation (3.38) shows the complex nature of polarization value, that influences phase difference between the applied field and dipoles polarization.
So this is why water content can influence a microwave imaging capability.

3.2 Dielectric properties in food

The dielectric properties of food material are complex value that change quite a lot with the frequency of the applied field. They are complex quantities because it takes into account the conduction current and displacement current, in quadrature with the other. So the relative complex permittivity is given by:

$$\epsilon_r = \epsilon_r' - j\epsilon_r'' \tag{3.39}$$

where, as already written parameters are

ϵ'_r is the real part, *dielctric constant*

ϵ''_r is the imaginary part, *dielectric losses*

Anyway the frequency of the field and the conductivity σ of the medium can have thermal generation inside it because the dissipation reported in eq.(3.40).

$$\sigma = \omega \epsilon_0 \epsilon''_r \tag{3.40}$$

As already done, the absorb coefficient α is reported

$$\alpha = \frac{\pi \epsilon''_r f}{c\sqrt{(\epsilon'^2_r)}} \tag{3.41}$$

Debye[11] gives a mathematical formulation of the polarization phenomena, written as

$$\epsilon_r = \epsilon_{r\infty} + \frac{\epsilon_{rs} - \epsilon_{r\infty}}{1 + j\omega\tau} \tag{3.42}$$

where the parameters are

ϵ_{rs} is the relative static permittivity at low frequency

$\epsilon_{r\infty}$ is the relative optic permittivity at higher frequencies

ω is the angular frequency

τ is the relaxation time

Separating the two components, it is obtained:

$$\epsilon'_r = \epsilon'_{r\infty} + \frac{\epsilon'_{rs} - \epsilon'_{r\infty}}{1 + (\omega\tau)^2} \leftarrow \text{Dielectric constant} \tag{3.43}$$

$$\epsilon''_r = \epsilon'_{r\infty} + \frac{(\epsilon'_{rs} - \epsilon'_{r\infty})\omega\tau}{1 + (\omega\tau)^2} \leftarrow \text{Dielectric loos} \tag{3.44}$$

So the polarization, that is defined by the water content of food material, conditions its dielectric properties, because its molecular symmetry leading to high polarization. Stronger are molecular water bonds, higher will be dipoles moments, then higher will be the losses inside the material.

3.2.1 Dielectric spectrum in food material

Water content influences electromagnetic wave interaction with the material structure. Higher is the water content, greater will be the dielectric constant and dielectric losses. Generally dielectric proprieties varies with the frequency and inside the dielectric spectrum(figure (3.1)) there are some interest regions:

- high relative permittivity values at frequencies under 100 Hz

a dispersion region at lower frequencies α, that is associated with ionic diffusion at molecular level

a dispersion region around10^2 KHz (β spectrum) dues to cellular membrane polarizations that are obstacles for their ions flux

a dispersion region called γ, on GHz frequencies caused by water content polarization

it is defined also the absolute value of the dispersion as $\Delta\epsilon = \epsilon'_{rs} - \epsilon'_{r\infty}$

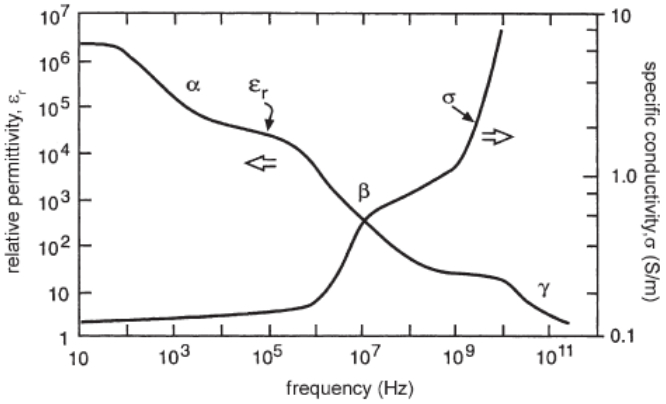

Figure 3.1: Frequency dependence of conductivity and relative permittivity

So it's always the water content that has great influence on dielectric proprieties around microwave frequencies.

3.3 Dielectric properties measure

Microwave technologies are based on the electromagnetic properties in high frequencies. The measurement of these properties is fundamental to create realistic model (called *phantom*) and to define the best coupled material to use. Generally at microwave frequencies used techniques are transmission lines, resonance cavity and free space measures. Each of these methods can be divided in many categories such as[11]:

- transmission and reflection measures
- resonant and non resonant methods
- closed or open structures to sense material under test characteristics

In closed structure methods are grouped waveguide and coaxial lines transmission measures and short-circuited reflection measures. While free space, coaxial lines and open circuit measurements are classified as open structure.

Measurement of dielectric properties of the orange marmalade and hazelnut cream was made by a coaxial probe inserted into the material itself.

An important role is played by the sample holder that is designed to avoid interference during measurements based on the sample's material. Simple examples of these are:

a small section of a coaxial line

a rectangular waveguide with a short circuit termination towards the sample

Holders are important because introduce the possibility to define the right position of the sample compared to the wave propagation axis. Dielectric properties (ϵ' and ϵ'') are then obtained using ad-hoc computer algorithms. With the technologies progression, controlling the instrumentations is simpler thanks to computer control that makes able to automate an high number of operations and the introduction of spectra analyzer and much other devices have made simpler to explore wider frequencies ranges.

3.3.1 Measurement systems

Impedance analyzer and LCR measure

An impedance analyzer aim is to measure the complex impedance between two ports at lower frequencies. It uses a sinusoidal wave generator, an amperemeter anda voltmeter and the simple equation to calculate the impedance[3]:

$$Z = \frac{V}{I} \tag{3.45}$$

Spectrum analyzer - Vector network analyzer (VNA)

From a simple point of view, the spectrum analyzer can be intended as an impedance analyzer, but with more functionalities. It is able to measure at radio-frequency and microwave range, using more complex methods. To make some measure of impedance or reflection factors, a sinusoidal generator stimulates the sample, while voltages and currents are acquired by the receivers. Using then ad-hoc hardware measures of incident and reflected phase and magnitude signal quantities are obtained, making possible the reconstruction of the dielectric properties of the sample. It's important underline the need of a calibration process to avoid error in scattering parameters collection.

S parameters basic principles

Finding scattering parameters is the main objective of the spectrum analyzer. These values describe the relation between magnitude and phase of incident and reflected waves.

The equations linking parameters to the waves are reported in eq((3.46) and (3.47)), depending on the considered port.

$$b_1 = S_{11}a_1 + S_{12}a_2 \tag{3.46}$$

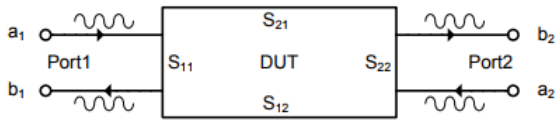

Figure 3.2: Example of a 2 ports devices and respective S parameters

$$b_2 = S_{21}a_1 + S_{22}a_2 \tag{3.47}$$

Considering a reflected wave from a device under test[1] as a linear combination of incident waves a_1 o a_2, the scattering parameters can be obtained imposing a termination, usually around 50Ω, that is the characteristic impedance Z_0, first on one port and then on the other one, writing the following:

$$S_{11} = \left.\frac{b_1}{a_1}\right|_{a_2=0} \tag{3.48}$$

$$S_{12} = \left.\frac{b_1}{a_2}\right|_{a_1=0} \tag{3.49}$$

$$S_{21} = \left.\frac{b_2}{a_1}\right|_{a_2=0} \tag{3.50}$$

$$S_{22} = \left.\frac{b_2}{a_2}\right|_{a_1=0} \tag{3.51}$$

The parameters subscript S_{mn} indicate m, the receiver port number and n that in transmission. So it is possible write all S parameters inside a matrix, colled *S matrix*, where each subscripts are used as matrix address.

3.3.2 Measurement methods

Resonant cavity

Resonant cavities are structures with high quality factor Q, that have determined resonant frequencies. As in figure(3.3), the cavity must have an interface with the network analyzer and a computer desktop in order to acquire data. This methods is based on create a perturbation inside the cavity. This structure is excited just belove cut-off frequency for TM_{01} mode, while TEM propagates along the central conductor, which length can be varied based on the desired resonant frequency. Sample influences the main resonant frequency and the quality factor of the cavity. From these quantities, complex permittivity or permeability can be calculated for a singular frequency. In case the sample holder is in a fixed position the sample must be at the coordinate where there is the maximum electric field, or in case of magnetic measurement at maximum magnetic field. The insertion

[1] DUT

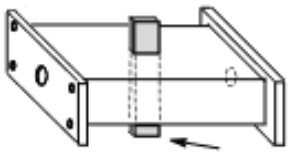

Figure 3.3: Example of resonant cavity

of sample in the middle of the guide provokes a shift in the position of the maximum electric field toward its position because the insertion adds an odd number of wavelength ($n = 2\kappa+1$). In case of magnetic measure the maximum field will shift for even wavelength ($n = 2\kappa$) towards sample position. This shift can be measured to find the dielectric properties. Anyway the sample dimensions must be small, with a volume V_s, in order to be inserted in the cavity, with volume V_c, which change the resonance frequency and quality factor. If the holder is not fixed, the measurement starts obtaining the TEM components from propagated and reflected wave, deriving the following equations:

$$E^0_{\rho s} = \frac{A}{\rho} e^{j\beta z} + \frac{B}{\rho} e^{-j\beta z} \tag{3.52}$$

$$H^0_{\phi s} = \frac{-A}{\eta\rho} e^{j\beta z} + \frac{B}{\eta\rho} e^{-j\beta z} \tag{3.53}$$

where η is the impedance calculated in free space, A and B are two constants. Boundary conditions are applied to the field along central conductor coordinates $z = 0$ and $z = L$ So from the solution of equations (3.52) and (3.53) in $z = 0$, $A = -B$ is obtained, while solving for the second condition it gives the resonance. Using these in equations (3.52) and (3.53), they became:

$$E^0_{\rho s} = \frac{A}{\rho} \sin(\beta z) = E_{0,max} \sin(\beta z) \tag{3.54}$$

$$H^0_{\phi s} = \frac{A}{\eta\rho} \cos(\beta z) = H_{0,max} \cos(\beta z) \tag{3.55}$$

If the cavity is rectangular, the electric energy is calculated from:

$$w_e = \frac{\epsilon_0}{2} \int_{V_c} {E^0_{\rho s}}^2 dv \tag{3.56}$$

and using eq.(3.54):

$$w_e = \frac{\epsilon_0}{2} \int_0^{2\pi} \int_a^b \int_0^L {E_{0,max}}^2 \sin^2 \beta z \rho d\rho d\phi dz \tag{3.57}$$

where b is the external radius and a the internal one of coaxial resonator. The answer of the cavity to the perturbation is a frequency shift calculated as:

$$-\frac{d\Omega}{\Omega} \approx \frac{(\epsilon_r - 1)\epsilon_0 \int_{V_s} E.E_0^* dV + (\mu_r - 1)\mu_0 \int_{V_s} H.H^* dV}{\int_{V_c} (D_0 E_0^* + B_0 H_0^*) dV} \tag{3.58}$$

In eq.(3.58), the numerator represents the sample stored energy, while the denominator the total energy of the cavity.
So under the hypothesis that sample position is at the maximum electric field and only the first term of the numerator is significant since exist only a small variation in ϵ or μ in respective fields that doesn't change the resonant frequency, the frequency shift due to the sample can be obtained with

$$-\frac{d\Omega}{\Omega} \approx \frac{(\epsilon_r - 1)\int_{V_s} E E^*_{0,max} dV}{2\int_{V_c} |E_0|^2 dV} \tag{3.59}$$

and considering quality factor too, the equation (3.60) is obtained.

$$-\frac{d\Omega}{\Omega} \approx \frac{d\omega}{\omega} + \frac{j}{2}\left[\frac{1}{Q_s} - \frac{1}{Q_c}\right] \tag{3.60}$$

Knowing that $\epsilon_r = \epsilon'_r - j\epsilon''_r$ and equalizing the equations (3.59) and (3.60), the dielectric constant is obtained as eq.(3.61) and the losses as eq.(3.62).

$$\epsilon'_r = \frac{V_c}{2V_s}\frac{(f_c - f_s)}{f_s} + 1 \tag{3.61}$$

$$\epsilon''_r = \frac{V_c}{2V_s}\frac{1}{2}\left[\frac{1}{Q_s} - \frac{1}{Q_c}\right] \tag{3.62}$$

Regardless of this method has great accuracy, it presents some errors due to the fact that the cross-section dimension of the sample must be exactly known and the numerical approximation made by algorithms can introduce some errors too, decreasing the quality of results.

Parallel planes

This technique is based on a parallel plane capacitor used as sample holder. It uses an impedance analyzer or LCR measurer. Generally measure are made at low frequencies, inside $20Hz$ to $1GHz$ range. Sample is stimulated by an AC signal and the voltage dropped on it is measured. In case of direct electrodes contact with the sample, permittivity is calculated from their capacity. Since electrodes are not ideal there is a air gap between contacts and sample leading to a parassitic series capacitance that will influences the results. The used equations are:

$$C_0 = \epsilon_0 \frac{A}{t_a} \rightarrow \text{Air gap capacitance} \tag{3.63}$$

$$C_x = \epsilon_x \epsilon_0 \frac{A}{t_m} \rightarrow \text{Dielectric capacitance} \tag{3.64}$$

$$C_{err} = \frac{1}{\frac{1}{C_0} + \frac{1}{C_x}} = \epsilon_{err}\epsilon_0 \frac{A}{t_m + t_0} \rightarrow \text{Measured capacitance} \tag{3.65}$$

$$1 - \frac{\epsilon_{err}}{\epsilon_x} = \frac{\epsilon_x - 1}{\epsilon_x + \frac{t_m}{t_a}} \rightarrow \text{Measured error} \tag{3.66}$$

Free space measurement

Free space measurement uses microwave antenna to enlighten the sample, assuming only a TEM mode propagation.

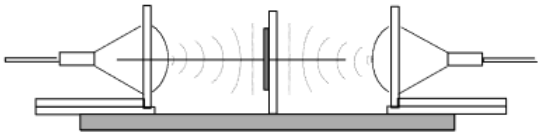

Figure 3.4: Example of free space measure

The measurement doesn't need any contact, it isn't destructive and can be used at high frequencies, but at lower frequencies it can't be used cause the wavelength constrains due to the sample dimensions. The systems is generally composed by a network analyzer, a transmitter and receiver, software and hardware elements. The antennae are connected to the spectrum analyzer. VNA also is useful to reduce error caused by the holder.
This method need a careful calibration of the VNA in order to reduce errors due to diffraction and reflections effects between antennae and the sample dimensions can't be too much smaller.

Coaxial probe

Coaxial probe method consists of putting the terminal probe region in contact with sample. Then through the probe an electromagnetic field whose scattering parameter S_{11} is acquired to get the dielectric constant. System is composed by spectrum analyzer, coaxial probe and ad-hoc software to calculate the dielectric parameters. The probe should be calibrated to avoid errors due to the different impedances. In addition the air gap inside the contact region must be considered, that can slow down the entire measurement process because the time interval to stabilize the signal. By the way measures haven't enough accuracy and only reflection measure can be performed.

Transmission line

In this method sample is inserted inside the transmission line, generally with rectangular section, where only TEM mode is propagating. S_{11} and S_{21} are then measured and used to get dielectric constant and losses. This system type is characterized by a spectrum analyzer, coaxial lines or waveguide section (usually 50ω adapted), a computer and software.
Main disadvantage is the frequency constrains that fix the upper frequency around $10GHz$ in order to consider the parassitic elements of the guide negligible.

Chapter 4

Three-dimensional model design

In food monitoring, microwave imaging technology is a valid alternative to the methodologies already in use. It has main advantages that make it preferable to manufactures point of view such as:

- absence of ionizing radiation, that ensures health food, unlike X-rays
- low cost, making the production line integration of the system simpler

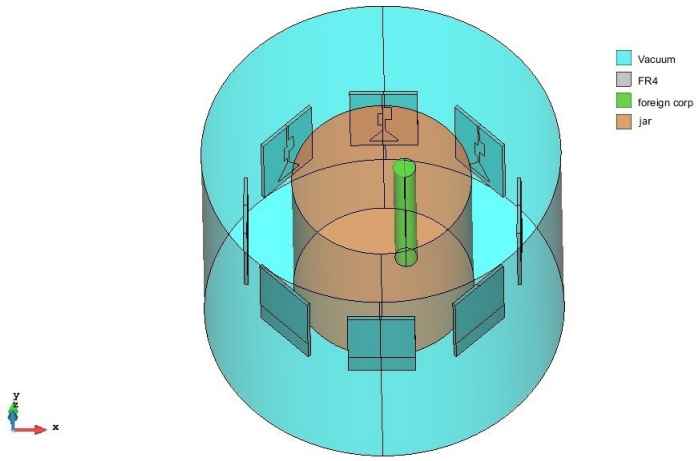

Figure 4.1: Starting model

Microwave imaging (MWI) is a tomographic method[42] whose aim consists to map the dielectric properties of inspected domain without any invasive procedure, only acquiring domain field and scattering parameters. The detection is made possible because material and foreign object have different electrical properties. Aim of this system is to obtain a correct detection of the intruder, its position is a less important point.

As starting point, an already available narrow band monopole, showed in figure (4.2), was used to work in air space and tests the correct functionalities. Then a new ultra wide band monopole is proposed, reported in figure (4.3), in order to have the possibility of explore a wide frequency range, that has a great influence on the detection capability of the system, in terms of field penetration capability and minimal resolution.

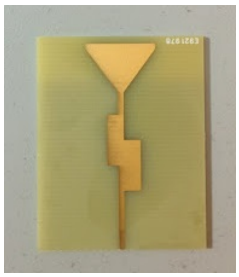

Figure 4.2: Narrow band monopole model

Figure 4.3: Ultra wide band monopole model

Each3D models was created using GID[8]. The MWI model (fig.(4.1)) represents the entire antennae and jar system where the components are:

- cylindrical jar, initially completely made of marmalade or hazelnut cream
- a cylindrical foreign object made of air, to verify the correct functionality of the system
- n antennae equally spaced around the jar

Foreign object is made of air, to ensure high difference in term of dielectric constants that leads to an high contrast with the investigated domain. Next steps consist in complicating the model with material jar addition, change the intrusion type, material and dimensions to get closer to a real situation.

4.1 3D model creation

Model creation is made with GiD version 13. GiD is a pre and post processor useful to create three-dimensional models and mesh to use in finite element methods of more in general in numeric analysis.

Simplified jar model

Inside the firsts simulations the aim is to obtain a correct detection of the intruder at different frequencies and with different object materials. So jar, as reported in figure (4.4) is made completely of its content, orange marmalade or cream hazelnut with a cylindrical geometry to study the detection capability in ideal conditions. The chosen dimensions are the same of a real jar (fig.(4.5)) and are:

- radius $= 4cm$

- height $= 8cm$
- inferior base center corresponds to the *system center*

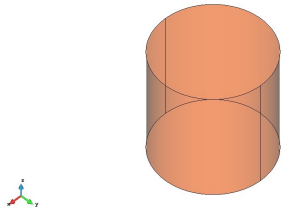

Figure 4.4: 3D jar model

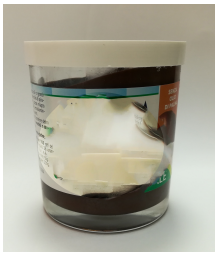

Figure 4.5: Jar example

The dielectric properties, in terms of electric conductibility and permittivity of jar contents are showed for orange marmalade and hazelnut cream respectively, in figure (4.6) - (4.7) and (4.8) - (4.9), where the frequency variation can be appreciated. Those behaviors have an important role on detection capability of the system because have a severe impact on field penetration depth and resolution at every frequency.
These quantities have been measured using the dielectric probe method at earlier project steps.

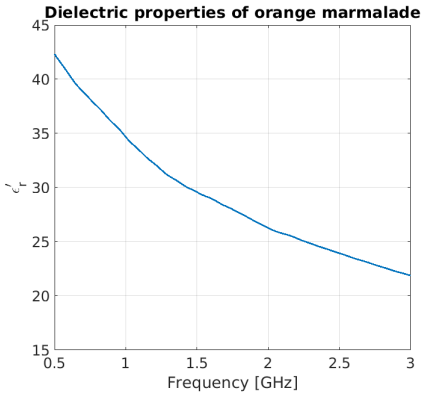

Figure 4.6: Real part of the electric permittivity of orange marmalade

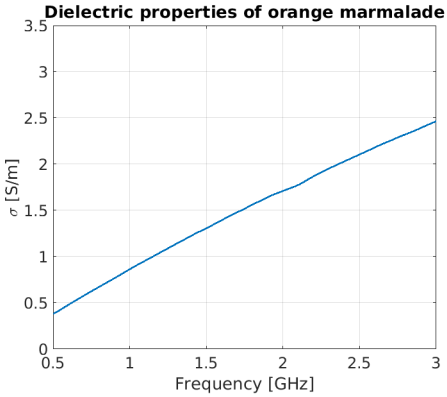

Figure 4.7: Dielectric conductivity of orange marmalade

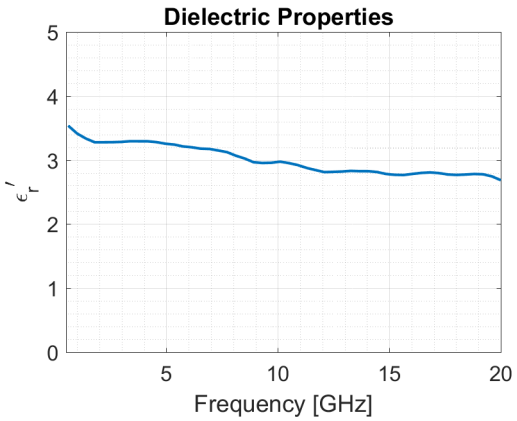

Figure 4.8: Real part of the electric permittivity of hazelnut cream

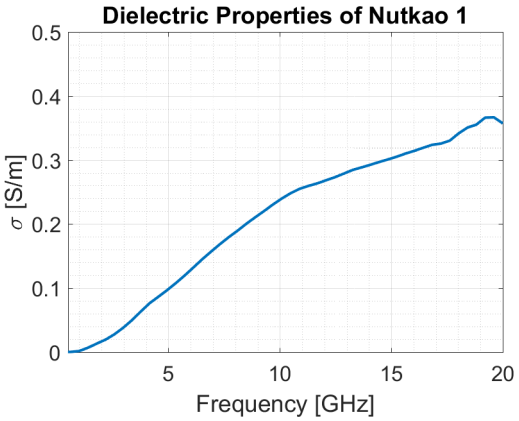

Figure 4.9: Dielectric conductivity of hazelnut cream

Jar introduction and 3D model

Next step is the introduction of jar around the marmalade/hazelnut cream volume as shown in figure (4.10). Total volume of food and jar is the same of the previous case, but now material and thickness of jar are considered:

- thickness $= 3mm$
- glass
  $\sigma = 0$
  $\epsilon_r = 4.7$
- *glassPET* plastic
  $\sigma = 0$
  $\epsilon_r = 3.4$

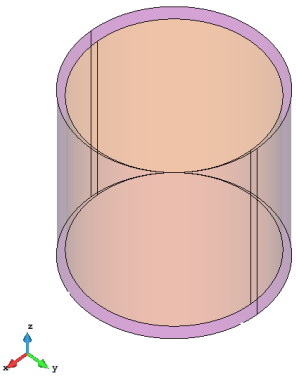

Figure 4.10: 3D model where jar volume is specified

Ideal intrusion modeling

After jar definition, the foreign object must be introduced inside the food volume. As first attempt it is created as a cylindrical object (see figure (4.11a)) because it is used to verify the correct functionality of MWI system. Defined through GiD, the external volume is holed inserting the intruder. This operation is necessary because the program can't handle volume that are simply overlapped, it doesn't manage mesh because can't correctly define

the material to be assigned. This steps are valid every time volume are defined inside another one.

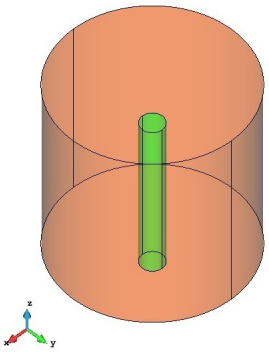

(a) Intrusion inside the jar

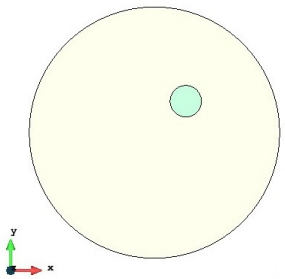

(b) Top view

Inside initial steps the intrusion dimensions are:

- radius = $0.5cm$
- height = $7cm$, in order to be completely immersed into the volume letting $0.5cm$ from each of the two basis
- lower center coordinates are 1.5,1 cm

Studying for now the ideal case the intrusion is defined with the vacuum dielectric properties considered constant with the frequencies, in order to get a strong contrast with the around material. Vacuum dielectric values are

$\sigma = 0.0$

$\epsilon_r = 1.0$

Step by step the intrusion will be replaced by a sphere made of air, then glass or plastic to move towards a real situation.

Antenna model integration

Inside the simulation model there are 8 antennae too, whose position is around the jar along a circle with different radius based on used antennae:

$6cm$ in case of narrow band monopole (fig.(4.2))

$8cm$ in case of ultra wide band monopole (fig.(4.3))

Antennas are used one at time as transmitter while the others as receiver to get a 3D scan of the dielectric properties of the sample. Model with positioned antennae are in figure (4.12a) and (4.12b).

The two antenna proposed are described in section 4.2 and 4.3.

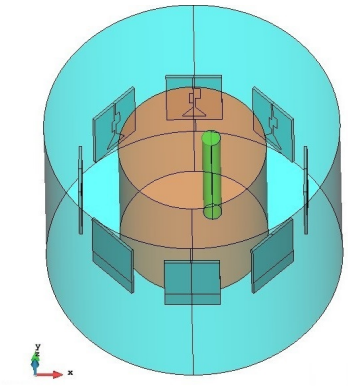

(a) Narrow band antennae inside the model

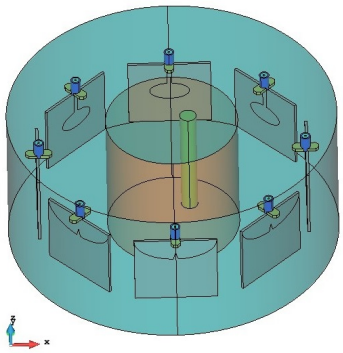

(b) Ultra wide band antennae inside the model

Figure 4.12: Model examples

Background volume definition

The background volume, showed in figure (4.13)), represents the space region where the system is placed. It is modeled as an air cylinder containing all of its components.

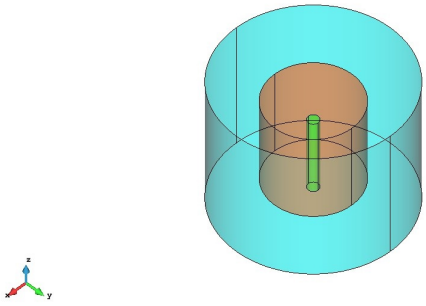

Figure 4.13: Background volume addition

It must be present into the model because the used finite element method requires it to obtain a correct simulation of the propagation problem.
This cylindrical container must include the entire system, so its dimensions are:

- narrow band monopole situation:
  radius = $8cm$ and height = $12cm$
- ultra wide band monopole situation:
  radius = $10cm$ and height = $9cm$

It's important underline that its dimensions can have a great impact on the simulation time, so should be minimized.

4.2 Narrow band monopole definition

First used antenna is a narrow band monopole, which substrate is made of FR4. The model utilized in GiD is reported in figures ((4.14a) and (4.14b)), already available at laboratory.

(a) Front face of narrow band monopole **(b)** Back face of narrow band monopole

Figure 4.14: Narrow band antenna model

The behavior of this antenna, in a frequency range between 0.5 GHz and 8 GHz, is been measured in laboratory using a VNA. The resulted S_{11}, figure (4.15), shows some resonance peaks at:

- f=2.75 GHz with S_{11} = -6.862 dB
- f=6.25 GHz with S_{11} = -22 dB
- f=6.75 GHz with S_{11} = -40.1 dB
- f=8.00 GHz with S_{11} = -9.7 dB

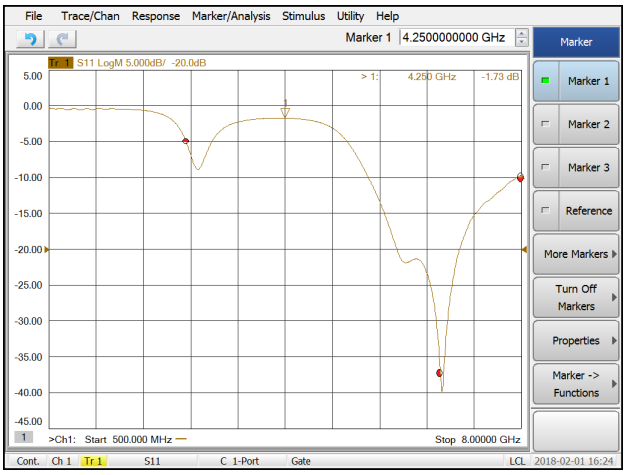

Figure 4.15: Narrow band monopole measured S_{11}

In the following figure are showed the max currents at various frequencies along the antenna structure.

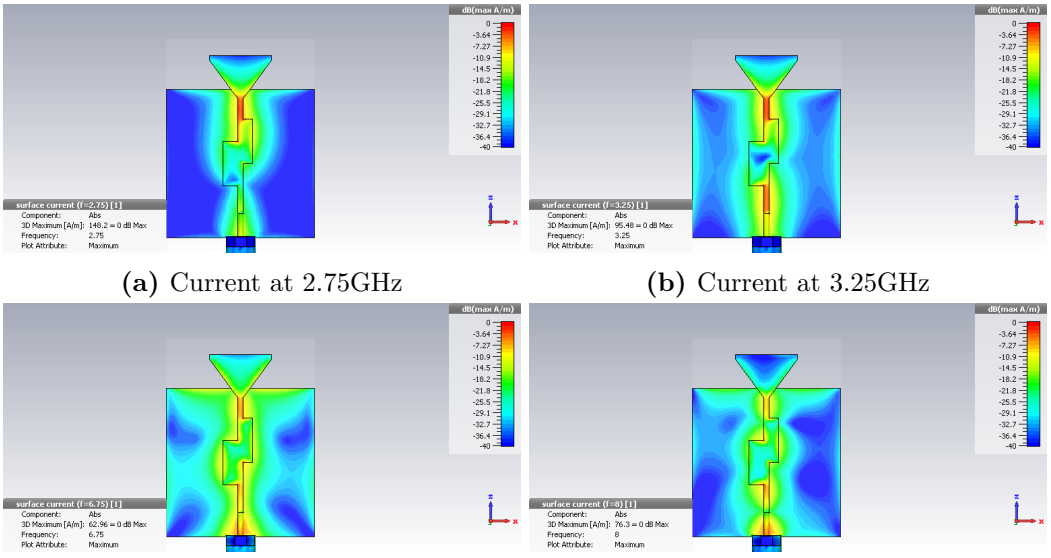

(a) Current at 2.75GHz

(b) Current at 3.25GHz

(c) Current at 6.75GHz

(d) Current at 8GHz

Figure 4.16: Flowing current on the monopole antenna

The model used into the simulation is been created on GiD. The materials composing the antenna are

- substrate dielectric → FR4;
- surface geometries → PEC (underlined in figures (4.17a) and (4.17b));

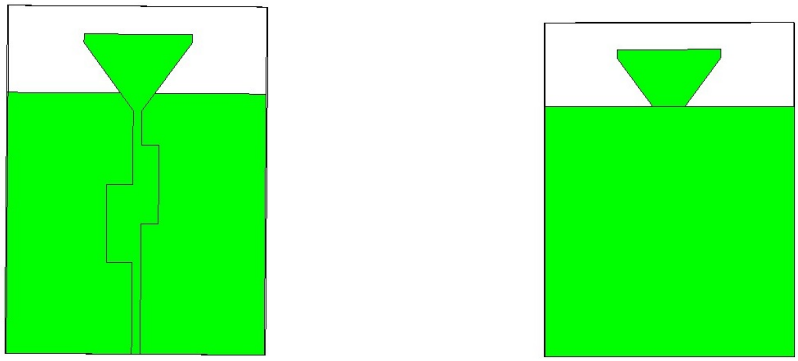

(a) Front surface PEC **(b)** Back surface PEC

Figure 4.17: PEC surface definitions

PEC condition is a boundary condition that defines an ideal material whose electric conductivity is infinite. It is defined on surfaces where should not be any electromagnetic field reflection, as metallic surfaces.
The source of this monopole is define as a line probe, called *current probe*, between the two midpoint of antenna bases as reported in figure (4.18).

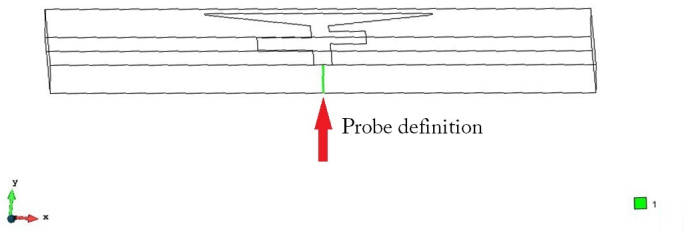

Figure 4.18: Input/output port position

Defined the model, the monopoles are added to the MWI system model, as shown in figure (4.19).

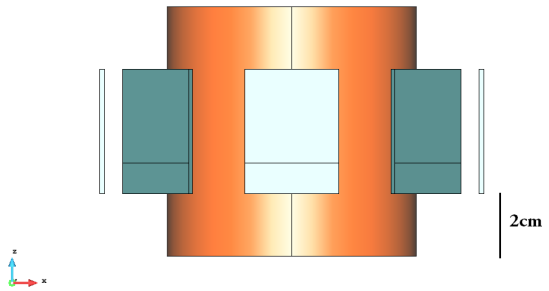

Figure 4.19: Antennas position

4.3 Ultra waveband monopole model and definition

In this section the proposed antenna is presented. A new monopole with larger bandwidth is needed in order to have the possibility to explore a wider range of frequencies in order to increase the detection ability and resolution of the system.

(a) Front face of the UWB monopole **(b)** Ground plane of the UWB monopole

The proposed antenna, which geometries are shown in figures (4.20a) and (4.20b)) is a ultra wideband monopole[28] that is characterized by S_{11} parameter under $-10dB$ in a frequency range between 1.9 GHz and 30 GHz. Presented simulation are stopped around 20 GHz because the MWI system must preserve a low cost equipment, which optimal behavior is ensured below that frequency. Antenna dimensions are:

substrate:

- L= $45mm$ x W= $50mm$ x Z= $1.6mm$

feed line:

- $L_1 = 15mm$ x $W_1 = 3mm$

main ellipse:

- semi major axes= $12mm$
- semi minor axes= $6mm$

ground plate:

- semi major axes= $25mm$
- semi minor axes= $14.5mm$

and the "V" cut:

- base= $3mm$ and edge= $5.2mm$

3D model is been created using CST STUDIO SUITE[1][37], a commercial software for electromagnetic simulation.

Specified material inside the model are:

- substrate dielectric → FR4;
- surface geometries → PEC (underlined in figures (4.26) and (4.27));

The first simulation sees the antenna without the SMA[2] connector. As reported in figure (4.21), the results are not acceptable.

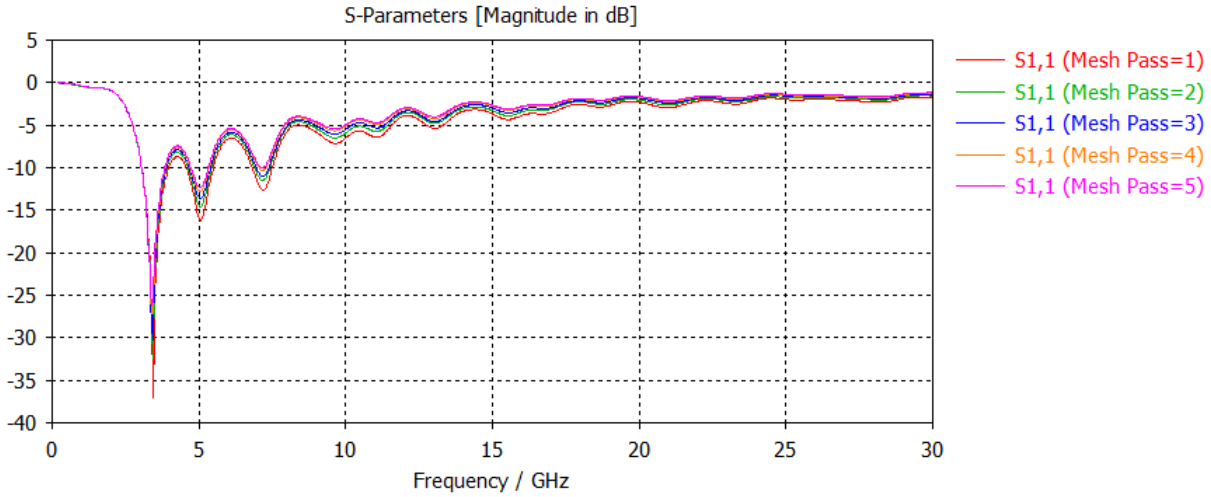

Figure 4.21: S_{11} result without SMA connector

So connector SMA, which model is shown in figure (4.22), is added to the model.
The connector specification follows the standards. The blue volume is defined as *Teflon PTFE*, while the others are PEC. To make the contact between the two structures:

in CST is enough overlap them (figure (4.23))

in GiD is necessary to define the intersection manually (figure (4.24))

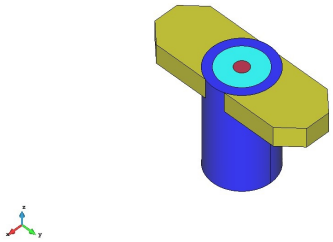

Figure 4.22: SMA connector model

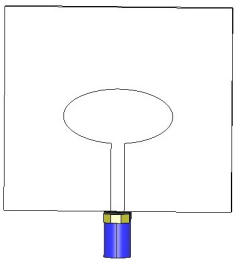

Figure 4.23: GiD model

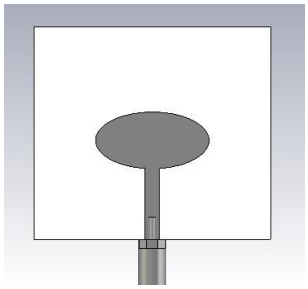

Figure 4.24: CST model

This time the source must be assigned at the input port of the coaxial line as indicated in figure (4.25), that corresponds to the Teflon section. This condition is assigned in GiD using the *Coaxial TEM conditions* → *CoaxialPort In* conditions, while in CST creating a waveguide port on the correspondent surface. It is also necessary to define the section center, external and internal radius of the coaxial line.

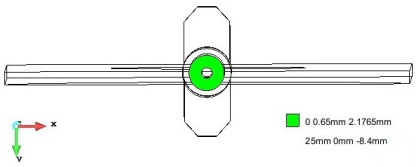

Figure 4.25: Coaxial line source definition

In the end the PEC condition are assigned at the metallic surface, showed in figures (4.26) and (4.27).

GiD discretization and FEM results

First of all the model is discretized with a tetrahedral mesh, which minimal dimension is based on working frequency and dielectric properties of the materials using the following

[1]Research purpose license

[2]Sub miniature type A

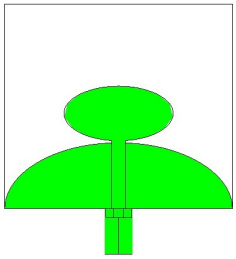

Figure 4.26: Front side PEC

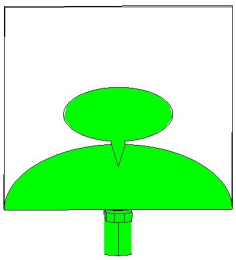

Figure 4.27: Back side PEC

equations:

$$mesh\_dimension = \frac{\lambda_{media}}{k} \tag{4.1}$$

where λ_{media} is the wavelength inside the propagation medium, expressed in eq.(4.2).

$$\lambda_{media} = \frac{\lambda_0}{\sqrt{\epsilon_r'}} \tag{4.2}$$

λ_0 is the light wavelength in vacuum space at working frequency, while ϵ_r' is the real part of the medium electric permittivity. Factor k is used to define the mesh density, which has a big impact on time simulation. So a good compromise is keep it around 10 or 15.

One of the output of the FEM is the field distribution inside space, where the correct irradiation can be observed (figures (4.28) and (4.29)).

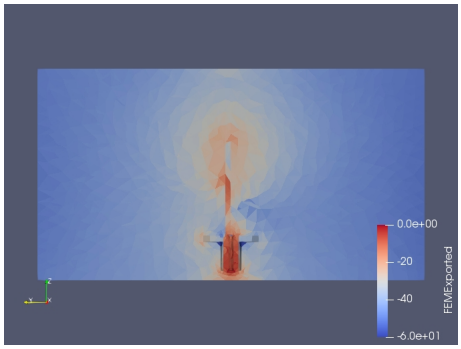

Figure 4.28: Antenna irradiation - Y cut

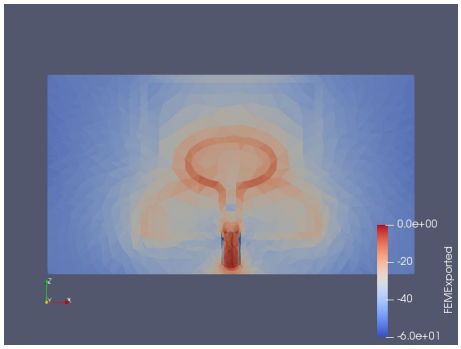

Figure 4.29: Antenna irradiation - X cut

Simulation results with CST STUDIO SUITE

CST simulation was made on a frequency range between $0.5GHz$ and $20GHz$ with the model in fig.(4.30) and (4.31), using a tetrahedral mesh too.

The obtained simulated S_{11}, showed in figure (4.32), extends from $3.26GHz$ to $20GHz$ as expected, with high peaks around 11 GHz and 16 GHz, while the measured one is a

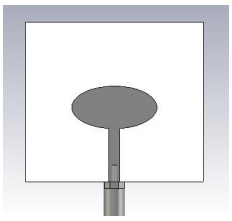

Figure 4.30: CST model: frontal plate

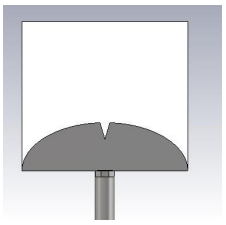

Figure 4.31: CST model: back plate

bit different because the presence of some non ideal elements such as the solder of the connector or the wires length. The measured results are in figure (4.33).

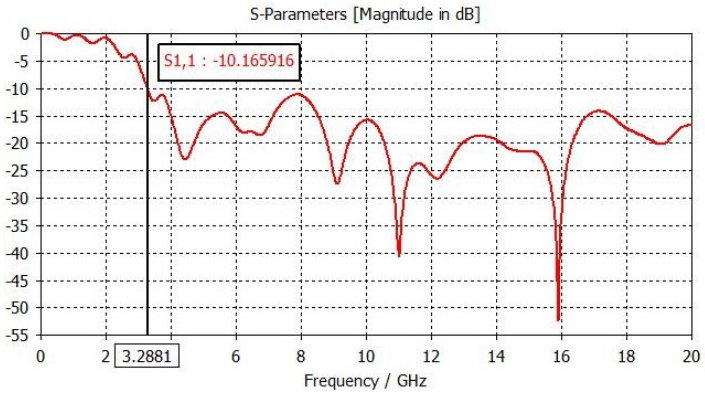

Figure 4.32: Simulated return loss of the UWB antenna

To complete the informations about this monopole the current flows on it are reported for various frequency in figures (4.34).

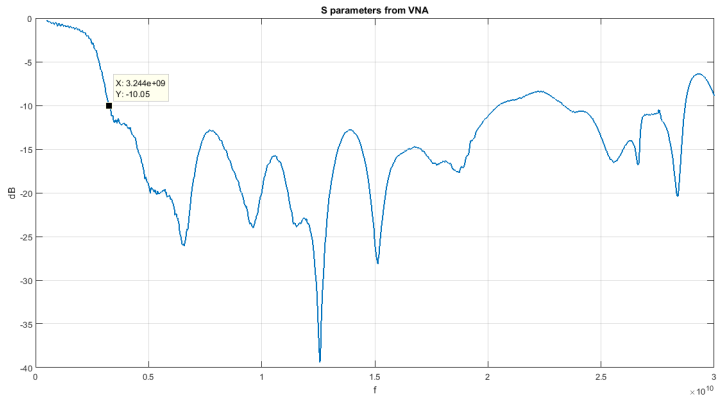

Figure 4.33: Measured return loss of the UWB antenna

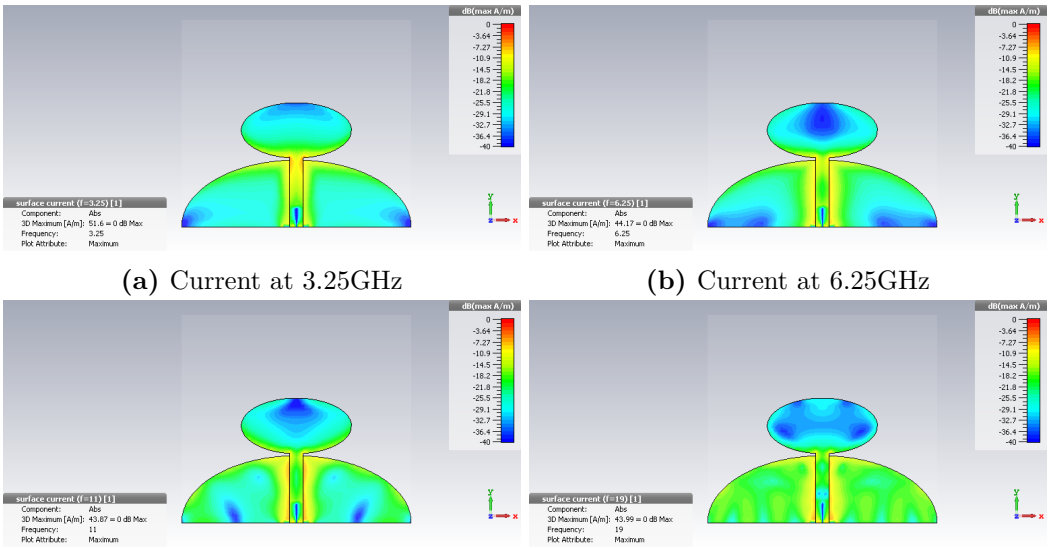

(a) Current at 3.25GHz

(b) Current at 6.25GHz

(c) Current at 11.00GHz

(d) Current at 19.00GHz

Figure 4.34: Flowing current on the monopole antenna

Then to understand the irradiation of the antenna is necessary to show the radiation pattern cut at different frequencies. The two dimensional figures are generated cutting across the x-y plane, showing that the main lobe radiates inside the front plane.

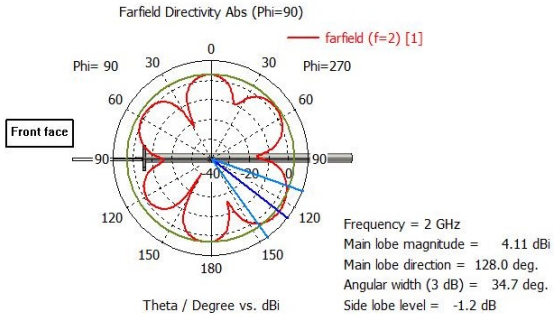

Figure 4.35: Radiation pattern cut at $2GHz$

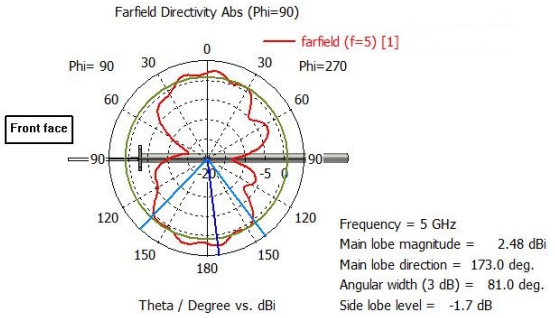

Figure 4.36: Radiation pattern cut at $5GHz$

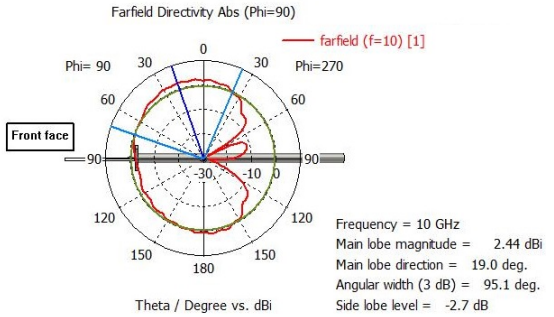

Figure 4.37: Radiation pattern cut at $10GHz$

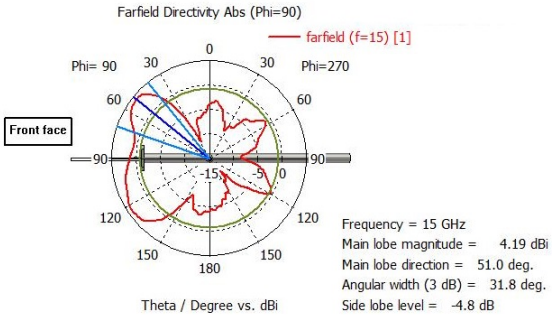

Figure 4.38: Radiation pattern cut at $15GHz$

4.3.1 UWB antenna integration inside MWI model

As already made with the narrow band monopole, the antenna model is inserted inside the system with distance 1cm from the jar base. Since the dimensions are larger than the previous antenna and their number must be kept constant, equal to 8, their distance from the center is increased to 8cm, as shown in figure (4.39) and (4.40).

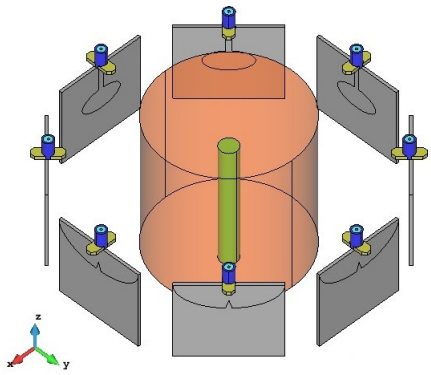

Figure 4.39: Starting model with UWB antennae

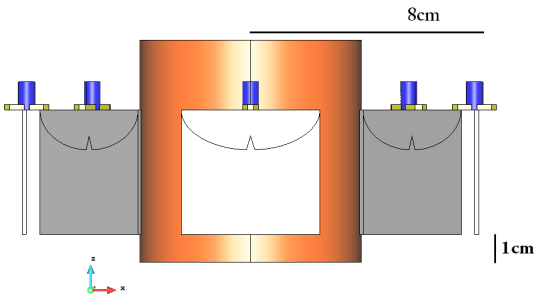

Figure 4.40: Lateral view of the model with UWB antennae

4.4 General conditions and material properties definition in GiD

Inside the model must be assigned various conditions in order to be simulated: boundary conditions, material dielectric properties.

Starting from the antenna , it is composed by:

- substrate of FR4:
  $\sigma = 0$ and $\epsilon'_r = 4.1$
- PEC conditions on the metallic surfaces, that are the geometrical pattern of front and back plates

Jar characteristics are

initially is completely made of

- orange marmalade
- hazelnut cream

in the more realistic models, thickness and material of the jar are considered

- glass:
  $\sigma = 0$ and $\epsilon'_r = 4.7$
- *GlassPET* plastic:
  $\sigma = 0$ and $\epsilon'_r = 3.4$

Dielectric quantities of the investigation domains vary with the frequency and are defined in function of the working frequency.

For example some used valued inside the simulations are listed in table (4.1).

Background volume si defined as air, which $\sigma = 0$ and $\epsilon'_r = 1$.

In addition a condition on its surfaces must be defined in order to be seen as an infinite space, where no field reflection comes back. This property can be found under *Coaxial TEM conditions*, which in finite element method corresponds to the *Absorbing boundary consitions (ABC)*.

Table 4.1: Some values of conductibility and electric permittivity

Frequency	$1GHz$	$2GHz$
Orange marmalade	$\sigma = 0.7$ $\epsilon'_r = 35$	$\sigma = 1.7$ $\epsilon'_r = 26.5$
Hazelnut cream	$\sigma = 0.00065$ $\epsilon'_r = 3.6$	$\sigma = 0.01$ $\epsilon'_r = 3.275$
Frequency	$2.25GHz$	$2.75GHz$
Orange marmalade	$\sigma = 1.9$ $\epsilon'_r = 25.05$	$\sigma = 2.29$ $\epsilon'_r = 22.8$
Crema di nocciole	$\sigma = 0.015$ $\epsilon'_r = 3.28$	$\sigma = 0.027$ $\epsilon'_r = 3.285$
Frequency	$3.25GHz$	
Crema di nocciole	$\sigma = 0.027$ $\epsilon'_r = 3.285$	

4.5 Mesh and GiD output file

Now that each conditions and materials, useful for the correct numerical simulation, have been assigned, the discretization of the model can be made. This step consists in the subdivision of the model in many tetrahedron with same dimensions, where the simulator will solve the inversion problem, using them to approximate the electromagnetic propagation equations for the detection.

Moreover, if needed, on the boundaries of each regions can be applied conditions that should make computationally simpler crossing different regions. Mesh quality can be observed from:

Convergence rate

Higher is this value, faster will be the convergence of the problem towards a solution. In case the mesh isn't sufficiently accurate it is probable that some elements of the model might be ignored cause too much smaller compared to the mesh cell dimension.

Precision of the solution

Generally using mesh element smaller, a more precise solution is got, because also the smaller variation on the model are taken in consideration, increasing its reliability.

Elaboration time

It's obvious that higher is the elements of the mesh, more time and more resource the simulator will need to solve the problem

4.5.1 Three dimensional mesh generation

Tetrahedral mesh is used because it discretizes a 3D model. The created mesh type is *unstructured* meaning that the cells connections aren't equal, differently for a *structured* one, where the connections are regular.

Minimal dimension of tetrahedrons is calculated using (4.1), where λ_{mezzo} is obtained considering the higher values among the real component of the electric permittivities of

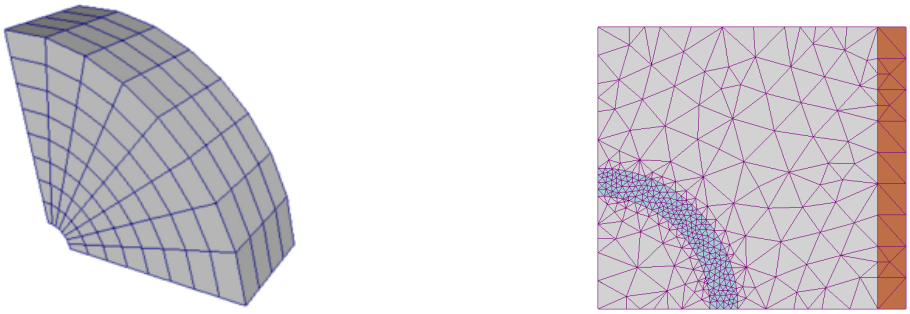

(a) Structured mesh example **(b)** Unstructured mesh example

Figure 4.41: Mesh examples

the investigated material. In this way mesh size calculated for high frequency values can be used too for lower frequencies, because it has already enough precision. It is already written that their number can have high impact on time requirement to solve the problem, so few precautions to limit it are considered:

- thinner mesh size on the investigated volume, considering the factor k = 15 → jar and its content
- bigger mesh size elsewhere, using a k = 10

In this manner model has enough reliability and elaboration time isn't too much expensive. Considering as example the starting model with narrow band monopole (fig.(4.12a))and the model of figure (4.12b) , the generate meshes are reported in fig.(4.42).

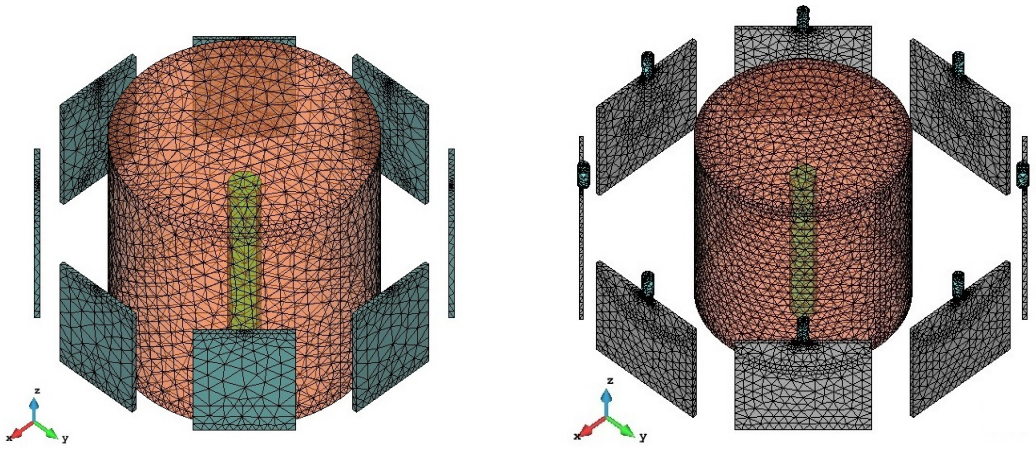

Figure 4.42: Model mesh examples

In analyzed cases number of tetrahedrons involved in the investigated volume is around 2.5×10^6, that depends on material and frequency considered. If variations in position, number or dimensions of the elements in the model must be applied, the entire mesh must be redone to have the expected accuracy.

4.6 FEM input file generation

Ended the discretization step, it is possible generate the file to give as input to the FEM simulator. It is generated by the command *file→export→calculation file*, getting a *.dat* file. This file is essentially a text file containing the information about mesh dimensions, material parameters, output and input ports, eventual conditions. It is composed by several parts:

- *Coordinates* section. It includes points in Cartesian coordinates and their total number
- *Elements* section, that includes information about tetrahedrons such as vertexes coordinates, assigned material and total number
- The PEC section, PEC faces, input/output ports and conditions sections are the following
- a table summarizing the dielectric properties of each material included in the model, in terms of conductivity and permittivity

Thanks to this file, FEM simulator is able to assign materials and conditions at each element of the mesh.

Chapter 5

The Finite Element Method FEM

Finite element method is a numerical algorithm which aim is to convert partial differential equations into a set of linear algebraic equations, used to obtain approximate solutions to mathematical problems, that in this project corresponds to the wave propagation problem[21]. FEM is based on the approximation of partial differential equation solutions. The main characteristic of this method is the fact that can be used with arbitrary shape and inhomogeneous materials, required in presented system. Our starting point is the previous generated mesh, whose example is reported in figure (5.1). It's important note that where higher precision is required it is denser.

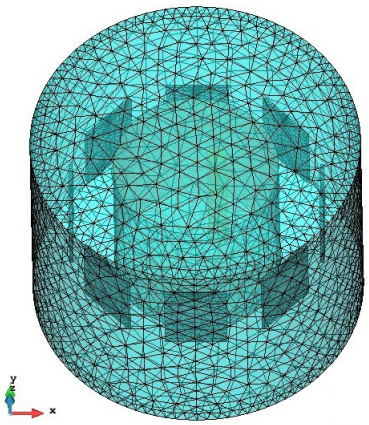

Figure 5.1: Tetrahedral mesh example

Each tetrahedron is a sub-domain, that composes the model, and represents a *finite element*, where the method finds the approximated solution. These geometrical forms are chosen because the aim is a 3D reconstruction and are quite flexible to model various shapes. The solutions is obtained from linear combination of *basis functions* or called *norm functions*, that are the approximated partial differential equations for the problem. Anyway being an approximated solution, there will always be non null error because the modeling

step and the mesh, which decrease the *degrees of freedom* of every point of the model. To these mesh elements will be associated some points, called *nodes*, that individuate its geometry, where a field value is linked. A degree of freedom is a measure of how many values the field can acquired in that point.

5.1 Preliminary concepts

Maxwell's equations (table.(2.6)) are the main functions that rules electromagnetism problems. Following the approach used by *Dott. D.R. Wilton* in [44]In case of magnetic and electric current densities, M_v and J_v, aren't zero, Faraday and Ampere's law are:

$$\nabla \times E = -j\omega\mu \cdot H - M_v \tag{5.1}$$

$$\nabla \times H = j\omega\epsilon \cdot E + J_v \tag{5.2}$$

Considering the permittivity and permeability dyadic functions of the position written as

$$\epsilon = \epsilon_r\epsilon_0 \qquad \mu = \mu_r\mu_0 \tag{5.3}$$

useful to consider the dielectric parameters of the medium inhomogeneous and anisotropic.

The two forms of Gauss law must be remembered as

$$\nabla \cdot D = q_v \tag{5.4}$$

$$\nabla \cdot B = m_v \tag{5.5}$$

where q_v and m_v are the electric and magnetic volume charge densities, which are related to their respective current bu *continuity equations*(5.6)-(5.7)

$$\nabla \cdot J_V = -j\omega q_V \tag{5.6}$$

$$\nabla \cdot M_V = -j\omega m_V \tag{5.7}$$

Where V is used to represent the calculation inside a three dimensional space.

Definition of the vector wave equation

In order to correctly formulate the problem the vector wave equations must be defined. Making the divergence to the equations (5.1) and (5.2) and using the identity $\nabla\cdot(\nabla\times A) = 0$ the vector wave equations can be written as

$$\nabla \times (\mu_r^{-1} \cdot \nabla \times E) - k_0^2\epsilon_r \cdot E = -j\omega\mu_0 J_v - \nabla \times (\mu_r^{-1} \cdot M_v) \tag{5.8}$$

$$\nabla \times (\epsilon_r^{-1} \cdot \nabla \times H) - k_0^2\mu_r \cdot H = -j\omega\epsilon_0 M_v + \nabla \times (\epsilon_r^{-1} \cdot J_v) \tag{5.9}$$

Potential field representation

Electric and magnetic field can be represented in terms of potential with

$$E = -j\omega A - \nabla\phi - \frac{1}{\epsilon}\nabla \times F \tag{5.10}$$

$$H = -j\omega F - \nabla\Psi + \frac{1}{\mu}\nabla \times A \tag{5.11}$$

that under homogeneous and isotropic methods the four potential are expressed as

- the magnetic and electric vector potentials

$$A = \mu \int_V J_V(r')G(r,r')dV' \tag{5.12}$$

$$F = \epsilon \int_V M_V(r')G(r,r')dV' \tag{5.13}$$

- the magnetic and electric scalar potentials

$$\phi = \frac{1}{\epsilon} \int_V q_V(r')G(r,r')dV' \tag{5.14}$$

$$\Psi = \frac{1}{\mu} \int_V m_V(r')G(r,r')dV' \tag{5.15}$$

Important equation is the scalar Green function $G(r,r')$, that in a medium with wavenumber $\mathrm{k} = \omega\sqrt{\mu\epsilon}$ is

$$G(r,r') = \frac{e^{-j\kappa R}}{4\pi R} \tag{5.16}$$

where $R = |r - r'|$ describe the distance from a source point located at r' and an observation point in r. This function has the aim to map the scattering between two points through the tetrahedral mesh as in figure (5.2).

5.1.1 Application

In this project, finite element method is chosen because investigated domain is approximate to a 3D non homogeneous medium. This region is divided in the tetrahedral mesh defined in chapter 4, that approximates the region as $\tilde{V} = \bigcup_{e=1}^{E} V^e$, where V_e is a tetrahedron volume.

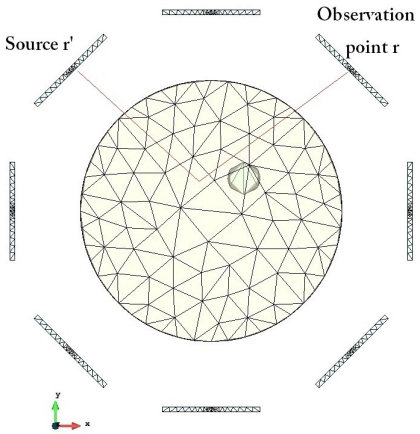

Figure 5.2: Example of scattering path

Base functions definition

Base functions are the equations used to calculate the solution of the problem as a linear combination of them applied on every elements of the mesh. Test function must be able to model curl-free vector fields, requiring continuous tangential component across the boundaries. So as bases functions are defined:

$$\Omega_{ij}^{e} = l_{ij}(\xi_i \nabla \xi_j - \xi_j \nabla \xi_i) \tag{5.17}$$

$$\nabla \times \Omega_{ij}^{e} = 2 l_{ij} \nabla \xi_i \times \nabla \xi_j \tag{5.18}$$

where the i,j indexes represent the edge on it is applied.

Matrix definition

In this paragraph the matrix defined inside the executable are listed:

$$Y_{ij,kl}^{e} = \frac{\sigma_{ij}^{e}\sigma_{kl}^{e}}{j\omega}\Gamma_{ij,kl}^{e} + j\omega\sigma_{ij}^{e}\sigma_{kl}^{e}C_{ij,kl}^{e} \tag{5.19}$$

$$\Gamma_{ij,kl}^{e} = \frac{1}{\mu_0\mu_r^{e}} < \nabla \times \Omega_{ij}^{e}; \nabla \times \Omega_{kl}^{e} > \rightarrow \text{Inductance matrix} \tag{5.20}$$

$$C_{ij,kl}^{e} = \epsilon_0\epsilon_r^{e} < \Omega_{ij}^{e}; \Omega_{kl}^{e} > \rightarrow \text{Capacitance matrix} \tag{5.21}$$

$$I_{i}^{e} = -\sigma_{ij}^{e} < \Omega_{ij}^{e}; J_V > \rightarrow \text{Excitation matrix} \tag{5.22}$$

The Γ and C matrix are analytically evaluated starting from the tetrahedra geometry during the solver execution.

5.2 Problem statement

Affronted situation is an inverse scatterign problem with inhomogeneous medium where there aren't no magnetic current. Under this hypothesis the vector wave equation can be write as:

$$\nabla \times (\mu_r^{-1} \cdot \nabla \times E) - k_0^2 \epsilon_r \cdot E = -j\omega\mu_0 J_V \tag{5.23}$$

where V is the considered volume with perfectly conductive surface, where the absorbing boundary condition was assigned during mesh creation step. This is equivalent to satisfy the Dirichlet condition on the volume boundaries:

$$\hat{n} \times E = 0$$

Testing equation(5.23) with basis function Ω defined in (5.17) and (5.18), the *weak form of the vector wave equation* is obtained in eq.(5.24), which index m represents the degrees of freedom associated to the respective tetrahedra edge.

$$< \Omega_m; \nabla \times (\mu_r^{-1} \cdot \nabla \times E) > -k_0^2 < \Omega_m; \epsilon_r \cdot E >= -j\omega\mu_0 < \Omega_m; J_V > \tag{5.24}$$

Using these set of functions expanding the electric field, it can be described by:

$$E(r) \approx \sum_{n=1}^{N} V_n \Omega_n(r) \tag{5.25}$$

Substituting eq.(5.25) in (5.24), matrix form of the problem is obtained:

$$[Y_{mn}][V_n] = [I_m] \tag{5.26}$$

This process gives as output electromagnetic field inside the inspected media, which example is shown in figure(5.3c). The obtained field is used inside the next step(chapter 6) to solve the scattering inversion problem to get the reconstruction of the dielectric properties of the sample under investigation.

5.3 Output file

At the end of the simulation, the FEM generates two type of files:

- *.VTK* file containing field inside the entire simulated domain (example in figure (5.3c))
- *.txt* file, listing the S parameters for each antenna

These files are then used as input for the TSVD algorithm presented in chapter 6, which aim is the reconstruction of the image.

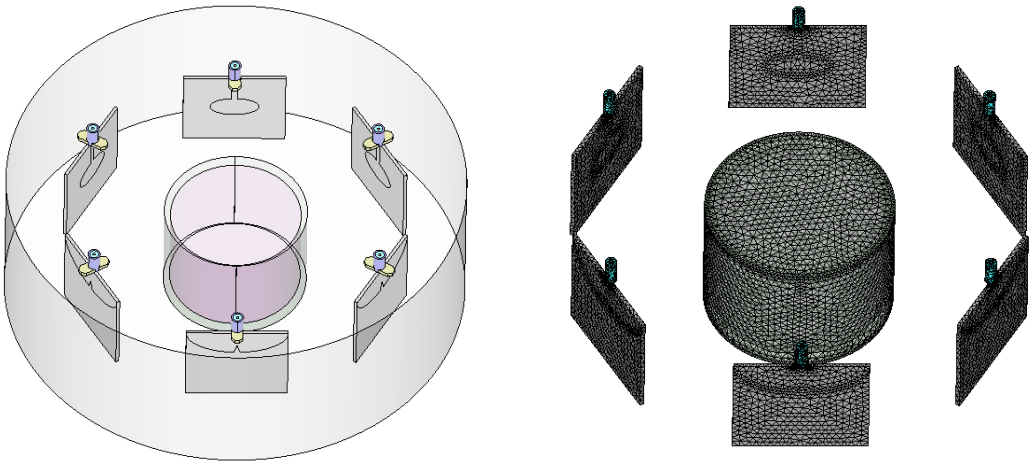

(a) 3D cad **(b)** Tetrahedral mesh

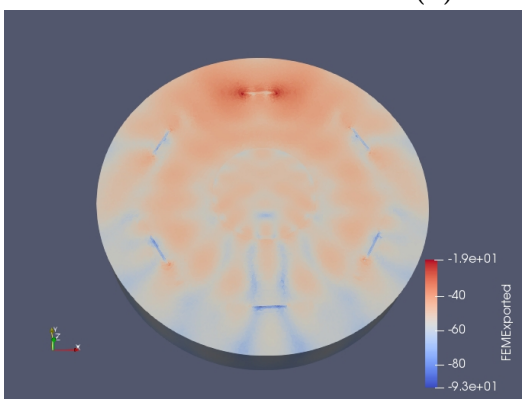

(c) VTK output

Figure 5.3: FEM flow example

5.3.1 Imaging algorithm file setup

In simulation case FEM is applied with placed intrusion and without it, because respectively the imaging algorithm needs the field in the inspected domain and S parameters in case of "clean" jar content and only the scattering parameters in case of intrusion. These are necessary during the simulation steps, while in laboratory test the S parameters are obtained directly from sample measures, but the field inside the jar without any intrusion is generated using FEM, using it as "gold" situation.
So if fields are needed, the VTK file are read using MATLAB[24] scripts, where there is the possibility to choose material and thickness of the interested slice to reconstruct, to get a three dimensional reconstruction. It's obvious that in case of complete 3D reconstruction the slice will is equal to the entire jar. In this project the chosen materials are the ones that fill the jar. The thickness choice is related to the number of tetrahedra that will be processed by the TSVD, conditioning the image generation time. Generally the chosen slice (figure(5.4)) is inside the radiant region of antennae, that usually is characterized by

higher gain value, which means cleaner informations.

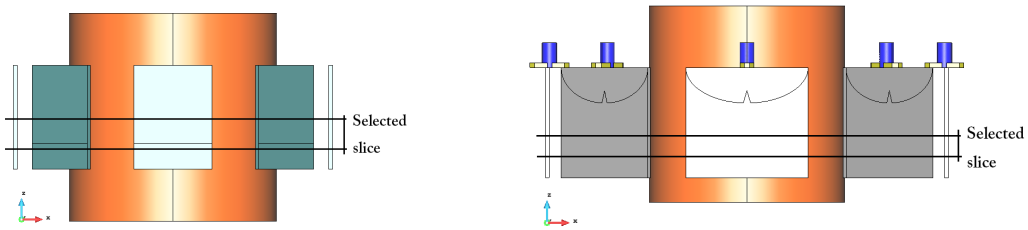

Figure 5.4: Slice cut example

The Scattering parameters files are read by another MATLAB script, whose output will be a matrix n × m, where n and m are respectively the transmitter and receiver antennae. These matrix are used from TSVD to solve the scattering inverse problem to reconstruct the dielectric properties of the sample.

Chapter 6

Truncated singular value decomposition

In this chapter the truncated singular value (TSVD) decomposition is briefly described. In this thesis project TSVD is been used to solve the image reconstruction problem of the investigated domain, starting from the field inside it and scattering parameters in case with and without intrusion. During the simulation steps its inputs are all produced by the FEM, while in laboratory tests S parameters are obtaining directly from VNA measure of the samples.

6.1 Problem statement and inversion procedure

The detection of an intruder inside food is based on the comparison between a reference case, where there is no foreign object, and a sample of the same type, characterizing the algorithm as a differential one, robust against same errors on its inputs. The scattering parameters measurements are taken by the antennae of the MWI system for each frequency of interest, that depends on the inspected material, intrusion dimensions and composition.

Considering only one frequency the electric field ca be written[31] as:

$$E_s(r_p, r_q) = \int_\Omega \underline{\underline{G_e}}(r_p, r) \cdot E(r, r_q)\chi(r)dr \tag{6.1}$$

where parameters are:

r_p: receiver coordinates

r_q: transmitter coordinates

Ω: investigated media volume, which is the material inside the jar

$\underline{\underline{G_e}}$: Green function of reference model

$E(r, r_q)$: total field inside the reference volume

$\chi(r)$: electric constrast. It includes the dielectric properties variations between the investigated scene and the reference one, whose difference is related to foreign object presence

After the definition of the two situations, using the Maxwell's equation linearity, the differential form of the electric field is

$$\Delta E_s(r_p, r_q) = \int_\Omega \left(\underline{\underline{G_e}}(r_p, r) \cdot E^1(r, r_q)\chi^1(r) - \underline{\underline{G_e}}(r_p, r) \cdot E^0(r, r_q)\chi^0(r) \right) dr \tag{6.2}$$

Equation (6.2) is simplified in eq.(6.3) thank to the following:

- Green function is the same in each situation, because the respective reference model is always the same
- It is possible to adopt the Born distorted approximation that assumes negligible variation of the total electric field respect to the contrast, thank to the small variation of χ

$$\Delta E_s(r_p, r_q) = \int_\Omega \underline{\underline{G_e}}(r_p, r) \cdot E^0(r, r_q)\delta\chi_s(r)dr = L_e\delta\chi_s \tag{6.3}$$

This problem is considered as linear, since the operator L_e describes the relation between measured data and the unknown contrast.

$$L_e^0 : \delta\chi_s \in L^2(\Omega) \rightarrow \Delta E_s \in L^2(D) \tag{6.4}$$

The aim is the image reconstruction of contrast variation $\delta\chi_s$ from the scattering parameters difference ΔE_s.

6.1.1 TSVD algorithm application

The truncated singular value decomposition solve the inversion problem using the inversion formula stated in eq.(6.5).

$$\delta\chi_s = \sum_{n=1}^{N} \frac{1}{\sigma_n} < \Delta E_s, U_n > V_n \tag{6.5}$$

Parameters of equation (6.5) are:

$\sigma_n \rightarrow$ singular values of L_e matrix

$U_n \rightarrow$ left singular vector of L_e matrix

$V_n \rightarrow$ right singular vector of L_e matrix

N $\rightarrow$ Truncation factor on the eigenvalue to be considered. It defines the informations quantity considered by the TSVD, influencing the reconstruction stability and image resolution

These variables are characterized by the property $L_e = U_n \sigma_n V_n^*$, obtained using the *svd* function in MATLAB.

Important role is played by the truncation factor that can be considered the threshold between valid information and noise floor. Generally to choose a value, the eigenvalues plot is considered. An example is shown in figure (6.1a).

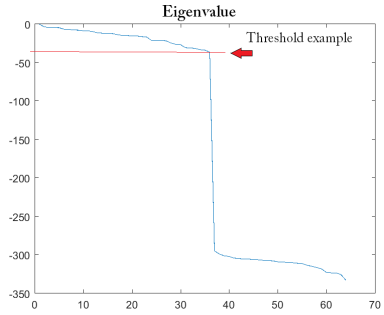

(a) Eigenvalue plot and example of threshold

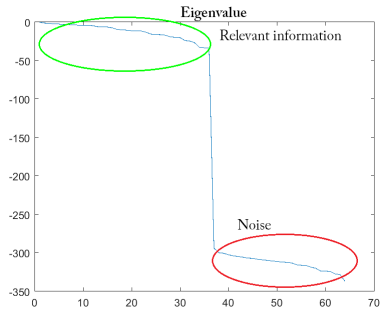

(b) Relevant and noise regions

Figure 6.1: Eigenvalue plot examples

In figure (6.1) two distinct region can be observed, that are underlined in fig.(6.1b). The green one represents the region where the wanted information are located, while the red one, being so low, it includes only information linked to the noise level. Every line drop means information looses, points where the output images can increase in quality and resolution, since the level is far enough from the noise level and from the higher level, where the TSVD acquires too many informations to give a correct detection. In the results section these type of graphs will report only the considered information region. Reference scenario is generated off-line ad-hoc for each type of affronted situation, without compromise the response rate of the system during laboratory tests.

6.1.2 Output file

The output file generated by the TSVD consists of a three dimensional image of the reconstructed dielectric properties of the investigated volume where the presence of the intrusion is signaled by a maximum inside this volume. Its position is freely obtained thank to the scattering parameters references of the TSVD. An example of reconstructed image is in figure (6.2).

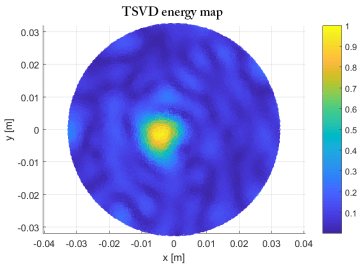

Figure 6.2: Example of the TSVD output

6.2 Calibration of TSVD input data

In laboratory tests a lot of noise takes place, making important the calibration of the TSVD input data, in particularly of the scattering parameters. Noise factors are quite different and can be caused by many elements such as cable losses and phase shifts, mismatches at connectors, differences on same type antennae. These can be removed using the calibration method proposed in [14].

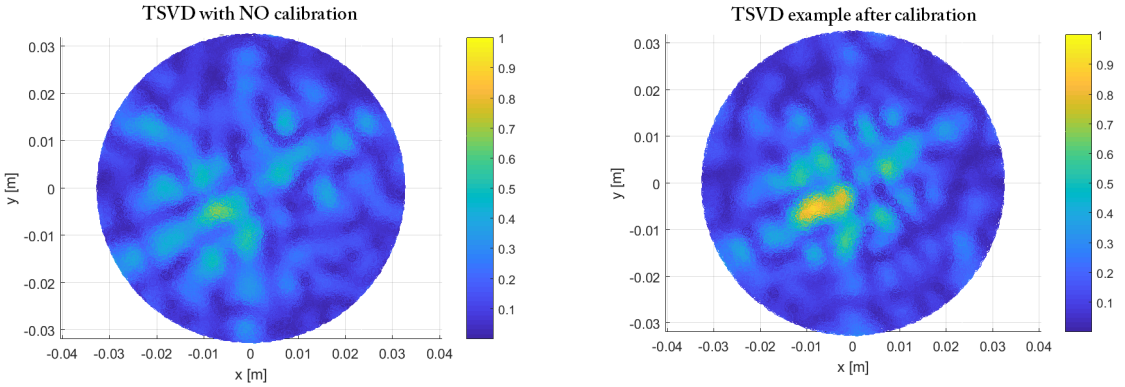

(a) TSVD result with no calibration

(b) TSVD result after calibration

Figure 6.3: Effect of the proposed calibration

This method consists in create values to weigh the original scattering parameters difference using the S parameters of a reference case, in order to mitigate the eventual errors. The main reference scenario is a scattering measure of a metallic cylinder, shown in figure (6.4a) or the empty tank scene can be used.

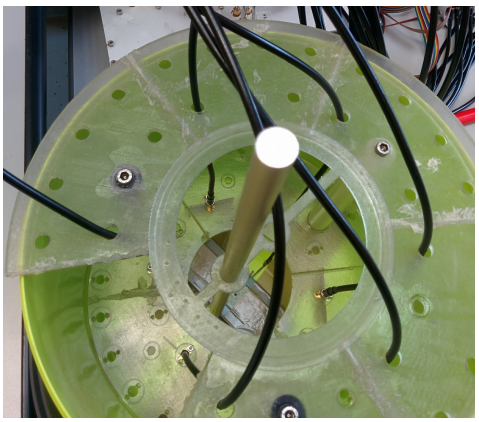

(a) Example of metallic cylinder positioning

The base equation is:

$$\Delta E_{s\,cal} = \frac{\Delta E_s}{S_{21}^{meas\,ref}} S_{21}^{simul\,ref} \tag{6.6}$$

where

- ΔE_s represents the difference of S parameters in case of intrusion presence and its absence
- $S_{21}^{meas\,ref}$ is the measured scattering parameters matrix of the reference scenario
- $S_{21}^{meas\,ref}$ is the simulated scattering parameters matrix of the reference scenario

6.3 Multi-frequency truncated singular value decomposition

The TSVD algorithm applied to a multi-frequency range is not so different to the mono-frequency TSVD already described. The main difference is in the fact that the inputs are organized as the previous procedure, but the same type data are appended for each additional frequency.
The combination of more frequencies data can leads to a cleaner outputs from the noise artifacts.

Chapter 7

Microwave imaging system simulation

This chapter describes the obtained result in simulation condition at various frequency and materials in order to understand the MWI behavior and capabilities. Starting model is a simplified one where the entire jar is composed of the investigating material, after then the model and intrusion are complicated getting closer to real situations. Together with it, the frequency is gradually increased in order to increase the resolution capabilities, that are strongly dependent on dielectric properties of considered materials. The figures (7.1, 7.2) summarize the entire process flow.
Inside the first step the 3D cad and its mesh are generated. Here the mesh is created in order to solve the EM propagation problem using the FEM. Follow the inversion procedure by TSVD algorithm, contrast differences, which inputs are field and scatterer parameters calculated by FEM.

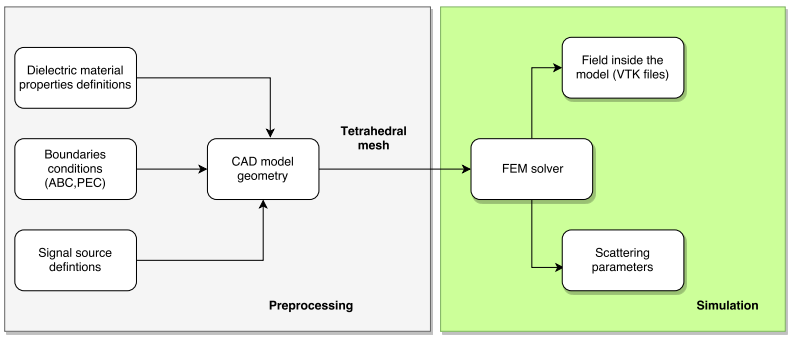

Figure 7.1: 3D model and FEM flow

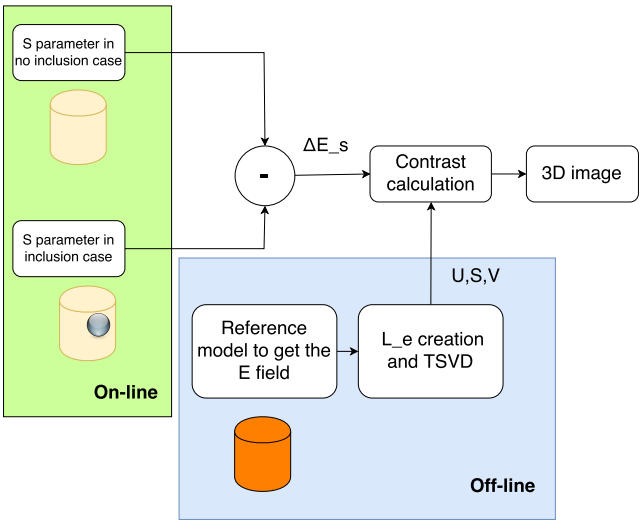

Figure 7.2: TSVD flow

7.1 Model 1: cylindrical inclusion

In these step of verification of the right functionality of the system the investigating model is the jar volume entirely composed of orange marmalade or hazelnut cream based on which case is under test. 8 antenne are posed around the jar as shown in figure(4.14a). So the model without the inclusion is in figure (7.3).

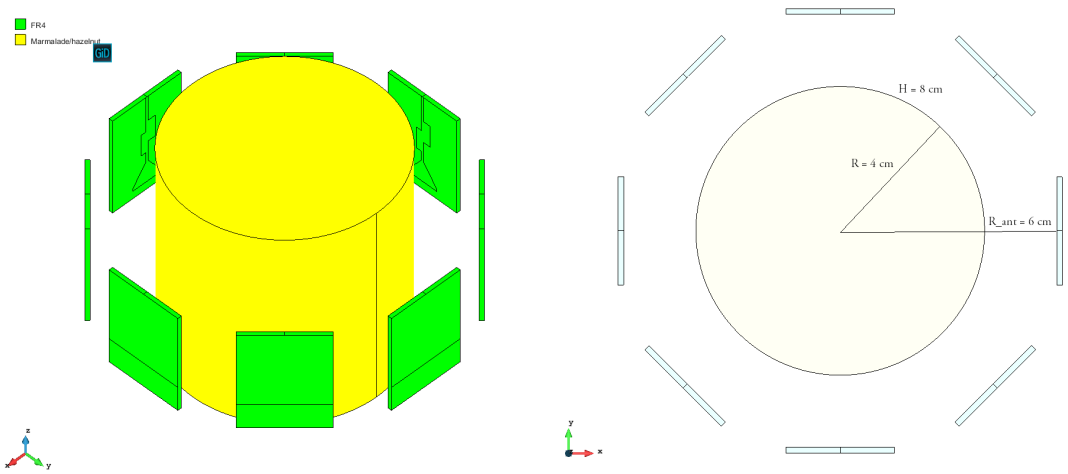

Figure 7.3: Model 1: simplified jar

The first considered inclusion is a cylindric made of air which dimensions are:

radius = 0.5 cm

height = height jar = 8 cm

and with center coordinates $x = 1cm$ e $y = 1cm$, resulting in the model reported in figure (7.4).

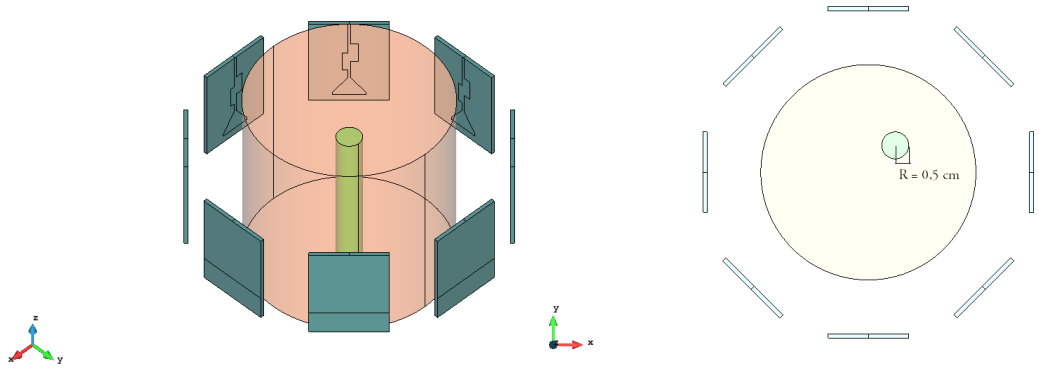

Figure 7.4: Model 1: cylindrical inclusion

For the firsts simulations the inclusion is made of air to get an optimal contrast in terms of dielectric properties with the two explored food types(see tab.(7.1)).

Moreover the figure (7.5) shows the position of each antenna around the jar. These position are assigned in GiD geometry definition (chapter4) and used from the FEM solver(chapter5).

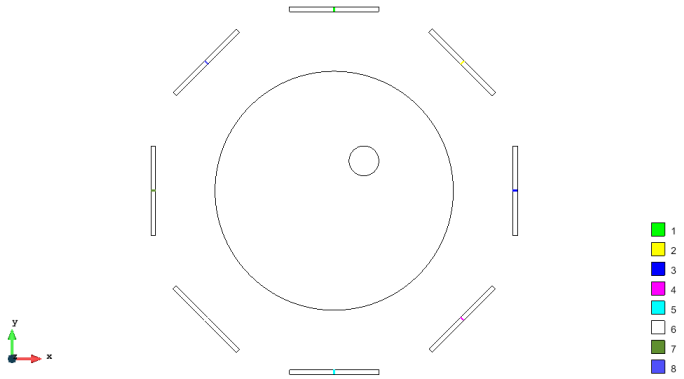

Figure 7.5: Example of positioning

Various frequencies are simulated in order to study the MWI behavior with different dielectric parameters materials. Considering the orange marmalade the field penetration decreases with the frequency because the strong losses due to the higher real part of electric permittivity, typical of material with high water contents. On the other hand hazelnut cream is characterized by a strong oily content that decreases conductivity and permittivity values, making simpler the field penetration at higher frequencies, but noisy at lower

Table 7.1: Some dielectric parameters

Frequency	$1GHz$	$2GHz$	
Orange marmalade	$\sigma = 0.7$ $\epsilon'_r = 35$	$\sigma = 1.7$ $\epsilon'_r = 26.5$	
Hazelnut cream	$\sigma = 0.00065$ $\epsilon'_r = 3.6$	$\sigma = 0.01$ $\epsilon'_r = 3.275$	
Frequency	$2.25GHz$	$2.75GHz$	
Orange marmalade	$\sigma = 1.9$ $\epsilon'_r = 25.05$	$\sigma = 2.29$ $\epsilon'_r = 22.8$	
Hazelnut cream	$\sigma = 0.015$ $\epsilon'_r = 3.28$	$\sigma = 0.027$ $\epsilon'_r = 3.285$	
Middle frequencies	$1.25GHz$	$1.50GHz$	$1.75GHz$
Orange marmalade	$\sigma = 1.08$ $\epsilon'_r = 31.7$	$\sigma = 1.305$ $\epsilon'_r = 29.5$	$\sigma = 1.515$ $\epsilon'_r = 28.01$
Air	$\sigma = 0$ $\epsilon'_r = 1$		

ones.

The expected resolutions, shown in figures (7.6),(7.8), is a parameter useful to understand the minimal dimension of an inclusion that can be seen and it is obtained as

$$\lambda = \frac{c}{f \cdot \sqrt{\epsilon_r}} \tag{7.1}$$

where f is the working frequency and λ is the field wavelength inside the propagation medium. The penetration depth in fig.(7.7) and (7.9)) indicates at which penetration the EM radiation inside the material falls to $1/e$ of its value and it is obtained from

$$PD = \frac{1}{\alpha} \tag{7.2}$$

deriving it from

$$k = \frac{2\pi f}{c}\sqrt{\epsilon'_r - j\epsilon''_r} = \beta - \alpha \tag{7.3}$$

Considering these graphics it's considerable to expect that a lower frequencies jam behavior is better than the hazelnut cream one. Anyway increasing the frequency is useful to make better the resolution of the microwave imaging system.

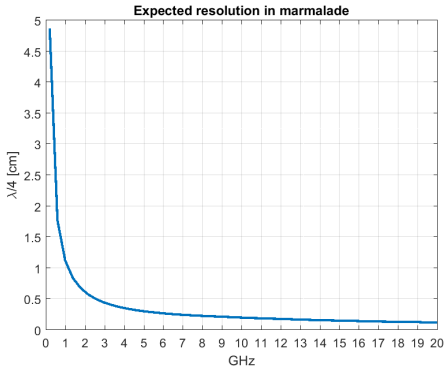

Figure 7.6: Orange marmalade expected resolution

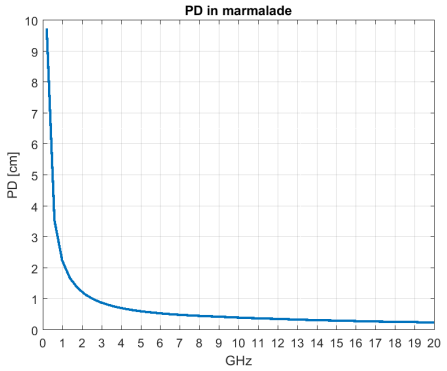

Figure 7.7: Orange marmalade penetration depth

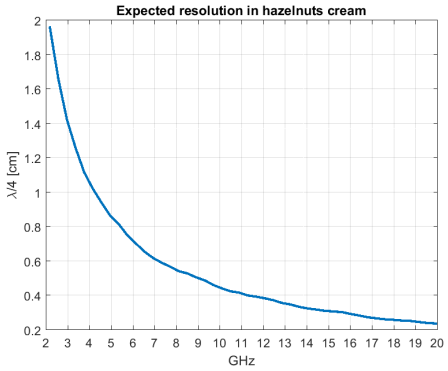

Figure 7.8: Hazelnut cream expected resolution

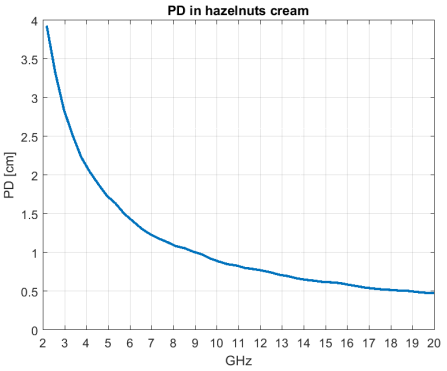

Figure 7.9: Hazelnut cream penetration depth

7.1.1 Numerical analysis at 1 GHz

Case: orange marmalade

- Frequency $= 1GHz$
- Dielectric properties of jam:
  $\sigma_{jam} = 0.7$
  $\epsilon_{real} = 35$
- Background volume: *air*
  $\sigma_{air} = 0$
  $\epsilon_{air} = 1$
- Jar-antenna distance: $2cm$
- Intrusion material: *air*
- Intrusion position: $x = 1cm$, $y = 1cm$

- Intrusion radius: $0.5cm$

At this frequency marmalade offers:

- high difference in dielectric properties between jam and inclusion that ensure an high contrast
- expected resolution of about $1cm$, that is comparable with inclusion dimensions
- penetration depth of about $2cm$

A first result is the difference between the S_{21} scattering parameters of the case with and without the foreign object reported in figure (7.11). This result represents the interaction intensity between each antenna and it is a symmetric matrix with size n = number of the antenna. Each pixel shows the interaction between the antennae i,j. Generally a stronger interaction means the presence of an inclusion near these antennae, since the value are higher than the noise.

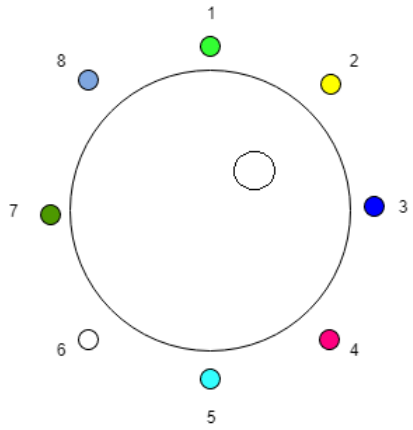

Figure 7.10: Antennae positions respect to the corps

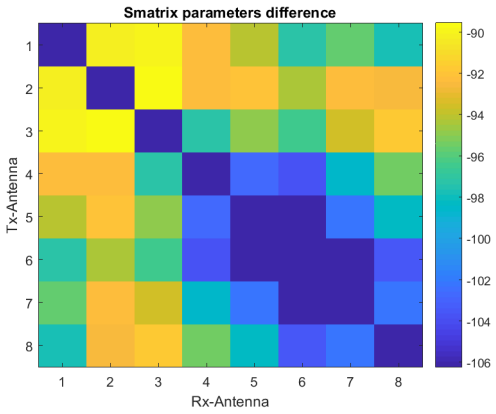

Figure 7.11: Interaction matrix

As the figure (7.11) shows, the antennae with greater interaction are those in proximity of the foreign object (see fig.(7.10)). In fact the position 1, 2, 3 are characterized by a strong interaction thank to the early reflection due to the corp, while going away from the inclusion the interaction becomes weaker. It's important note that the S_{11}, the irradiated power, are imposed to 0 to avoid the saturation of the image scale in case of too high irradiated power. The values range inside figure (7.11) are an information about how far the scattering parameters from the noise level are and if a real measure in the same condition can give satisfactory results, based on:

- higher are the value, simpler it will be got useful result in laboratory test
- smaller is the range and harder will be distinguishing the intrusion from the background

- towards the bottom is that range, harder is discriminate the foreign object from the noise

In this case, even if the monopole doesn't resonate under the -10 dB, these values seems affirm that a real measure that reproduce this case can have high possibilities to give considerable results. Anyway since this is a simulation the system performance depends only to the dielectric parameters of the medium and inclusion, which influence the penetration depth and resolution.

Moreover quality of the results depends on the quantity of information that TSVD receives as input. The reference plot is figure (7.12) where are listed some considered thresholds. From now this plot type will show the interested region only.

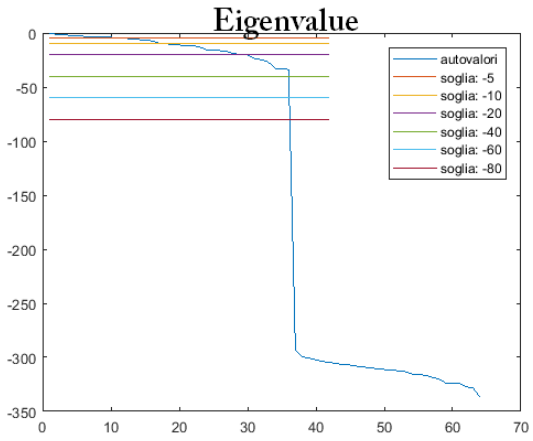

Figure 7.12: Eigenvalues plot

The obtained results from the TSVD algorithm are shown in figure (7.13) in function of the different thresholds. As fig.(7.13a) and (7.13b) display, the algorithm fails to detect the object or simply to locate correctly its position. *However the aim is to have a detection free from noise artifact* in order to establish if inside the sample there is an intrusion. The location is only an information got free thanks to the detection base on scattering parameters and propagation.

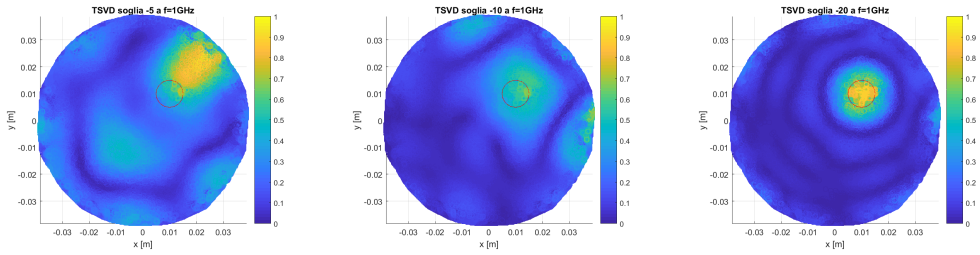

(a) **(b)** **(c)**

Figure 7.13

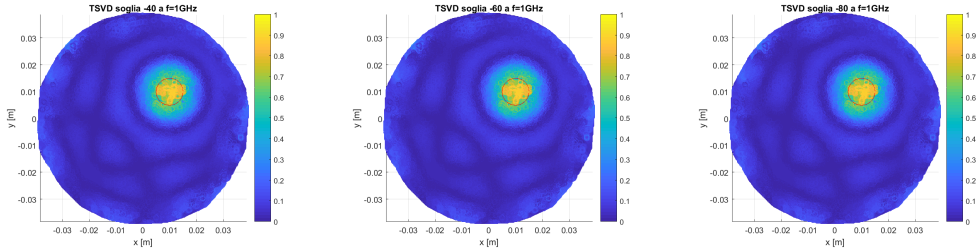

(d) **(e)** **(f)**

Figure 7.13: Energy map obtained from the TSVD: the red circle indicates the inclusion position

Increasing the input informations of TSVD the detection is correct (fig.(7.13c), (7.13d), (7.13e), (7.13f)).

Case: hazelnut cream

- Frequency $= 1GHz$
- Hazelnut cream dielectric properties:
  $\sigma_{nut} = 0.00065$
  $\epsilon_{real} = 3.6$
- Background volume: air
  $\sigma_{air} = 0$
  $\epsilon_{air} = 1$
- Jar-antennae distance: $2cm$
- Inclusion material: air
- Inclusion position: $x = 1cm$, $y = 1cm$
- Inclusion radius: $0.5cm$

It is got at this frequency:

- expected resolution of about 4 cm $\rightarrow$ the field wavelength is too larger respect to the foreign object dimensions. So the detection will not be correct
- high penetration depth

Considering the antennae interaction matrix (fig.(7.14c)), it tells already that the system will not be able to detect correctly the inclusion, because the too low values. This is a direct consequence of the cream low conductivity at low frequencies values. In figure (7.14) are listed the TSVD results varying the information threshold, shown in (7.14b), where the red circle signals the foreign object position.
By the way it's interesting note that varying the color scale, as shown in figures (7.15), the object is detected, but it isn't an acceptable situation.

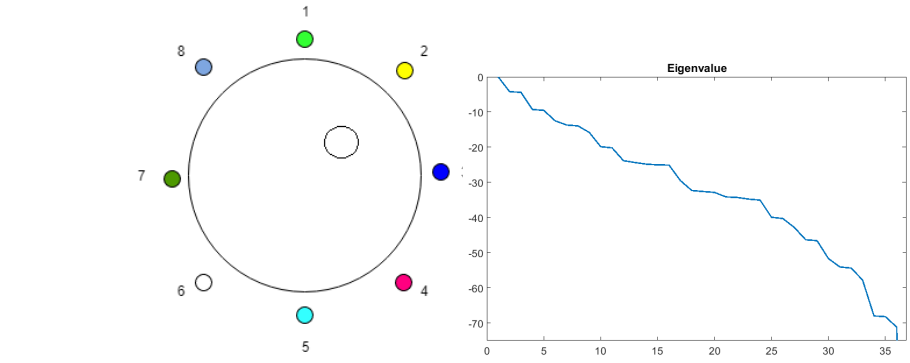

(a) (b)

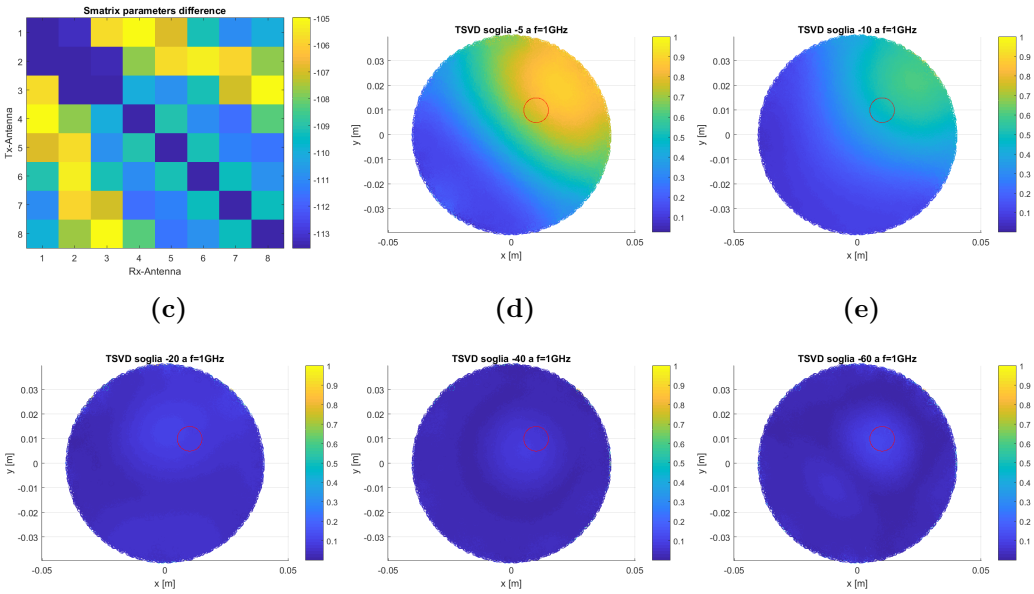

(c) (d) (e)

(f) (g) (h)

Figure 7.14: TSVD outputs

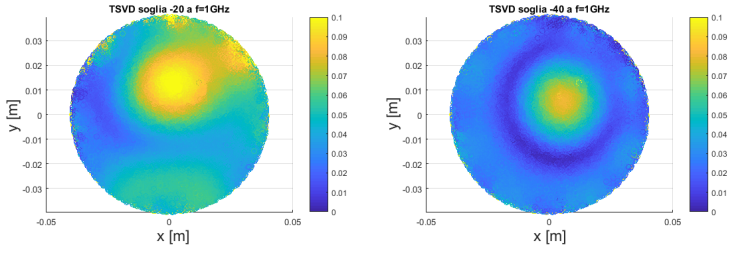

(a) (b)

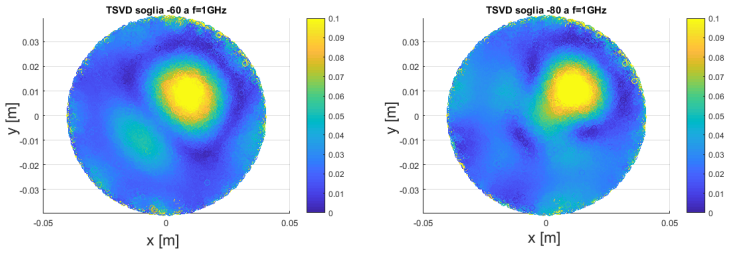

(c) (d)

Figure 7.15: Color scale modified energy maps

7.1.2 Numerical analysis at 2 GHz

Case: orange marmalade

- Frequency $= 2GHz$
- Orange marmalade dielectric properties:
  $\sigma_{jam} = 1.7$
  $\epsilon_{real} = 26.5$
- Background volume: *air*
  $\sigma_{air} = 0$
  $\epsilon_{air} = 1$
- Jar-antennae distance: $2cm$
- Intrusion material: *air*
- Intrusion position: $x = 1cm$, $y = 1cm$
- Intrusion radius: $0.5cm$

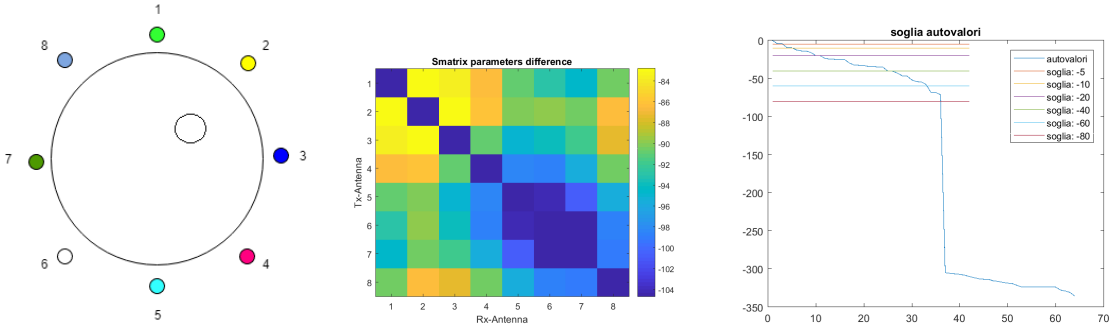

(a) (b) (c)

As in the case with the 1 GHz there is a strong contrast between the two materials, but the expected resolution is lower, because σ is higher increasing field losses inside jam.

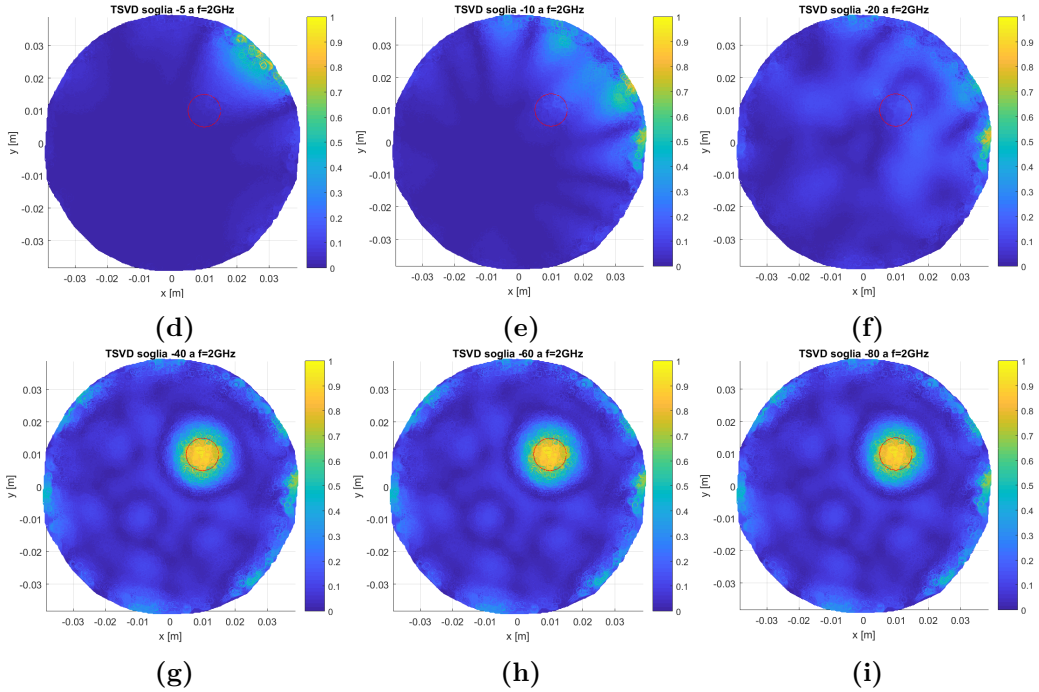

Figure 7.16: TSVD outputs

Increasing the frequency, the results start to show the tendency of the jam to loose field information, dues to the fact the now the system needs more information to give a correct detection.

Case: Hazelnut cream

- Frequency $= 2GHz$
- Hazelnut cream dielectric properties:
  $\sigma_{nut} = 0.01$
  $\epsilon_{real} = 3.275$
- Background volume: air
  $\sigma_{air} = 0$
  $\epsilon_{air} = 1$
- Antennae-jar distance: $2cm$
- Inclusion material: air
- Inclusion position: $x = 1cm$, $y = 1cm$
- Intrusion radius: $0.5cm$

At 2 GH the field penetrates easier inside the cream. This is shown by the clear interaction between the nearest antenna to the object (fig.(7.17b,7.17a)). Moreover expected

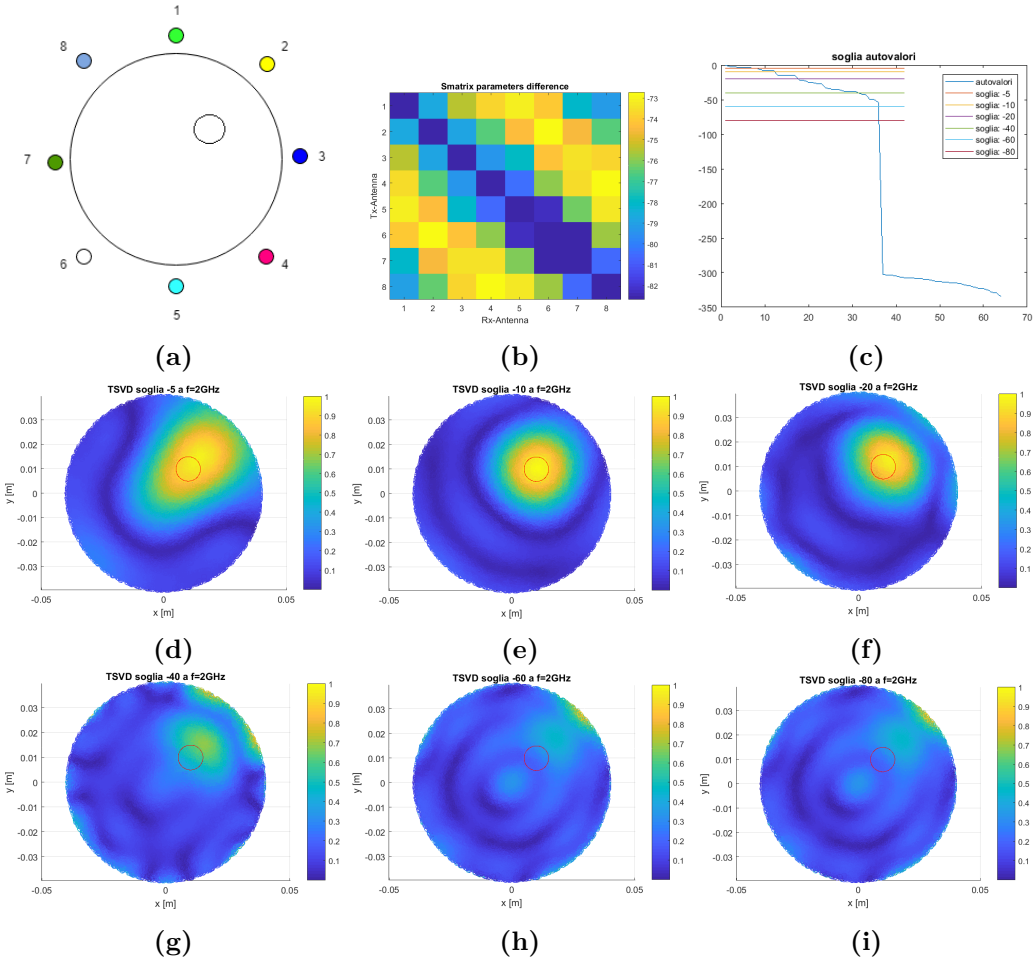

Figure 7.17: TSVD outputs

resolution is comparable with inclusion dimensions. These results are showing the dispersive nature at low frequency of cream, because with more information to the TSVD algorithm, it looses the detection.

7.1.3 Numerical analysis at 2.25 GHz

Case: orange marmalade

- Frequency $= 2.25GHz$
- Orange marmalade dielectric properties:
  $\sigma_{jam} = 1.9$
  $\epsilon_{real} = 25.05$
- Background volume: *air*
  $\sigma_{air} = 0$
  $\epsilon_{air} = 1$

- Antennae-jar distance: $2cm$
- Intrusion material: *air*
- Intrusion position: $x = 1cm$, $y = 1cm$
- Intrusion radius: $0.5cm$

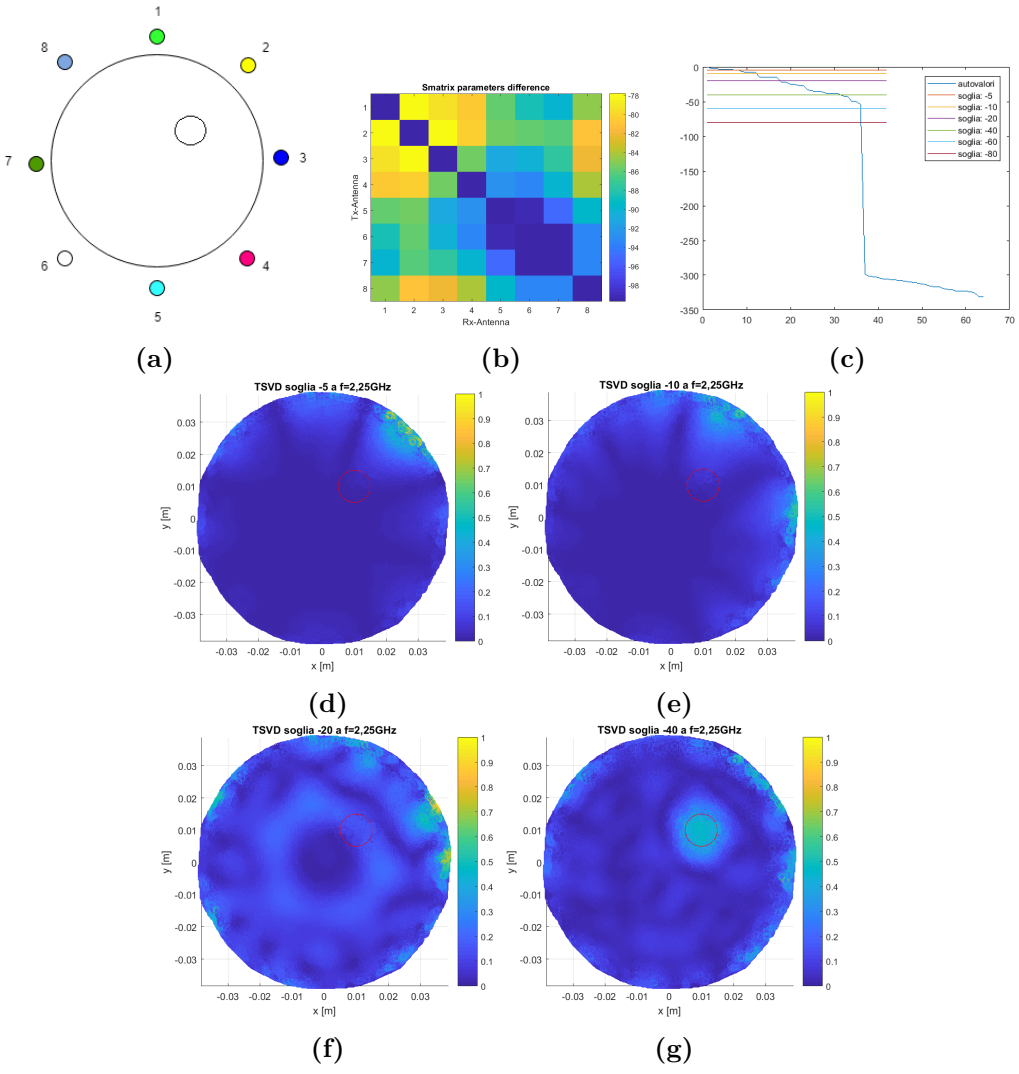

Figure 7.18: TSVD outputs

Considering only the interaction matrix in figure (7.18b) seems that the system can correctly detect the object, but its dimensions are too much smaller than the expected resolution (fig.(7.6)). The results(7.18), as expected, isn't able to detect in a clear way the intrusion.

Case: Hazelnut cream

- Frequency $= 2.25GHz$
- Dielectric properties:
  $\sigma_{nut} = 0.015$
  $\epsilon_{real} = 3.28$
- Background volume: *air*
  $\sigma_{air} = 0$
  $\epsilon_{air} = 1$
- Antennae-jar distance: $2cm$
- Intrusion material: *air*
- Intrusion position: $x = 1cm$, $y = 1cm$
- Intrusion radius: $0.5cm$

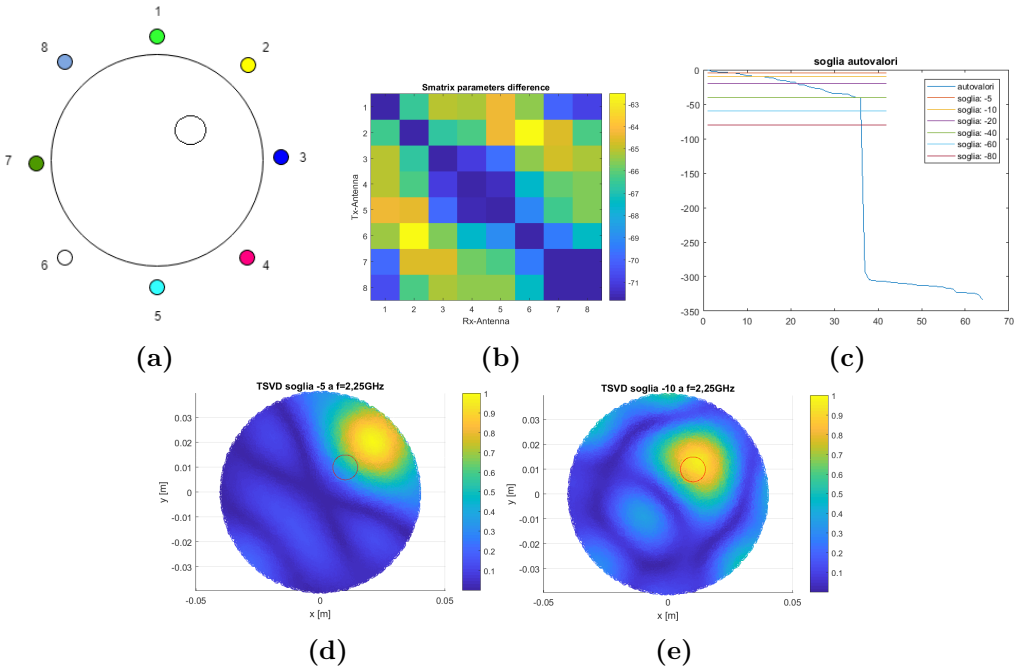

Figure 7.19

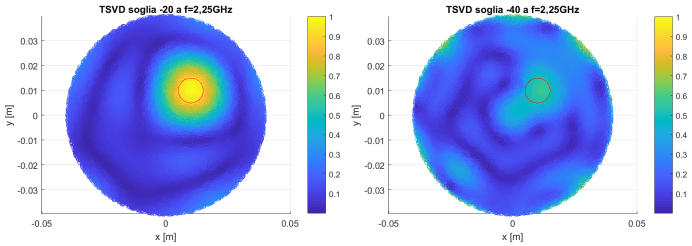

(f) (g)

Figure 7.19: TSVD outputs

Referring to the higher value of the interaction matrix (figure(7.19b)) the system increases its detection capability.

7.1.4 Numerical analysis at 2.75 GHz

Case: orange marmalade

- Frequency $= 2.75GHz$
- Dielectric properties:
  $\sigma_{jam} = 2.29$
  $\epsilon_{real} = 22.8$
- Background volume: *air*
  $\sigma_{air} = 0$
  $\epsilon_{air} = 1$
- Antennae-jar distance: $2cm$
- Intrusion material: *air*
- Intrusion position: $x = 1cm$, $y = 1cm$
- Intrusion radius: $0.5cm$

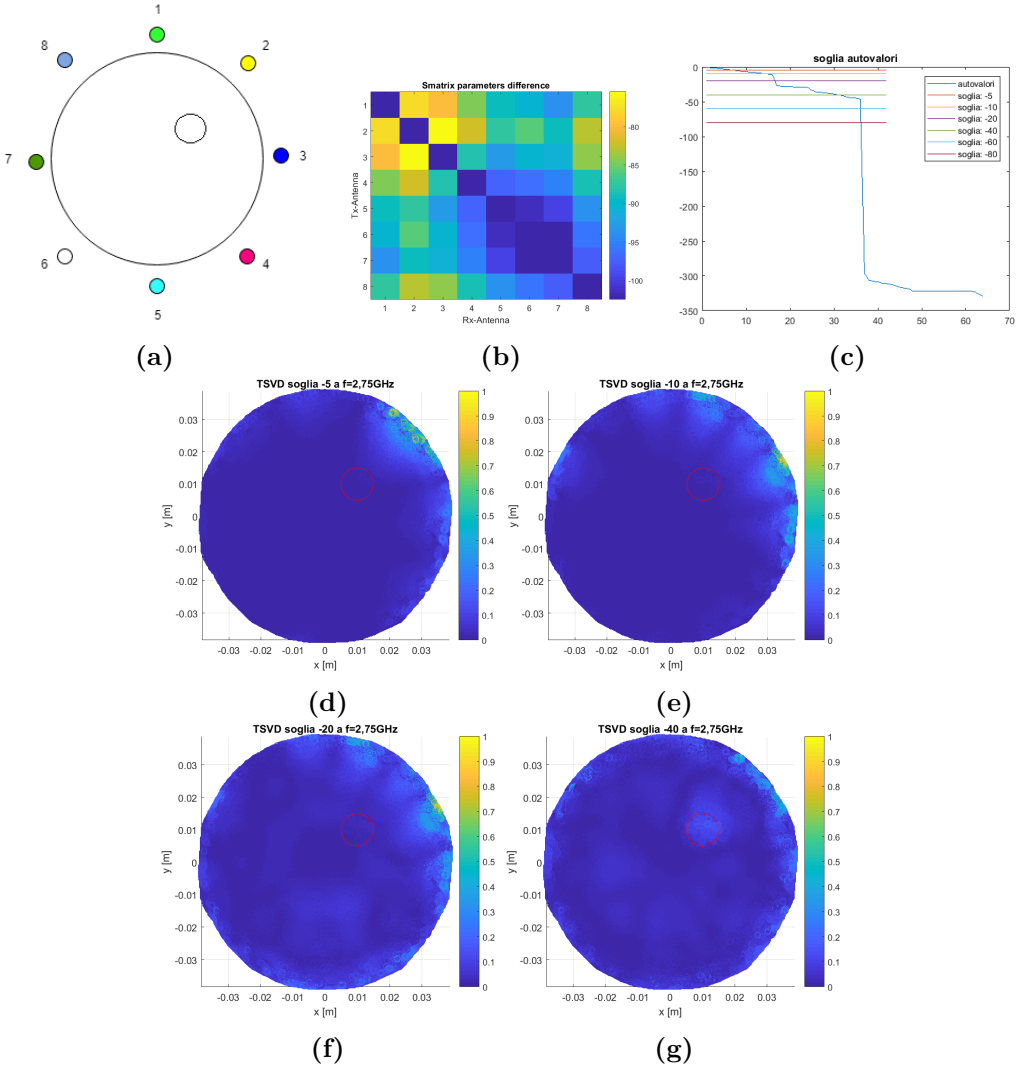

Figure 7.20: TSVD outputs

At this frequency the detection fails because the higher σ of the jam making the field not able to penetrate it.
Also in this situation, varying the color scale detection seems correct.

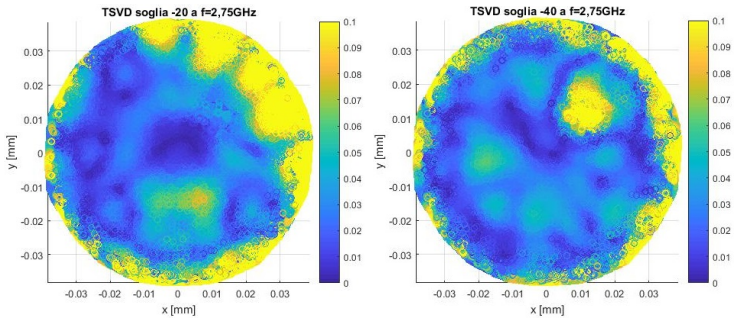

(a) **(b)**

Figure 7.21

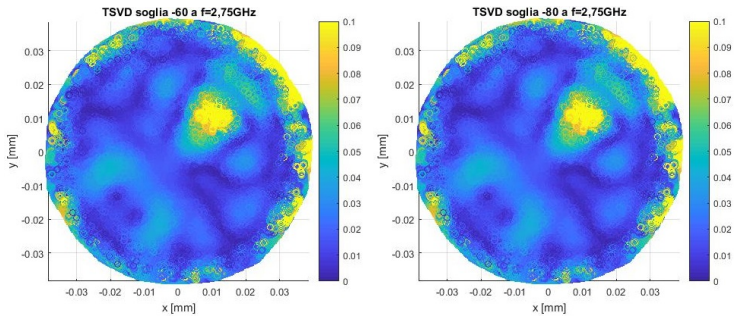

(c) **(d)**

Figure 7.21: Modified color scale TSVD outputs

Case: hazelnut cream

- Frequency $= 2.75GHz$
- Cream dielectric properties:
  $\sigma_{nut} = 0.027$
  $\epsilon_{real} = 3.285$
- Background volume: *air*
  $\sigma_{air} = 0$
  $\epsilon_{air} = 1$
- Antennae-jar distance: $2cm$
- Inclusion material: *air*

- Inclusion position: $x = 1cm$, $y = 1cm$
- Inclusion radius: $0.5cm$

A foreign object with diameter of about 1 cm is clearly visible at this frequency in the cream. It's already understood watching the interaction matrix in figure (7.22b), that is more accurate. In fact the intrusion interaction is underlined near number 1, 2, 3, 4 and 8 antennae, which are the nearest to it.

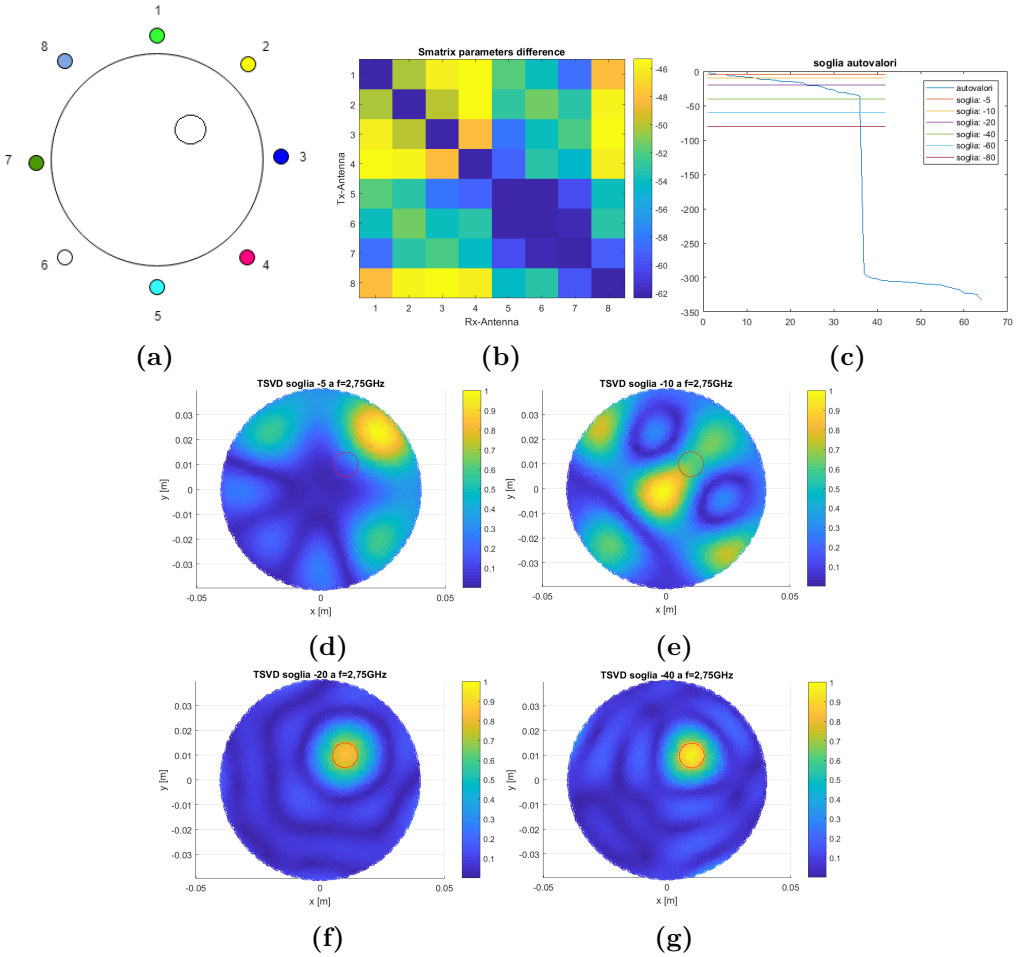

Figure 7.22: TSVD outputs

7.1.5 Additional numerical analysis to study the orange marmalade behavior with the frequency

In this section additional frequencies, between 1 GHz and 2 GHz, are analyzed to better understand why jam isn't penetrable increasing frequency. The system detection capability decreases because the high water content of the marmalade, which influences the dielectric properties, giving it at high conductivity, increasing with the frequency. This behavior

leads to the field incapability to penetrate the material, due to the strong dispersion effects that quickly decrease the field. Moreover the difficulties about the penetration is proved simulating a dummy scenario where the σ parameter of the material to investigate, the jam, is decreased to a value around 0.5, decreasing losses too.

Results at 1.25 GHz

- Frequency $= 1.25GHz$
- Dielectric properties:
  $\sigma_{jam} = 1.08$
  $\epsilon_{real} = 31.7$
- Background volume: *air*
  $\sigma_{air} = 0$
  $\epsilon_{air} = 1$
- Antennae-jar distance: $2cm$
- Intrusion material: *aria*
- Intrusion position: $x = 1cm$, $y = 1cm$
- Intrusion radius: $0.5cm$

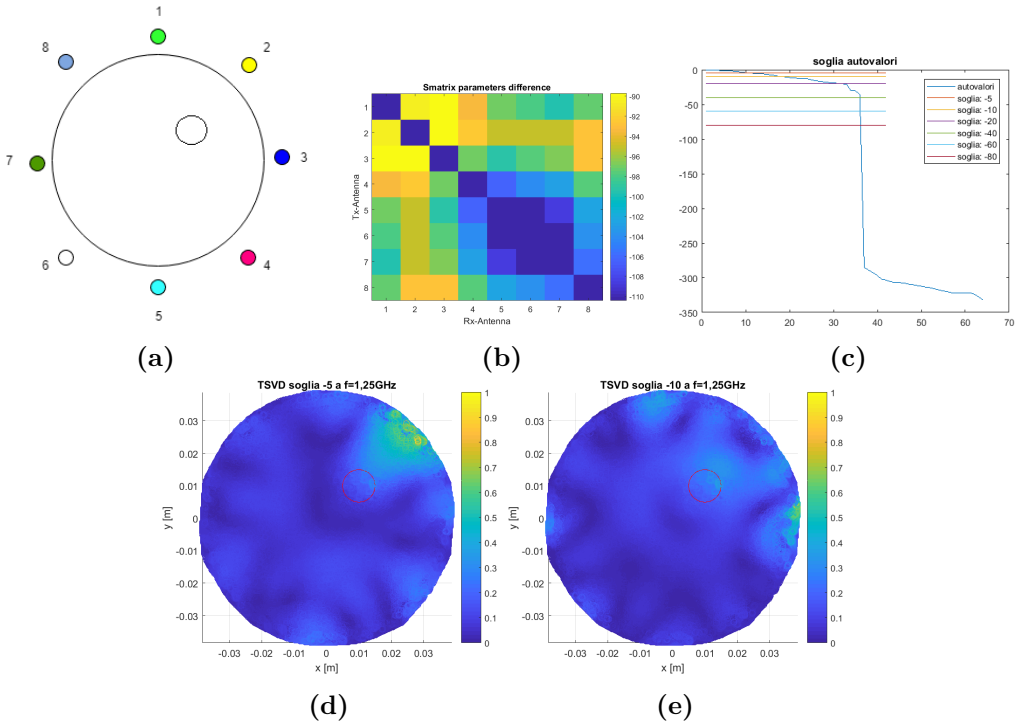

(a) **(b)** **(c)**

(d) **(e)**

Figure 7.23

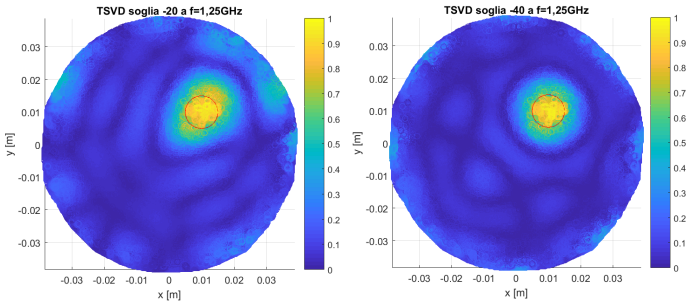

(f) (g)

Figure 7.23: TSVD outputs

As expected the detection is correct, but the influence of the high conductivity can be observed as information looses in figure (7.23f).

Results at 1.50GHz

- frequenza $= 1.50GHz$
- Proprietà dielettriche della marmellata:
  $\sigma_{jam} = 1.305$
  $\epsilon_{real} = 29.5$
- Volume di background: *aria*
  $\sigma_{aria} = 0$
  $\epsilon_{aria} = 1$
- Distanza barattolo-antenne: $2cm$
- Materiale dell'intrusione: *aria*
- Posizione dell'intrusione: $x = 1cm$ e $y = 1cm$
- Raggio dell'intrusione: $0.5cm$

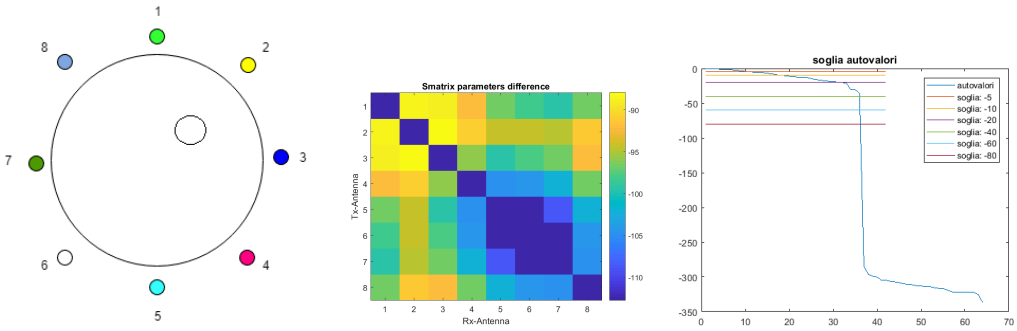

(a) (b) (c)

Figure 7.24

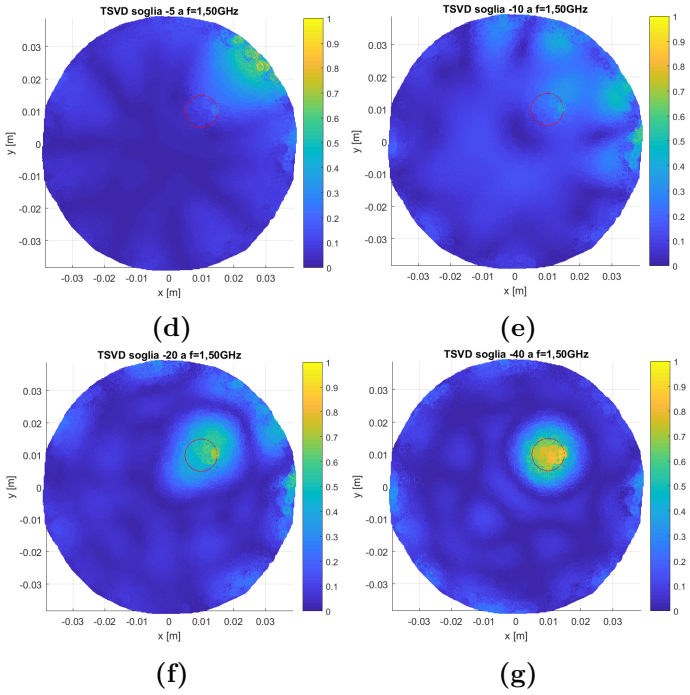

(d) (e)

(f) (g)

Figure 7.24: TSVD outputs

The detection is pretty the same of the previous case, but, due to the higher σ, the detection algorithm needs more information to be accurate.

Results at 1.75GHz

- Frequency $= 1.75GHz$
- Dielectric properties:
  $\sigma_{jam} = 1.515$
  $\epsilon_{real} = 28.01$
- Background volume: *air*
  $\sigma_{air} = 0$
  $\epsilon_{air} = 1$
- Antennae-jar distance: $2cm$
- Inclusion material: *air*
- Inclusion position: $x = 1cm$, $y = 1cm$
- Inclusion radius: $0.5cm$

Respect to the case 7.1.5 the conductivity is increased a little, but not enough to influences the results.

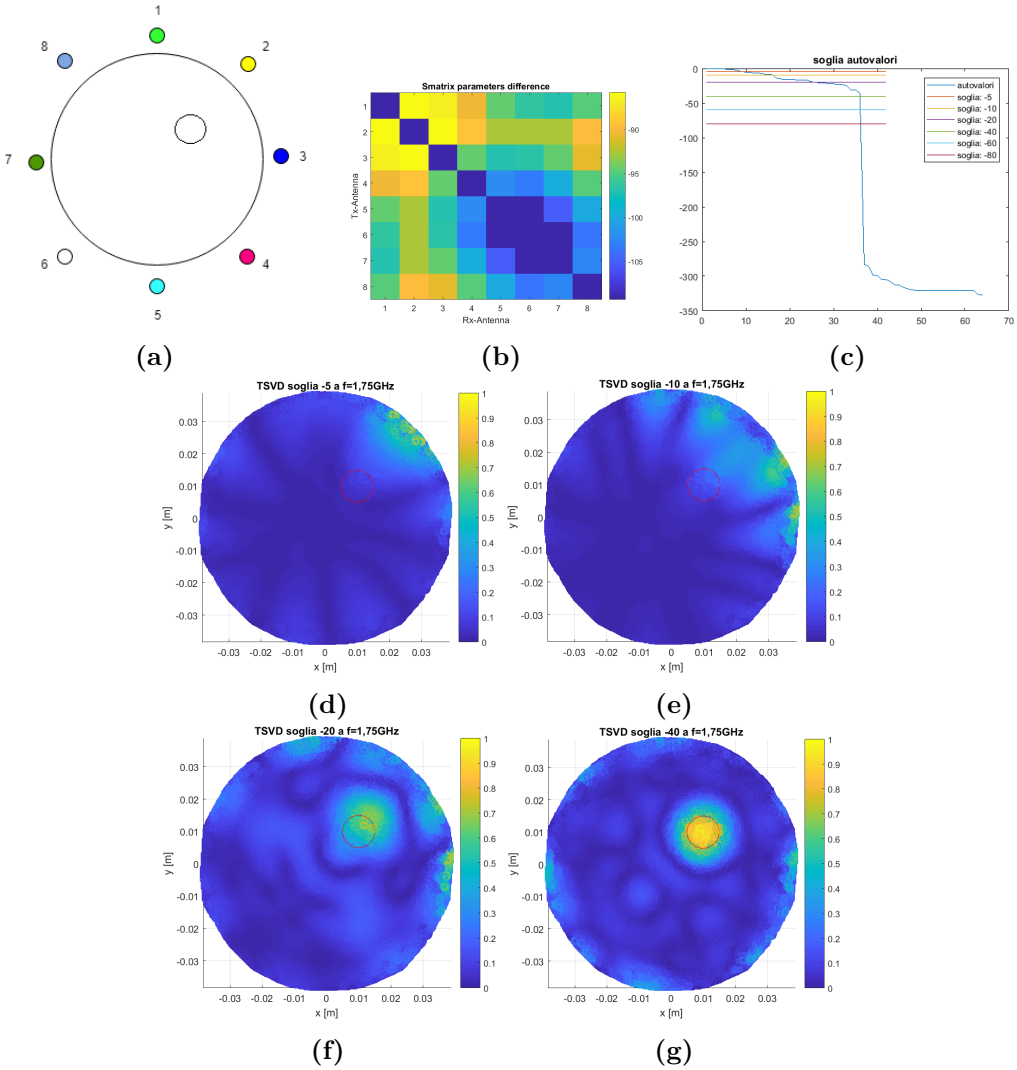

Figure 7.25: TSVD outputs

Specific cases at 2.75GHz

Contrast analysis

Inside the simulation here presented, the real permittivity ϵ_{real} of the inclusion is increased respect to the jam one, in order to get a better contrast in the TSVD reconstructed output.

- Frequency $= 2.75GHz$
- Dielectric properties:
  $\sigma_{jam} = 2.29$
  $\epsilon_{real} = 22.8$
- Background volume: *air*

$\sigma_{air} = 0$
$\epsilon_{air} = 1$

- Antennae-jar distance: $2cm$
- Inclusion material: *air*
- Imposed dielectric properties on the intrusion:
  $\epsilon_{real} = 50$
- Intrusion position: $x = 1cm$, $y = 1cm$
- Intrusion radius: $0.5cm$

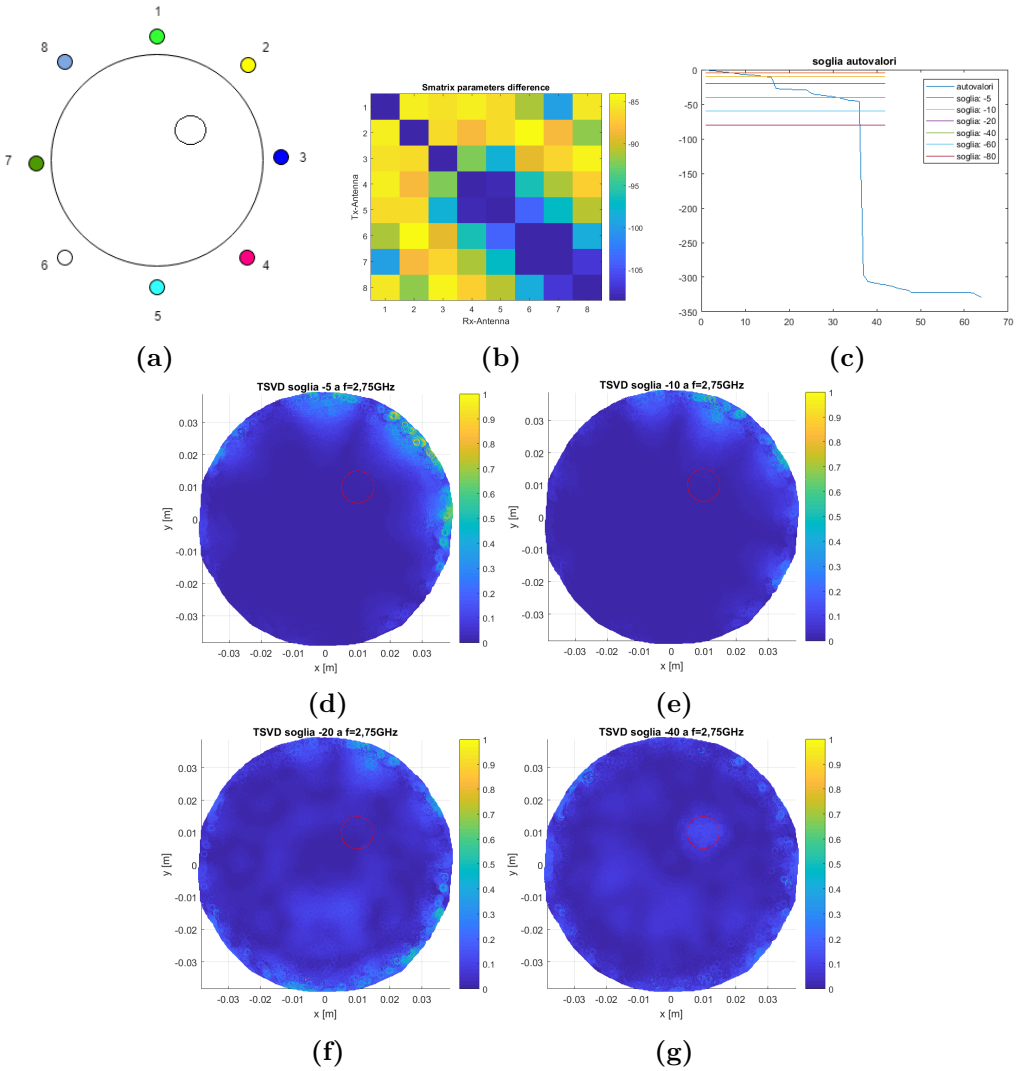

Figure 7.26: TSVD outputs

As the matrix interaction shows (fig.(7.26b)), its values are too small to produce a correct result. This means that the cause of the incorrect detection inside the marmalade with increasing frequency, isn't the contrast that limits the system capability. In this situation, the color axis change(fig.(7.27)) shows the correct detection, but as already state it is not acceptable as results, cause the levels comparable to the noise ones.

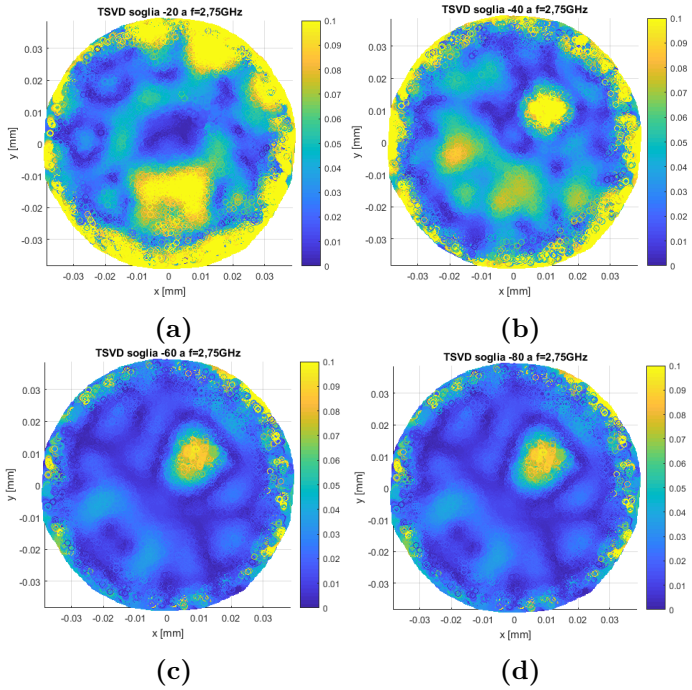

Figure 7.27: Color axis modified TSVD outputs

Attenuation effect analysis

This simulation see a jam σ lower than its real value, in order to limit looses inside the material and favorite then the penetration.

- Frequency $= 2.75GHz$
- Dielectric properties:
  $\sigma_{jam} imposto = 0.5$
  $\epsilon_{real} = 22.8$
- Background volume: *air*
  $\sigma_{air} = 0$
  $\epsilon_{air} = 1$
- Antennae-jar distance: $2cm$
- Inclusion material: *air*

- Inclusion position: $x = 1cm.\ y = 1cm$
- Inclusion radius: $0.5cm$

Considering the high values of the interaction matrix the detection of figure (7.28b) should be correct.

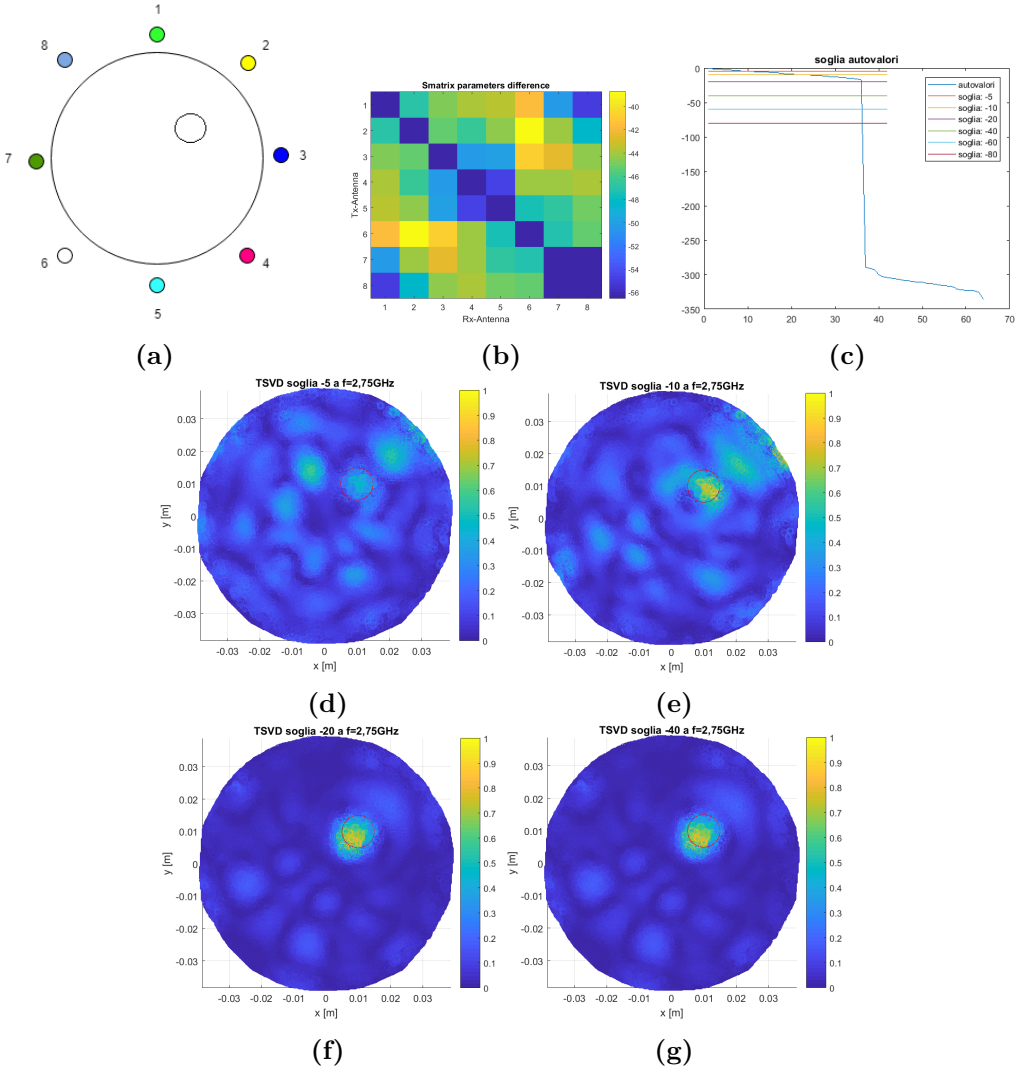

Figure 7.28: TSVD outputs

Results of fig.(7.28) clearly show that decreasing jam looses, the system is able to detect correctly the foreign object.

This is the reason why the detection can't be carried out with the orange marmalade at higher frequencies. Because the high field attenuation dues to the high water content, characterized by high value of conductivity.

7.2 Model 2: cylindrical inclusion

In this section the model with the new ultra wide band antennae, presented in (4.3), is considered, in order to get results at higher frequencies. Higher frequency values make the system able to detect also object with smaller dimensions. The model without the inclusion is the following:

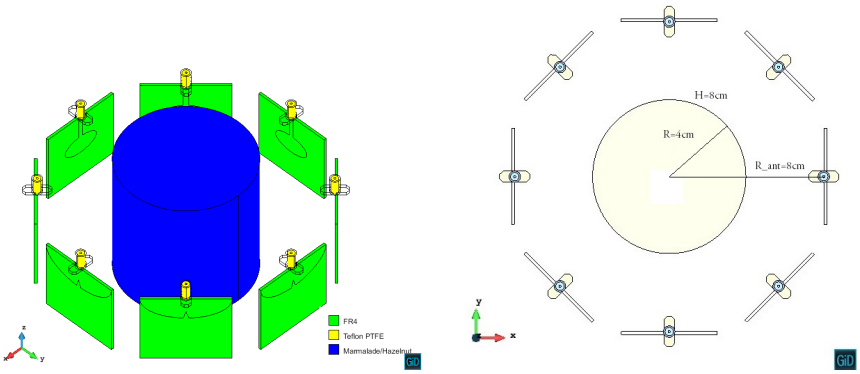

(a) Model material **(b)** UWB antennae positioning

Figure 7.29: Model 2 : simplified jar and UWB antennae

In order to keep constant the antennae number, their position radius is increased at R = 8 cm, as shown in figure(7.29). In these first simulations is also used a cylindrical inclusion positioned in $x = 1cm$, $y = 1cm$ from the system center, as already made.

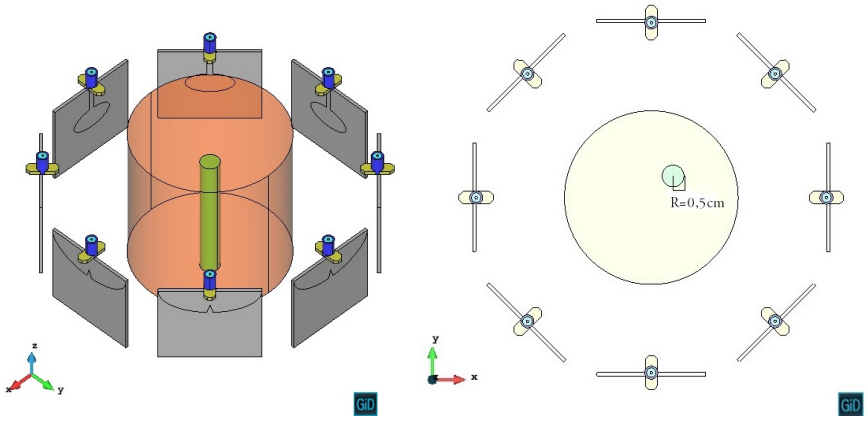

(a) **(b)**

Figure 7.30: Model 2 with the first inclusion

The following image reports the antennae numeration as reference to understand the position towards the inclusion. The dielectric properties of the new material are listed in table (7.2).

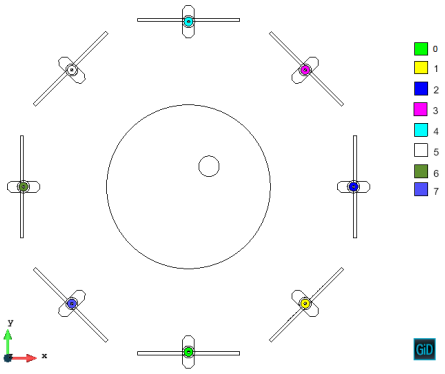

Figure 7.31: UWB antennae numeration

Table 7.2: Dielectric properties of introduce materials

Teflon	$\sigma = 0$ $\epsilon_r' = 2.1$
Aria	$\sigma = 0$ $\epsilon_r' = 1$

7.2.1 Numerical analysis at 2.75 GHz

Orange marmalade

- Frequency $= 2.75GHz$
- Dielectric properties:
  $\sigma_{jam} = 2.29$
  $\epsilon_{real} = 22.8$
- Background volume: *air*
  $\sigma_{air} = 0$
  $\epsilon_{air} = 1$
- Antennae-jar distance: $4cm$
- Inclusion material: *air*
- Inclusion position: $x = 1cm$, $y = 1cm$
- Inclusion radius: $0.5cm$

Orange marmalade simulation at this frequency, using the new antennae, gives slightly better result than with the older antennae, because at this it value they have higher S_{11} values. In fact the detection is only a slight Halo on its correspondence, but in this way it can't be considered anyway.

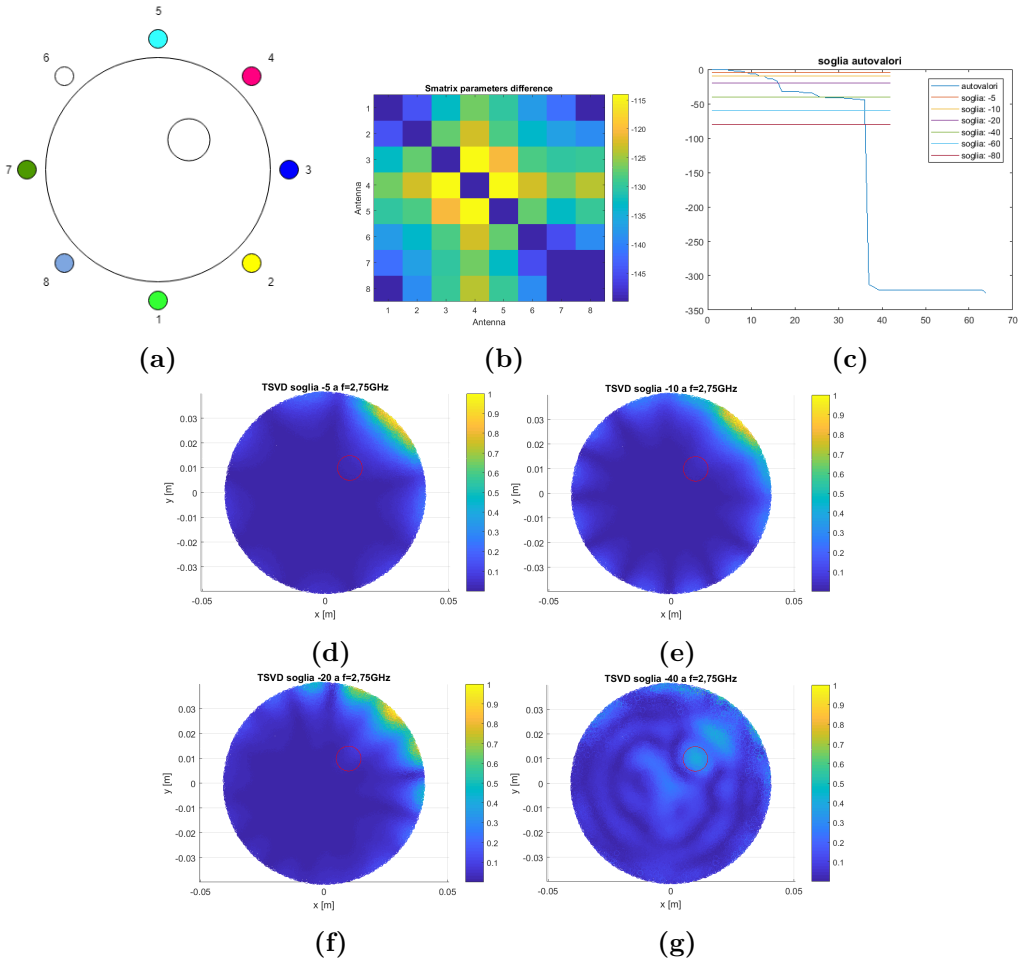

Figure 7.32: TSVD outputs

Case: Hazelnut cream

- Frequency $= 2.75GHz$
- Dielectric properties:
  $\sigma_{nut} = 0.027$
  $\epsilon_{real} = 3.285$
- Background volume: *air*
  $\sigma_{air} = 0$
  $\epsilon_{air} = 1$
- Antennae-jar distance: $4cm$
- Inclusion material: *air*
- Inclusion position: $x = 1cm$, $y = 1cm$

- Inclusion radius: $0.5cm$

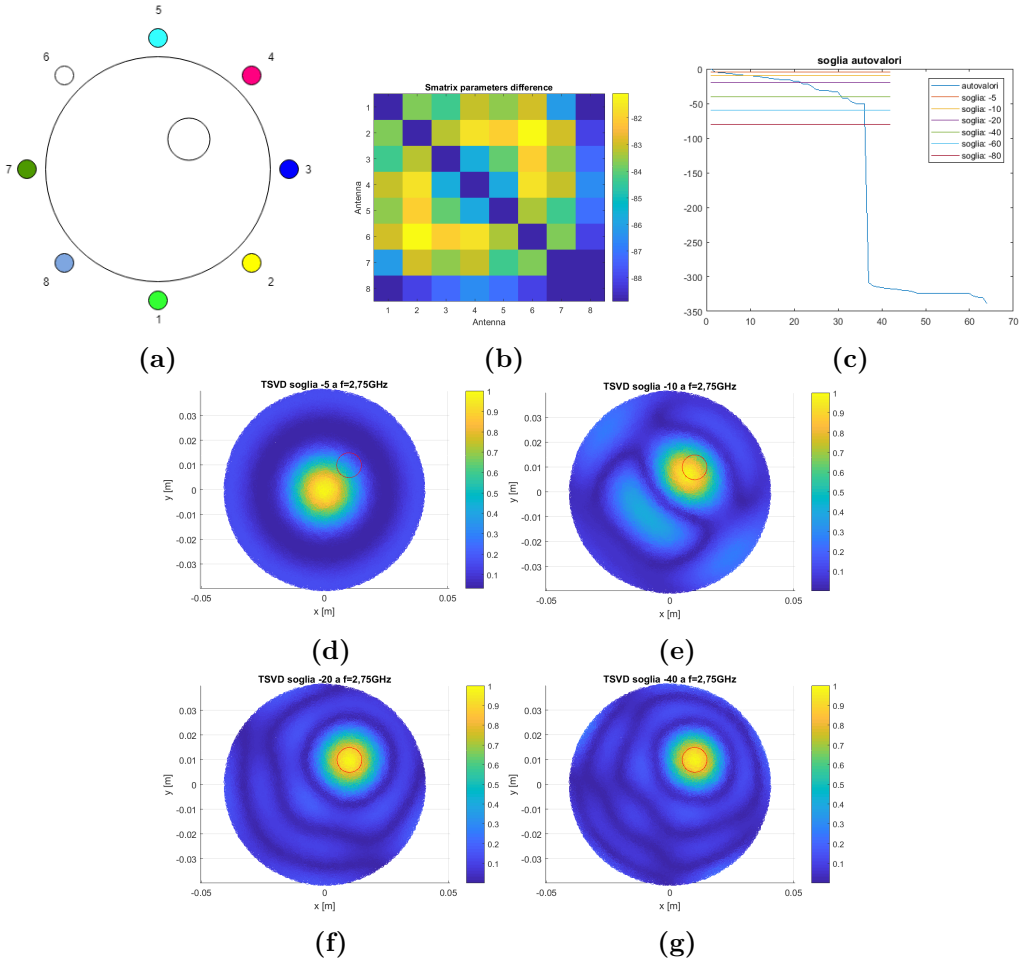

Figure 7.33: TSVD outputs

As expected, the results are correct.

7.2.2 Numerical analysis at 3,25GHz

- Frequency $= 3.25GHz$
- Dielectric properties:
  $\sigma_{nut} = 0.04$
  $\epsilon_{real} = 3.3$
- Background volume: *air*
  $\sigma_{air} = 0$
  $\epsilon_{air} = 1$
- Antennae-jar distance: $4cm$

- Inclusion material: *air*
- Inclusion position: $x = 1cm$, $y = 1cm$
- Inclusion radius: $0.5cm$

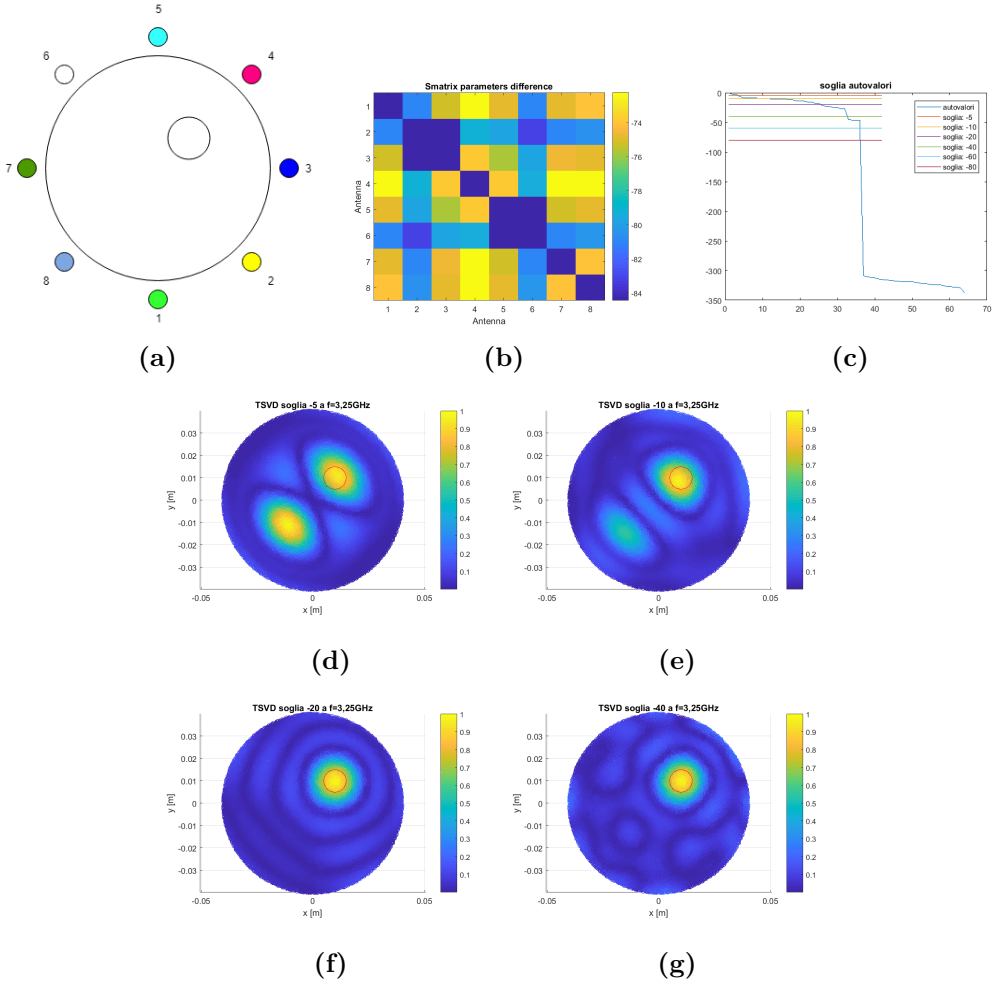

(a) **(b)** **(c)**

(d) **(e)**

(f) **(g)**

Figure 7.34: TSVD outputs

Increasing the frequency, MWI system shows a correct behavior. In figure (7.34d) an artifact is also detect, probably because the informations are cut too early and there is the possibility that at this frequency the inclusion position is at $\lambda/4$ multiple for this value, that cause the double position detection.

7.3 Model 2: spherical inclusion

Here the considered inclusion is a spherical object. The system detection capabilities are studied varying the working frequency and the sphere radius, which is made of air, then of

plastic. As long as the system has a correct function in a determinate frequency, the radius sphere will be decreased until its position will be loosed. So the frequency is increased again and radius decreased. From here only the hazelnut cream is analyzed, because, as already demonstrated in section 7.1.5, microwave imaging doesn't function at higher frequency with marmalade.

7.3.1 Case: air spherical inclusion at 2.75 GHz

General parameters

- Dielectric properties:
  $\sigma_{nut} = 0.027$
  $\epsilon_{real} = 3.285$
- Background volume: *air*
  $\sigma_{air} = 0$
  $\epsilon_{air} = 1$
- Antennae-jar distance: $4cm$
- Inclusion material: *air*
- Inclusion position: $x = 0.5cm$, $y = 0.5cm$, $z = 3.8cm$

Results with inclusion radius: 0.5 cm

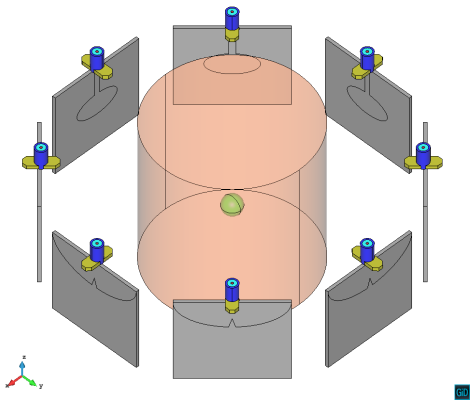

Figure 7.35: 3D model

Being pretty similar to the cylindrical case, the detection takes place correctly. Anyway interaction matrix is characterized by low values, meaning that in a laboratory test, the results might could not be positive.

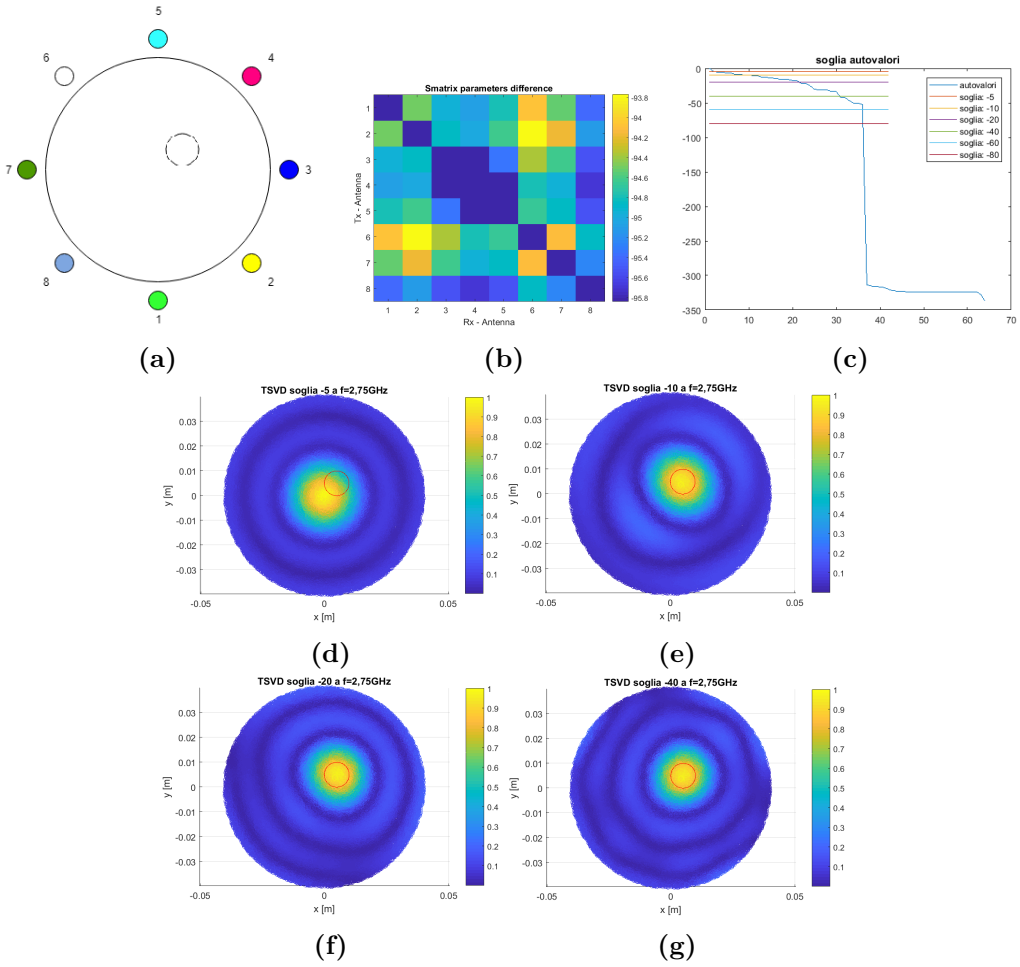

(a) (b) (c)

(d) (e)

(f) (g)

Figure 7.36: TSVD outputs

Results with inclusion radius: 0.25 cm

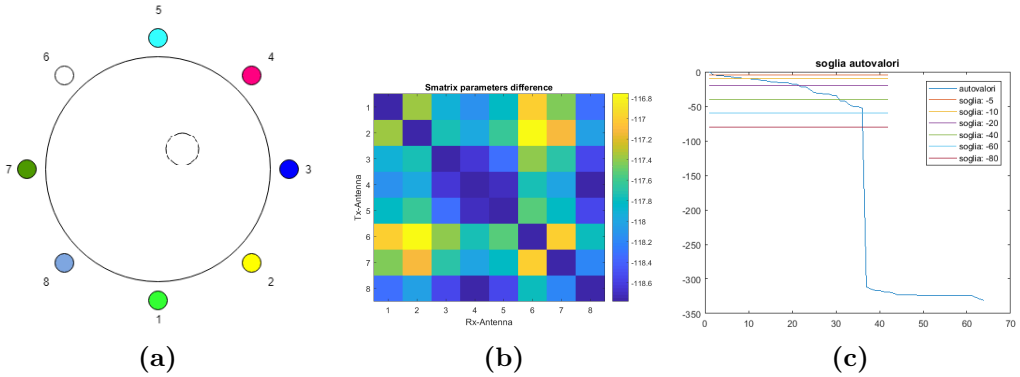

(a) (b) (c)

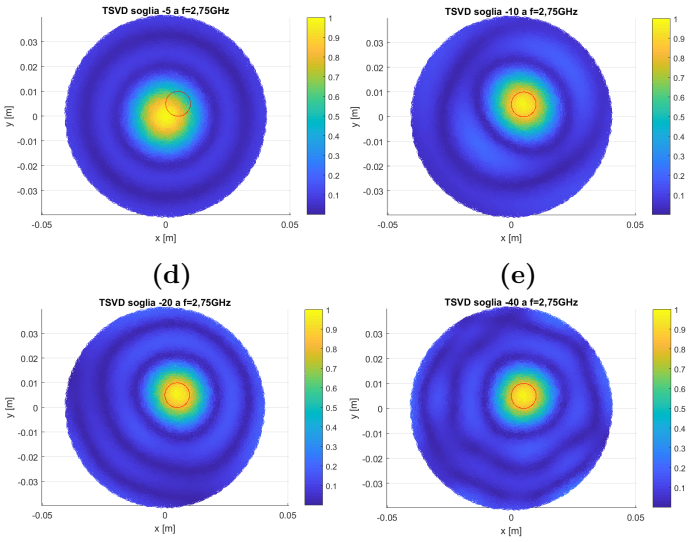

(d) (e)

(f) (g)

Figure 7.37: TSVD outputs

The detection of a sphere with radius 0.25 cm is correct, but it is a numerical simulation, but its quality is lesser than the previousc case considering the interaction matrix values (fig.7.37b)

Results with inclusion radius: 0.125cm

In this case the difference between the expected resolution at this frequency inside the hazelnut cream and inclusion dimension is too high, decreasing the detection quality of the simulated system. So it is necessary increase the frequency to detect smaller object.

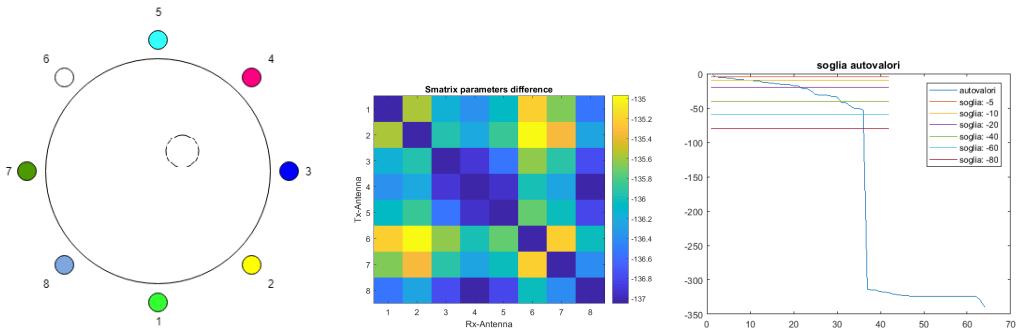

(a) (b) (c)

Figure 7.38

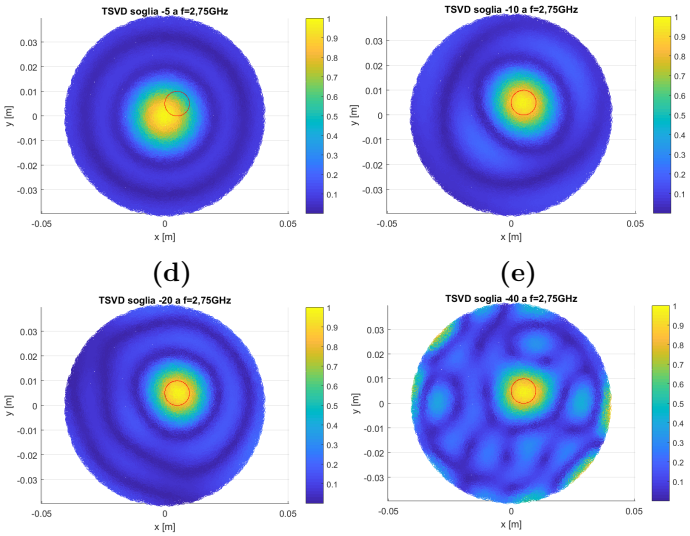

(d) (e)

(f) (g)

Figure 7.38: TSVD outputs

7.3.2 Case: air spherical inclusion at 3.25 GHz

General parameters

- Dielectric properties:
  $\sigma_{nut} = 0.04$
  $\epsilon_{real} = 3.3$
- Background volume: *air*
  $\sigma_{air} = 0$
  $\epsilon_{air} = 1$
- Antennae-jar distance: $4cm$
- Inclusion material: *air*
- Inclusion position: $x = 0.5cm$, $y = 0.5cm$, $z = 3.8cm$

Results with inclusion radius: 0.125cm

Thanks to the increased frequency the detection algorithm shows correct results, but considering the low difference between the scattering parameters, aren't enough to set a correct functionality in a laboratory test. By the way, being in simulation leads to the possibility to decrease again the sphere radius.

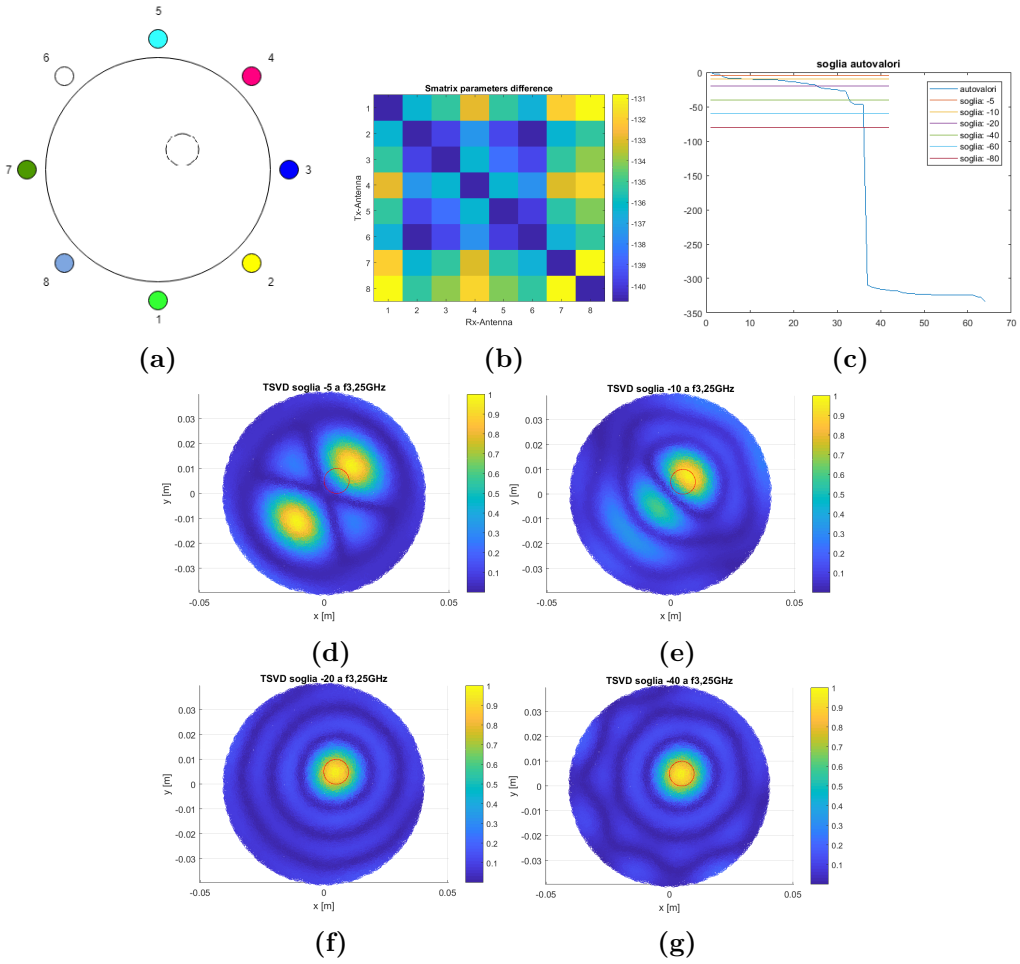

Figure 7.39: TSVD outputs

Results with inclusion radius: 0.0625cm

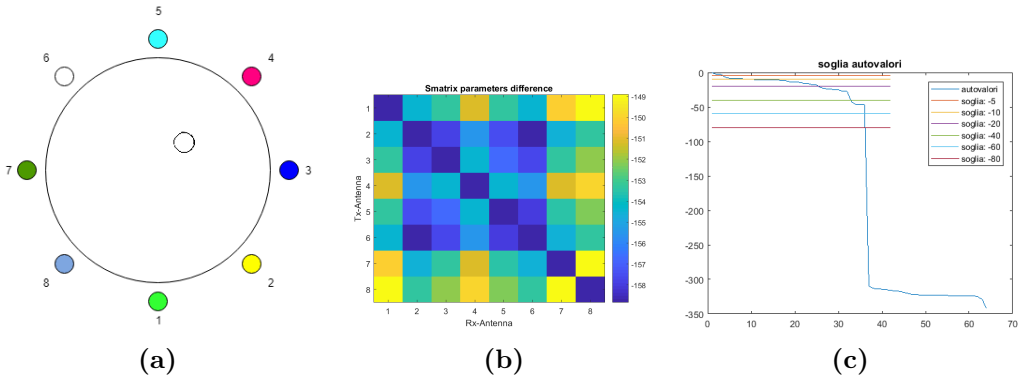

Figure 7.40

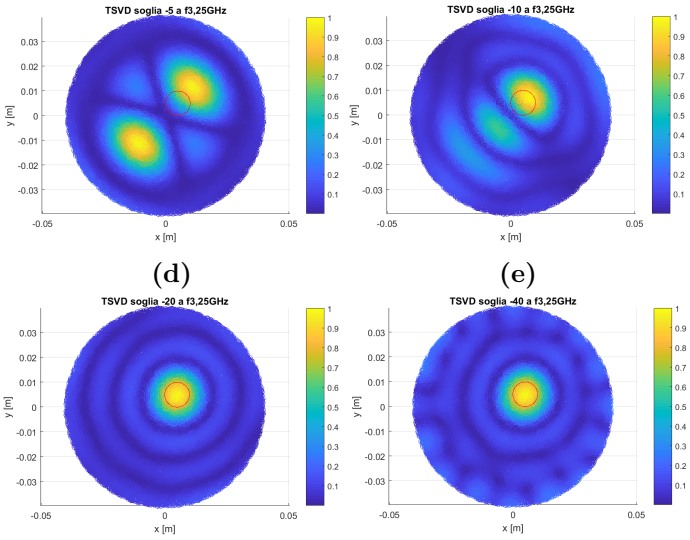

(d) (e)

(f) (g)

Figure 7.40: TSVD outputs

In this case also the detection is positive, but considering the expected resolution around $1.5cm$ and the smaller object dimensions, noise is no more negligible.

Results with inclusion radius: 0.03125cm

WIth this object dimensions, the reconstruction algorithm is able to detect it, but the frequency need to increase. Anyway to obtain acceptable laboratory result the working frequency must be at much higher values, in order to avoid the noise and non "ideal" instrumentation.

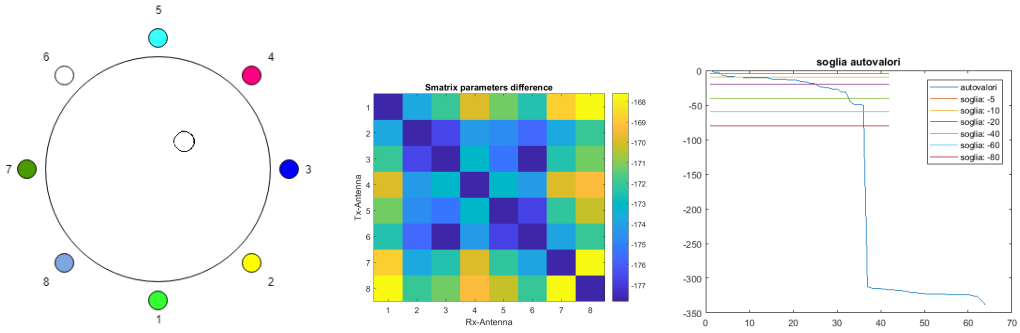

(a) (b) (c)

Figure 7.41

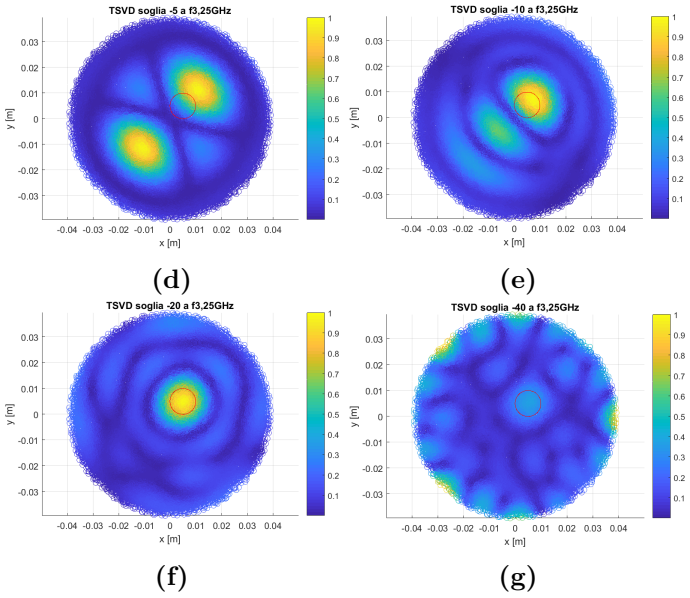

Figure 7.41: TSVD outputs

7.3.3 Case: plastic spherical inclusion at 2.75 GHz

General parameters

- Dielectric properties:
  $\sigma_{nut} = 0.027$
  $\epsilon_{real} = 3.285$
- Background volume: *air*
  $\sigma_{air} = 0$
  $\epsilon_{air} = 1$
- Antennae-jar distance: $4cm$
- Inclusion material: *plastic*
  $\sigma_{plastic} = 0$
  $\epsilon_{plastic} = 2.3$
- Inclusion position: $x = 0.5cm$, $y = 0.5cm$, $z = 3.8cm$

In this section simulations are made considering a plastic material intrusion, as in a real case. Because its permittivity is closer to the hazelnut cream value, a decrease in detection capability is expected, since the contrast between the two material is lower. For this reason will be also necessary increase the frequency in a real measurement.

Results with inclusion radius: 0.5cm

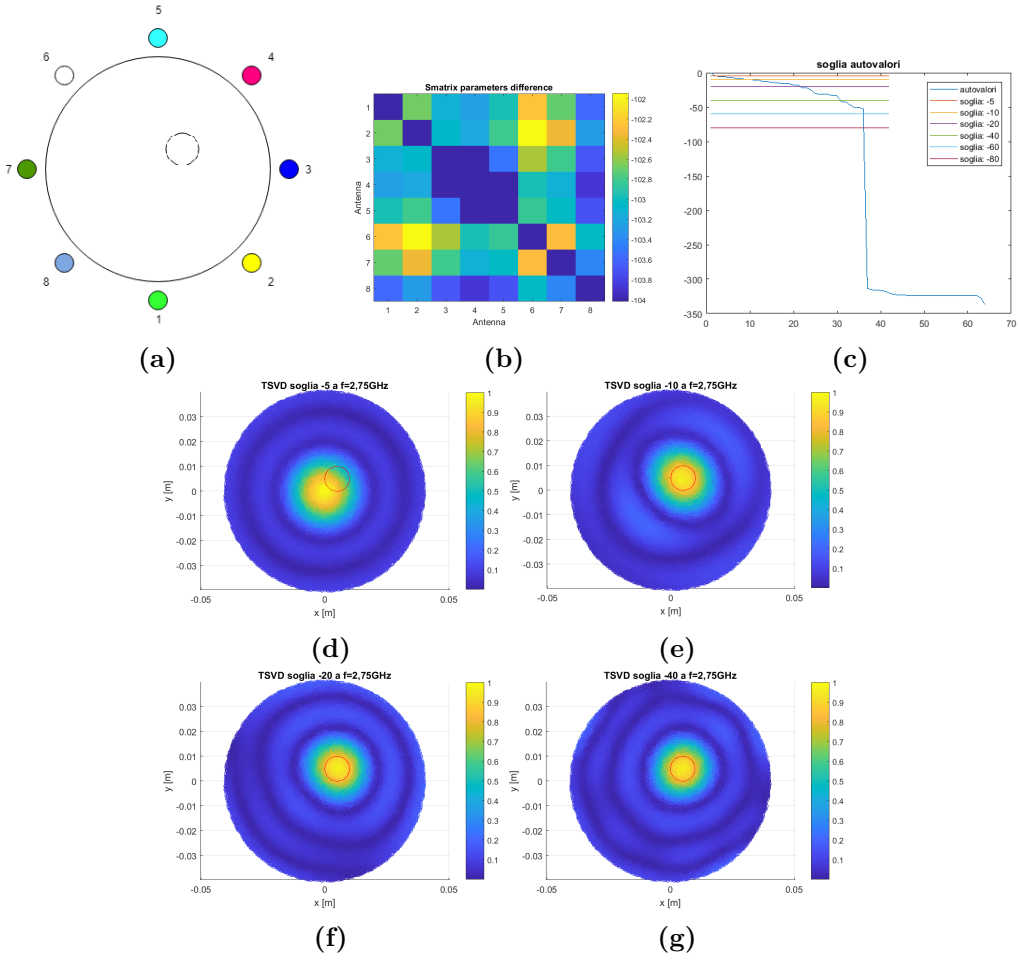

Figure 7.42: TSVD outputs

The detection is positive, but the the difficulty dues to the lower contrast between the cream and plastic is showed by the interaction matrix values (fig.(7.42b)), much lower than the respective air object case(fig.(7.36b)).

Results with inclusion radius: 0.25cm

Compared to the respective case in figures (fig.(7.37b) and (7.37)), the system already shows detection problems, linked to the low contrast materials.

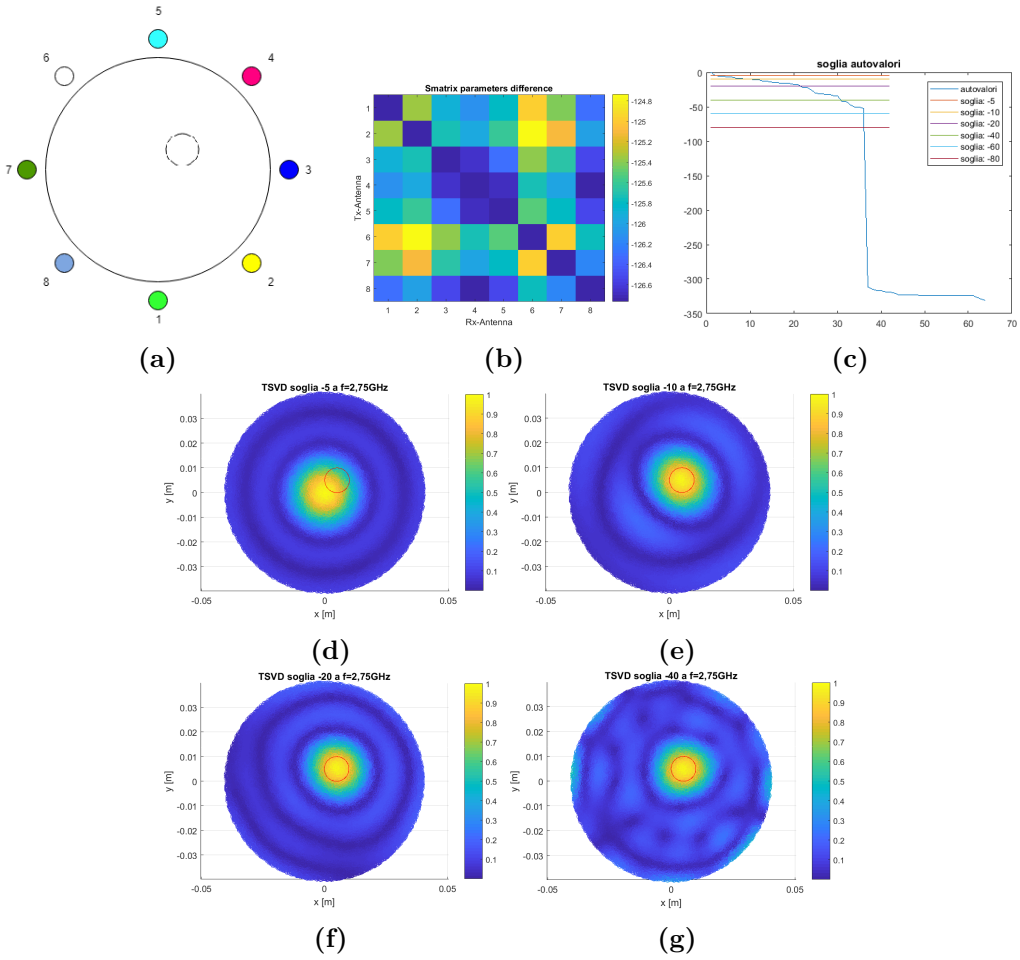

Figure 7.43: TSVD outputs

7.3.4 Case: plastic spherical inclusion at 3.25 GHz

General parameters

- Dielectric properties:
  $\sigma_{nut} = 0.04$
  $\epsilon_{real} = 3.3$
- Background volume: *air*
  $\sigma_{air} = 0$
  $\epsilon_{air} = 1$
- Antennae-jar distance: $4cm$
- Inclusion material: *plastic*
  $\sigma_{plastic} = 0$
  $\epsilon_{plastic} = 2.3$

- Inclusion position: $x = 0.5cm$, $y = 0.5cm$, $z = 3.8cm$

Results with inclusion radius: 0.25cm

The system shows a correct functionality. The interaction matrix of figure ((7.44c)) seems to see the object in a different position, because it considers the artifact visible in picture (7.44d) dues to the low data provide to the TSVD. Increasing them, the output increases in quality.

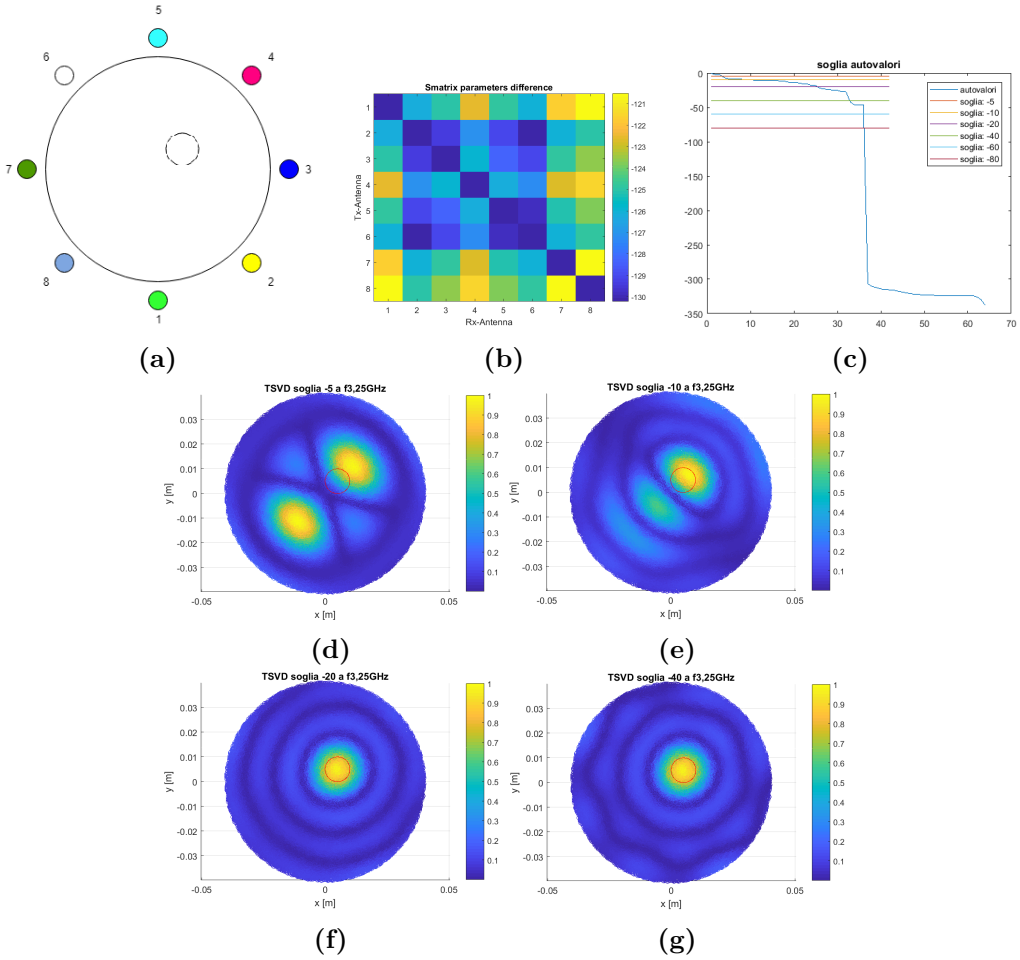

Figure 7.44: TSVD outputs

Results with inclusion radius: 0.125cm

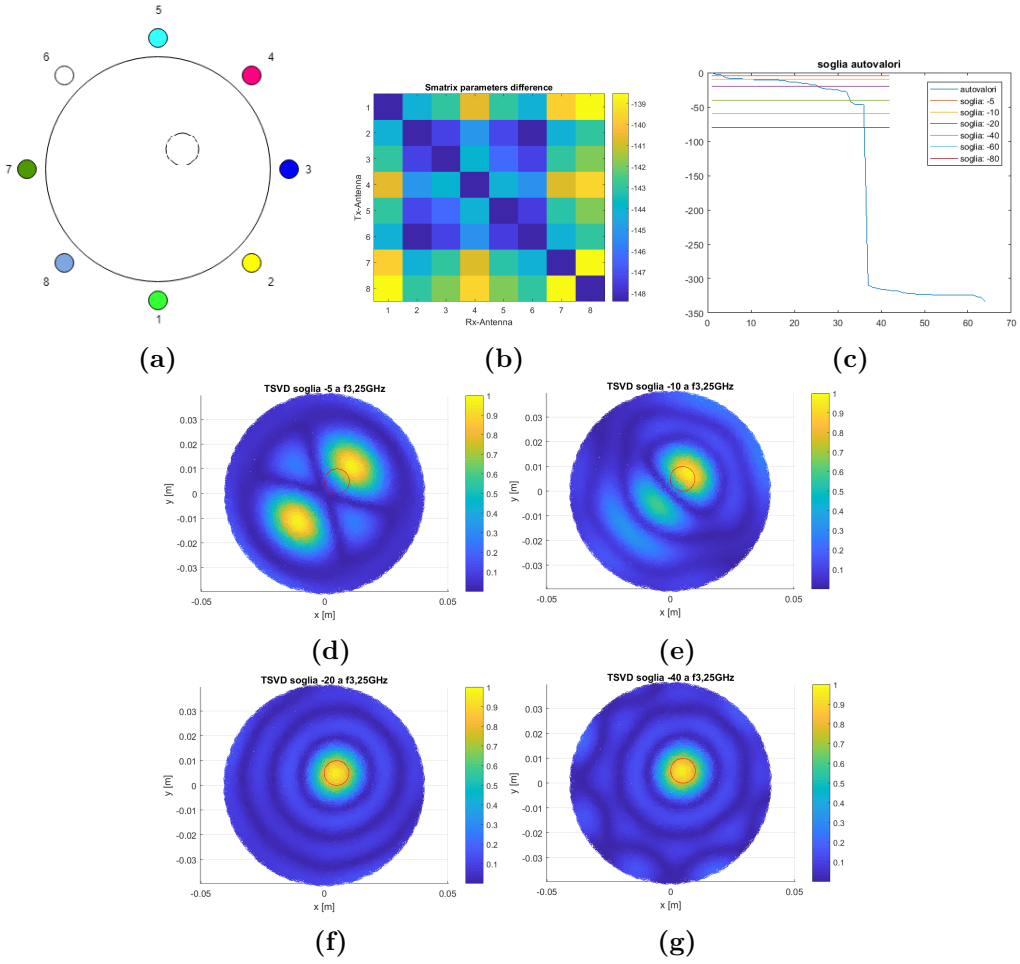

Figure 7.45: TSVD outputs

This situation is similar to the previous case, unless the smaller interaction matrix.

Results with inclusion radius: 0.0625cm

Considering the respective case with air composed sphere, which results are in figures (7.40), the system performances show a rapid decrease because the object dimensions are no more compatible with the expected resolution at this frequency giving as outputs noise components only with higher threshold values.

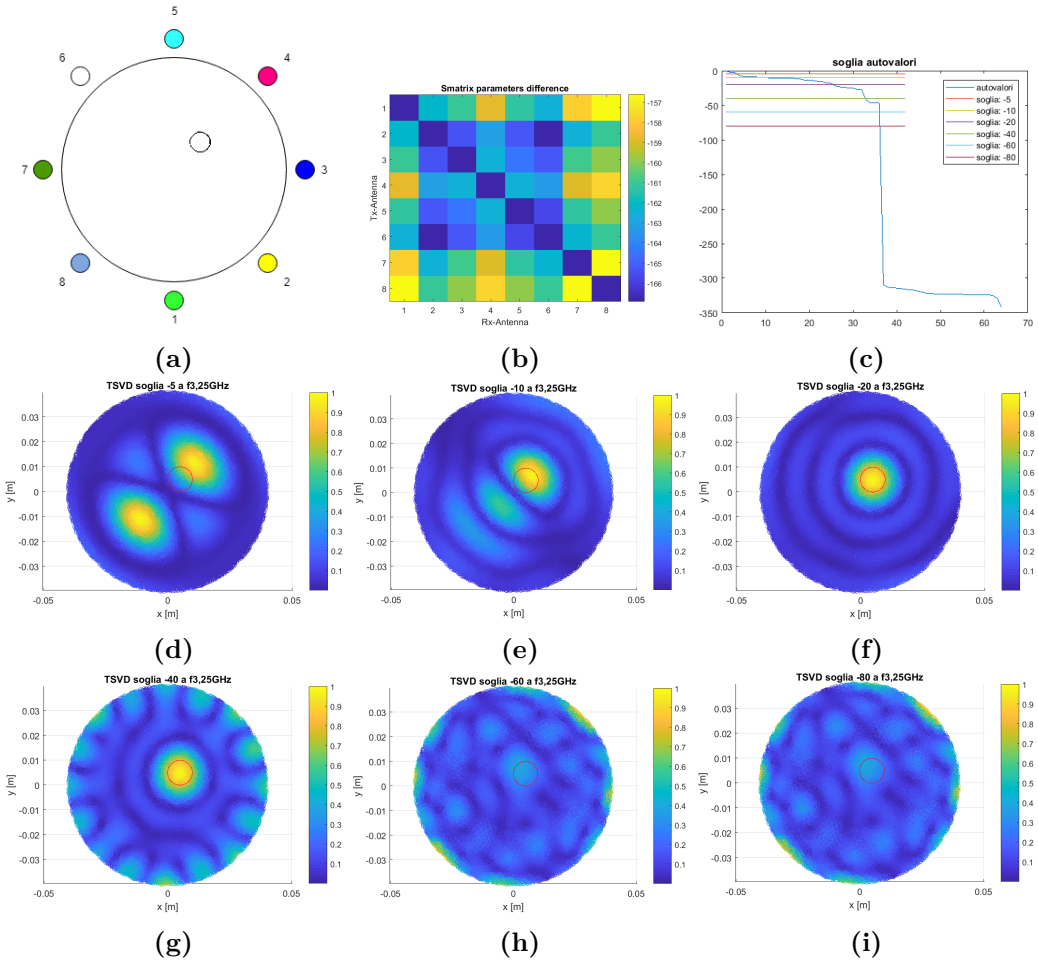

Figure 7.46: TSVD outputs

7.4 Model 3: adding the jar

In this section the jar is finally added to the model in order to study the performance variation of the system. As in figure (7.47), the hazelnut cream volume is enclosed by a 3 mm jar, that is made of glass or *GlassPet* plastic. The other model characteristics are unchanged. The dielectric properties of the used material for componing the jar are listed below: The jar introduction creates new interfaces between materials, that leads to

Glass	$\sigma = 0\ \epsilon_r' = 4.7$
Plastic - *GlassPet*	$\sigma = 0\ \epsilon_r' = 3.4$

additional reflections that mean additional noise. Moreover these new interfaces create a gradual transition from air to cream, probably making it less noisy too.
In this section are presented the simulation with a spherical inclusion, first made of air then

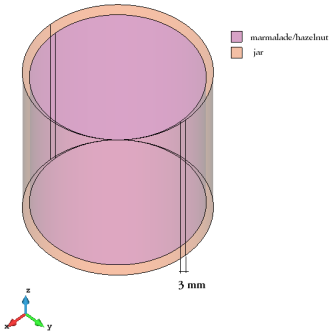

Figure 7.47: Three dimensional model with jar addition

plastic ($\epsilon'_r = 2.3$), with a radius equal to $5mm$ and $0.625mm$ to study the MWI behavior difference with the respective borderline cases.

7.4.1 Case: plastic jar (Glass-Pet) and air spherical inclusion

Results with inclusion radius: 0.5 cm and frequency: 2.75 GHz

General parameters

- Dielectric properties:
  $\sigma_{nut} = 0.027$
  $\epsilon_{real} = 3.285$
- Background volume: *air*
  $\sigma_{air} = 0$
  $\epsilon_{air} = 1$
- Antennae-distance jar: $4cm$
- Jar material: *Glass-Pet*
- Inclusion material: *air*
- Inclusion position: $x = 0.5cm$, $y = 0.5cm$, $z = 3.8cm$

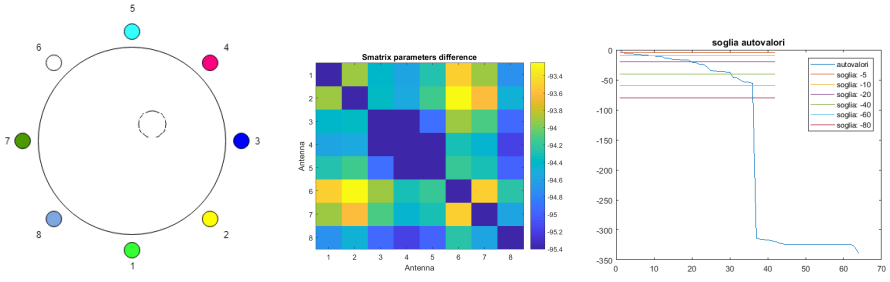

(a) **(b)** **(c)**

Figure 7.48

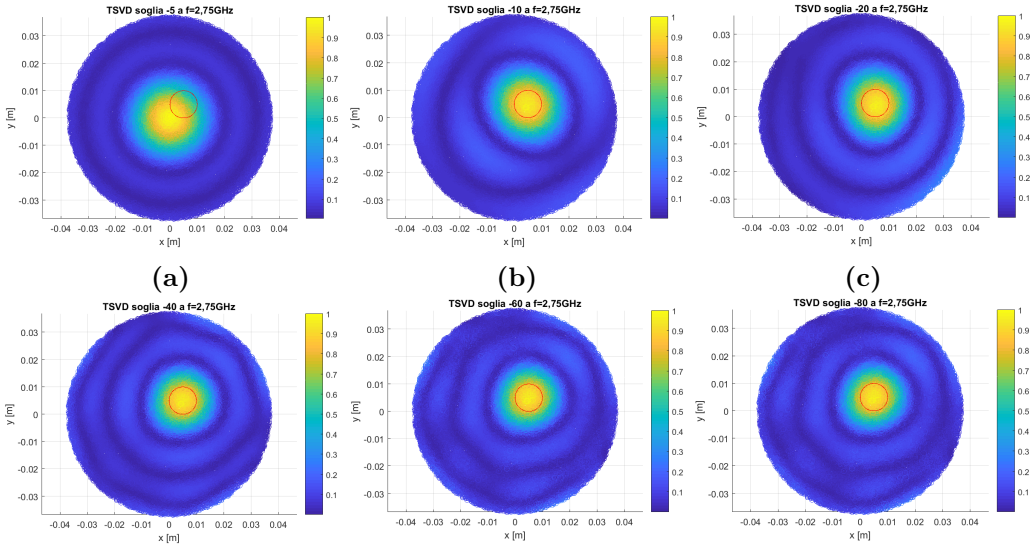

Figure 7.49: TSVD output

At this frequency and with this inclusion dimensions, the outputs don't have substantial difference respect to the case without jar of figure (fig.7.36).

Results with inclusion radius: 0.625 mm and frequency: 3.25 GHz

General parameters

- Dielectric properties:
  $\sigma_{nut} = 0.04$
  $\epsilon_{real} = 3.3$
- Background volume: *air*
  $\sigma_{air} = 0$
  $\epsilon_{air} = 1$
- Antennae-jar distance: $4cm$
- Jar material: *Glass-Pet*
- Inclusion material: *air*
- Inclusion position: $x = 0.5cm$, $y = 0.5cm$, $z = 3.8cm$

In this case also the detection is correct, but respect to its counterpart without the jar (fig.(7.40)), the noise is stronger influencing the detection.

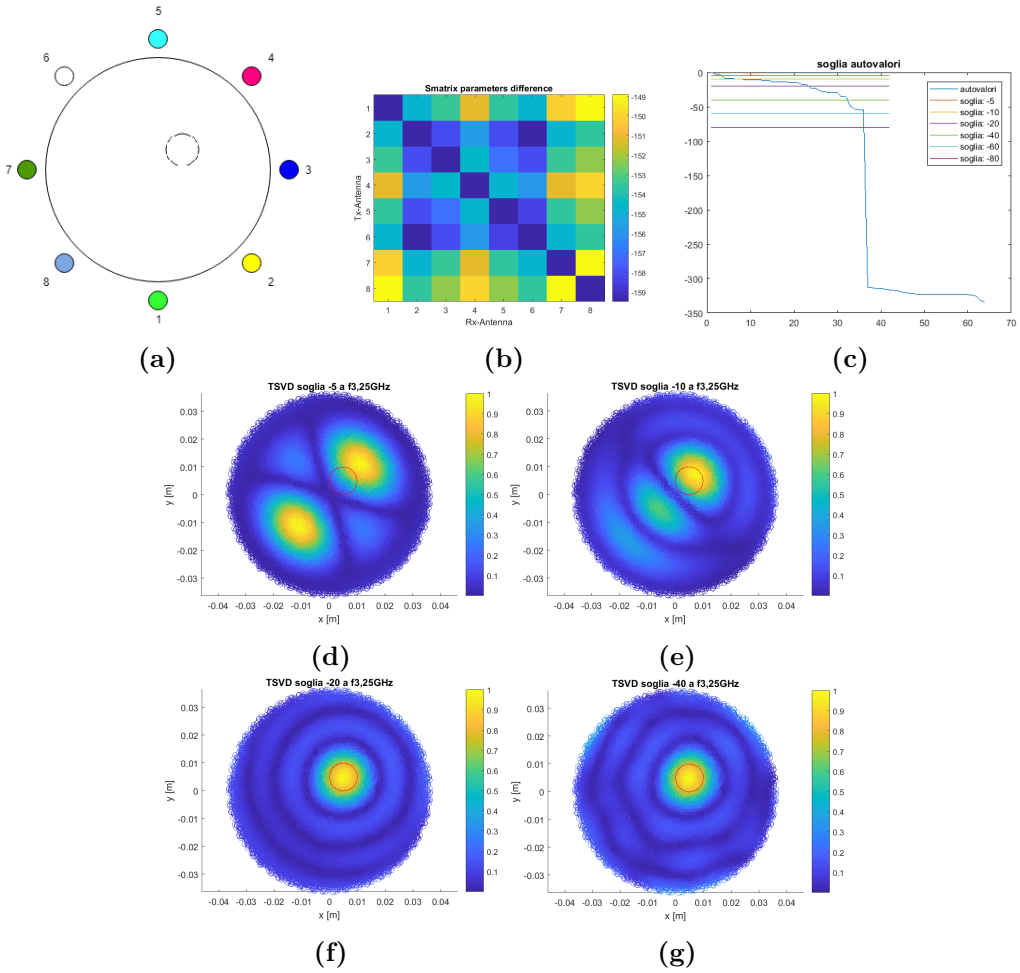

Figure 7.50: TSVD outputs

7.4.2 Case: plastic jar (Glass-Pet) and plastic spherical inclusion

In these simulations, because the electric permittivity of the intrusion is similar to the cream one it is less easier obtain a correct detection without increasing the frequency.

Results with inclusion radius: 0.5cm and frequency: 2.75GHz

General parameters

- Dielectric properties:
  $\sigma_{nut} = 0.027$
  $\epsilon_{real} = 3.285$
- Background volume0: *air*
  $\sigma_{air} = 0$
  $\epsilon_{air} = 1$

- Antennae-jar distance: $4cm$
- Jar material: *Glass-Pet*
- Inclusion material: *Plastic*
  $\sigma_{plastic-obj} = 0$
  $\epsilon_{plastic-obj} = 2.3$
- Inclusion position: $x = 0.5cm$, $y = 0.5cm$, $z = 3.8cm$

In these results the introduced jar seems to not influence the detection capability because they are similar to the case without jar shown in (fig.(7.42)).

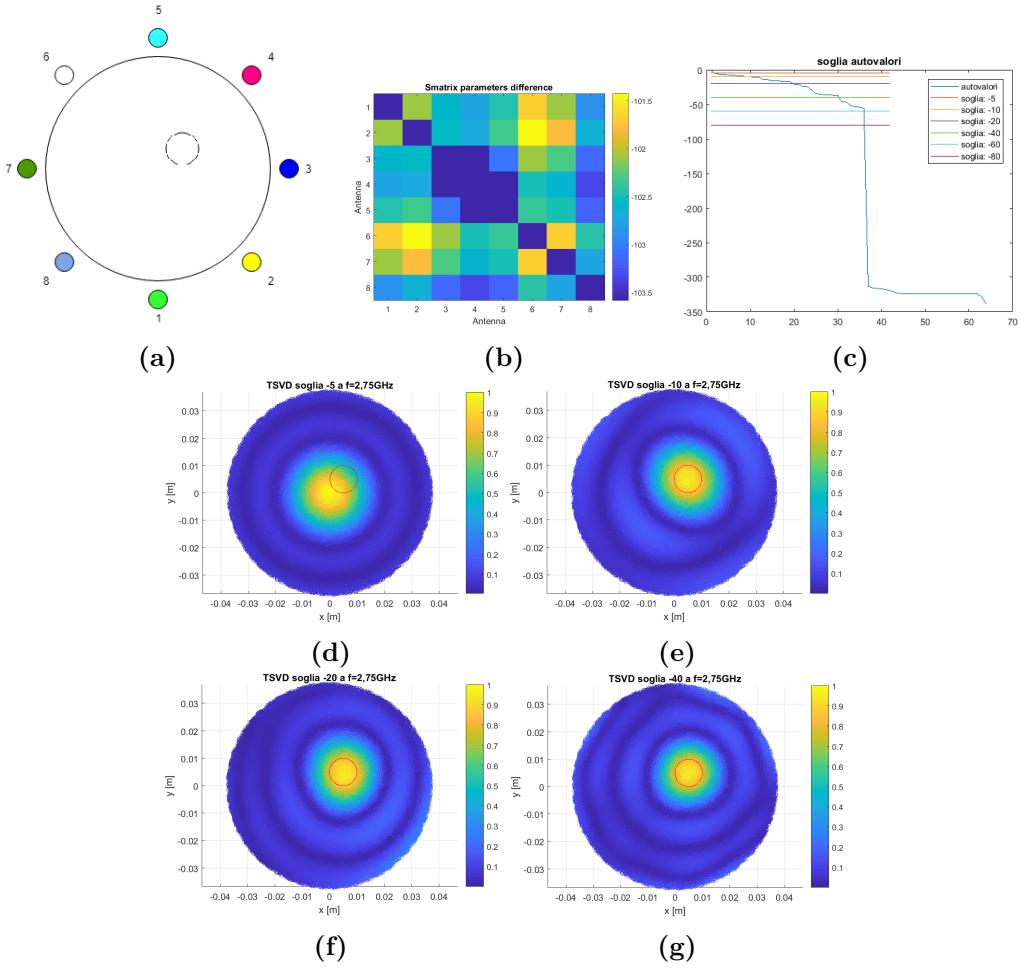

Figure 7.51: TSVD outputs

Results with inclusion radius: 0.625mm and frequency: 3.25GHz

General parameters

- Dielectric properties:
  $\sigma_{nut} = 0.04$
  $\epsilon_{real} = 3.3$
- Background volume: *air*
  $\sigma_{air} = 0$
  $\epsilon_{air} = 1$
- Antennae-jar distance: $4cm$
- Jar material: *Glass-Pet*
- Inclusion material: *Plastic*
  $\sigma_{plastic-obj} = 0$
  $\epsilon_{plastic-obj} = 2.3$
- Inclusion position: $x = 0.5cm$, $y = 0.5cm$, $z = 3.8cm$

Matrix interaction values decrease again, cause the similar dielectric properties of hazelnut cream and the plastic material of the sphere. In fact the detection is loosed in advance of its respective case where the object is fully made of air(fig.(7.50)).

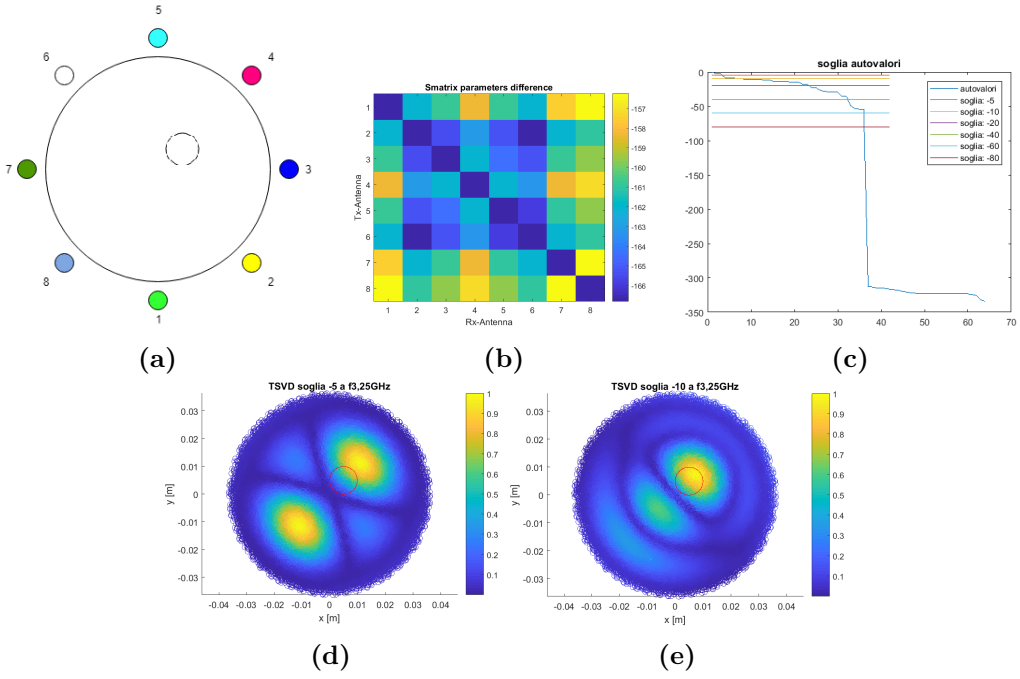

(a) **(b)** **(c)**

(d) **(e)**

Figure 7.52

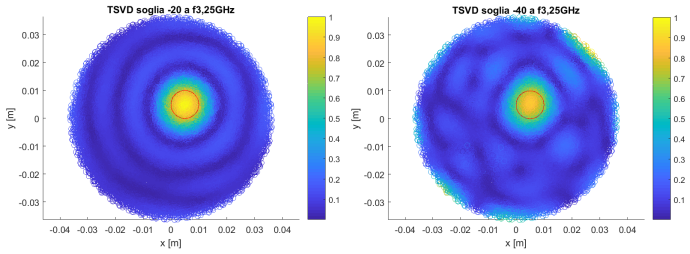

(f) (g)

Figure 7.52: TSVD outputs

7.4.3 Case: glass jar and air spherical inclusion

Results with inclusion radius: 0.5cm and frequency: 2.75GHz

General parameters

- Dielectric properties:
  $\sigma_{nut} = 0.027$
  $\epsilon_{real} = 3.285$
- Background volume: *air*
  $\sigma_{air} = 0$
  $\epsilon_{air} = 1$
- Antennae-jar distance: $4cm$
- Jar material: *Glass*
- Inclusion material: *air*
- Inclusion position: $x = 0.5cm$, $y = 0.5cm$, $z = 3.8cm$

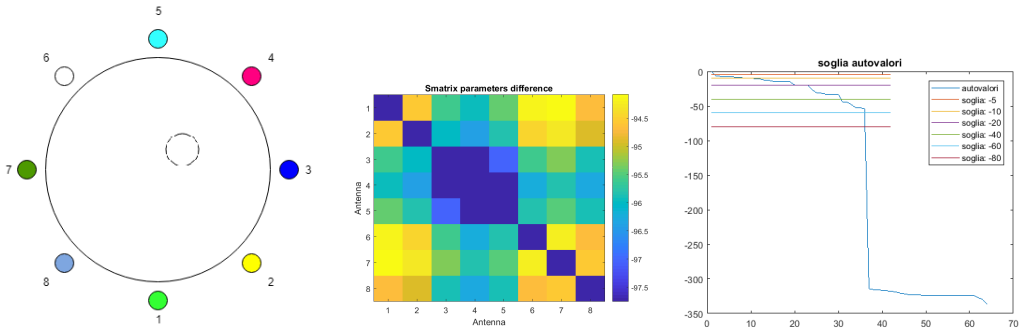

(a) (b) (c)

Figure 7.53

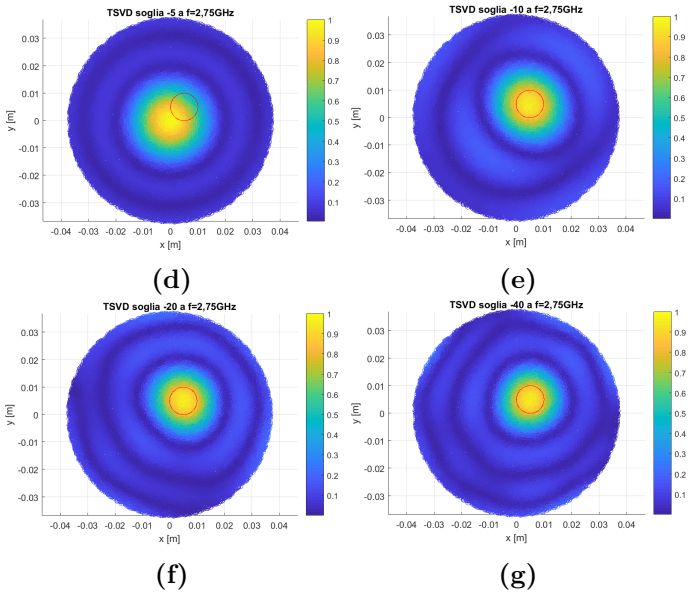

Figure 7.53: TSVD outputs

The jar material change doesn't seem to have influenced the detection capability of the system, that is able to find the intrusion independently from the information quantity given to the TSVD algorithm.

Results with inclusion radius: 0.625mm and frequency: 3.25GHz

General parameters

- Dielectric properties:
  $\sigma_{nut} = 0.04$
  $\epsilon_{real} = 3.3$
- Background volume: *air*
  $\sigma_{air} = 0$
  $\epsilon_{air} = 1$
- Antennae-jar distance: $4cm$
- Jar material: *Glass*
- Inclusion material: *air*
- Inclusion position: $x = 0.5cm$, $y = 0.5cm$, $z = 3.8cm$

As expected the object dimensions start to be too small to be detected at 3.25 GHz. This is shown by the fact the detection is confused with the background noise.

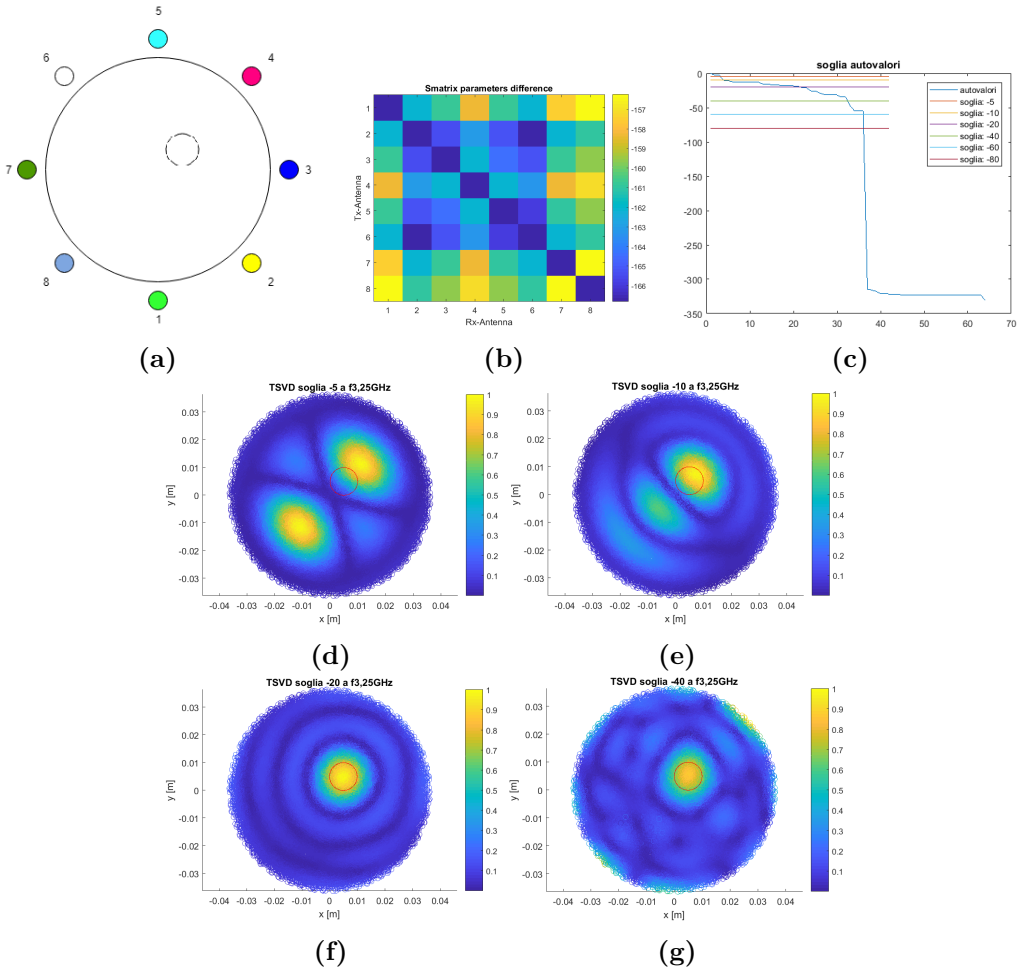

Figure 7.54: TSVD outputs

7.4.4 Case: glass jar and plastic spherical inclusion

Results with inclusion radius: 0.5cm and frequency: 2.75GHz

General parameters

- Dielectric properties:
  $\sigma_{nut} = 0.027$
  $\epsilon_{real} = 3.285$
- Background volume: *air*
  $\sigma_{air} = 0$
  $\epsilon_{air} = 1$
- Antennae-jar distance: $4cm$
- Jar material: *Glass*

- Inclusion material: *Plastic*
- Inclusion position: $x = 0.5cm$, $y = 0.5cm$, $z = 3.8cm$

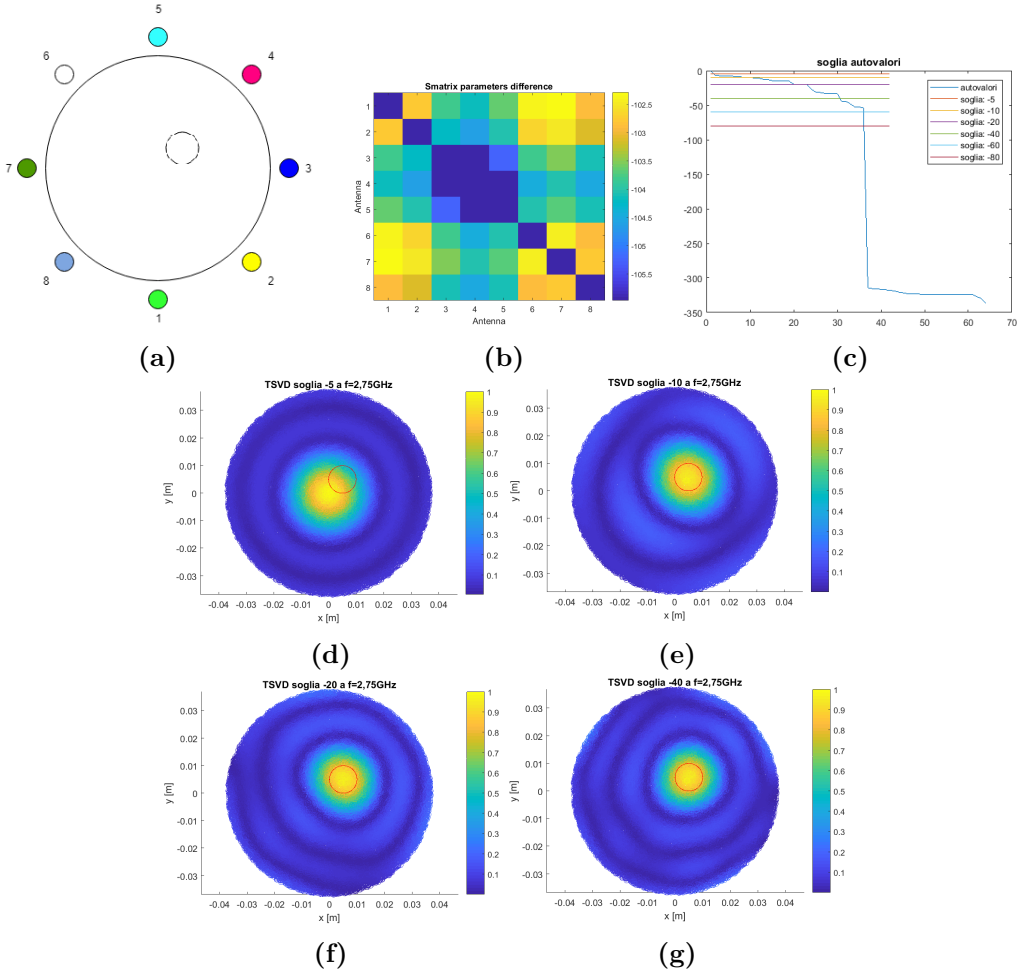

Figure 7.55: TSVD outputs

As observed in figure (7.55), since the sphere dimensions are compatible with the expected resolution for this frequency, the detection is correct. Anyway the need to increase the frequency is in the lower value of the interaction matrix.

Results with inclusion radius: 0.625mm and frequency: 3.25GHz

General parameters

- Dielectric properties:
  $\sigma_{nut} = 0.04$
  $\epsilon_{real} = 3.3$

- Background volume: *air*
  $\sigma_{air} = 0$
  $\epsilon_{air} = 1$
- Antennae-jar distance: $4cm$
- Jar material: *Glass*
- Inclusion material: *Plastic*
  $\sigma_{plastic-obj} = 0$
  $\epsilon_{plastic-obj} = 2.3$
- Inclusion position: $x = 0.5cm$, $y = 0.5cm$, $z = 3.8cm$

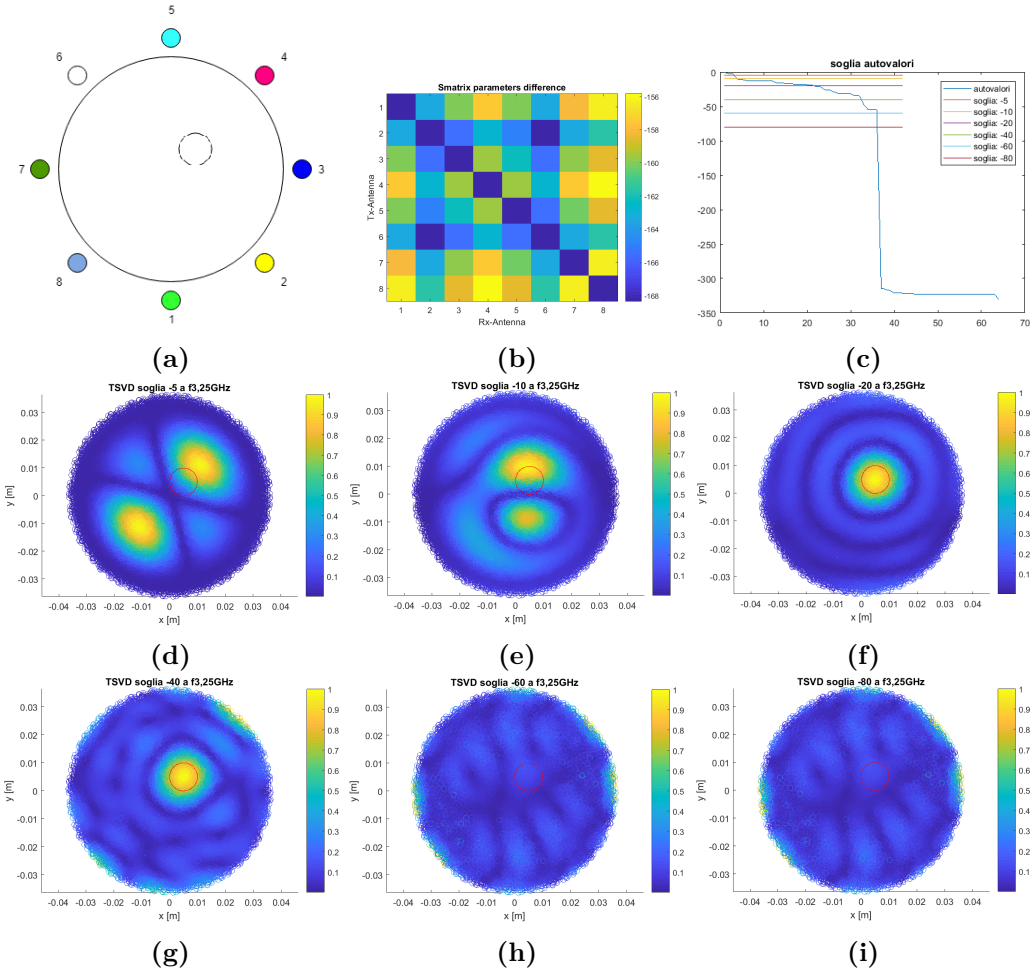

Figure 7.56: TSVD outputs

As in the previous cases, when the sphere is made of plastic material, that is characterized by a similar cream permittivity, the detection is harder because the less contrast. In fact at higher threshold values the noise informations became stronger.

7.5 Simulations results conclusions

After showing these results, it is stated that the MWI system has the correct behavior, since the antenna is used in a not ideal range for its resonance, frequencies range where its S_{11} are higher. Anyway the simulated situations were ideal, so to get correct detection in the laboratory test it is need increase the frequency in order to avoid the high noise dues to the environment, non ideal components and instrumentations. Moreover being the TSVD algorithm a differential procedure it is quite robust against input data errors since they influence all the inputs in the same way. In addition to that there are also some calibration methods that can be used to decrease noise influence, as the one presented in section 6.2.

Chapter 8

MWI sperimental tests

This chapter sees the description of the microwave imaging system prototype and sperimental testing at *Antenna and Electromagnetic Compatibility Laboratory (LACE)*, a substructure of the Department of Electronics and Telecommunications (DET) sited at Politecnico di Torino.
Tests presented cover the presented simulated situations and case to study the false-positive phenomena, that is one of the main problems in food imaging, because it can leads to a looses income in case of wrong detection.

8.1 Measure system

The entire measurement system, shown in figure(8.1a), is composed by the main computer,that using a MATLAB script commanding switch matrix(figure (8.1b)), which defines all the path between the antennae, through the control card Keysight L4445(fig.(8.2a)). It consists of two SP4T, eight SP6T and twenty-four SPDP electromechanical coaxial switches. The switches are connected with semi-rigid coaxial cables in order to realize a 2 by 24 switching matrix. Input and output of this matrix are connected to the VNA in order to measure the scattering parameters of each monopole. The Network vector analyzer is a Keysight PNA N5227A, shown in picture (8.2b).

(a) Microwave imaging system prototype **(b)** Switching matrix

Figure 8.1

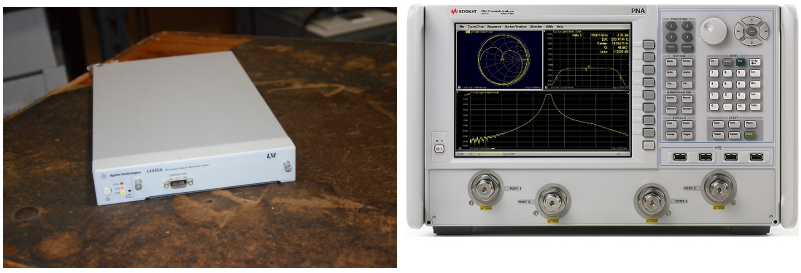

(a) Keysight L4445 **(b)** VNA

Figure 8.2

The main features of the switch matrix (figure (8.1b)) are the Keysight switches characterized by high isolation and low losses in order to not influence the acquired scattered data from the antennae. Their are divided in

- 8 L7106A Switch, SP6T, DC-4 GHz, terminated (L-series)
- 8 L7106A-024 24 vdc
- 2 L7104A Switch, SP4T, DC-4 GHz, terminated (L-series)
- 2 L7104A-024 24 vdc
- 24 8762A Coaxial SPDT switch, DC-4 GHz, 50 ohm

8.1.1 Inclusion collection

During the tests 3 type of foreign object detection are proved, from a lower to higher realistic inclusions. The first used is a plastic cylindric full of air, shown in figure(8.3a), that is also the case more similar to the firsts simulations. Then tests are moved towards object with smaller dimensions to challenge the system. The inclusion characteristics are:

- Cylinder type (fig.(8.3a))

  height: 6 cm

  diameter: 1 cm

- Plastic red cup (fig.(8.3b))

  0.6 cm × 1 cm × 1 cm

- Plastic sample with triangular shape (fig.(8.3c))

  1.3 cm × 1.2 cm × 0.15 cm

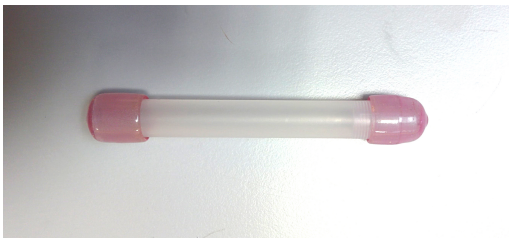

(a) First considered inclusion: a full air plastic cylinder

(b) Second considered inclusion: plastic cap

(c) First considered inclusion: plastic sample

Figure 8.3: Inclusions considered

8.2 Three dimensional model used to calculate the EM fields inside the target

The TSVD algorithm requires as input the simulated field inside the food jar to solve the imaging inversion problem. This field is obtained by the FEM solver applied on a similar 3D cad reproducing the situation in test.

8.2.1 Narrow band monopole testing model

This model is been used to simulate field in case of narrow band antennae at low frequency, as reported in the figure (8.4a). The chosen number of antenna in this case is 12 because the system holder has the possibility and the space to host them without any problem, as shown in fig.(8.4c). This model is used in case of marmalade and hazelnut cream studies. The characteristics of the prototype in this case are:

Antennae-jar distance: 2.5 cm

- Marmalade jar

  Jar radius: 3.5 cm

  Jar height: 8 cm

  Jar material: Glass

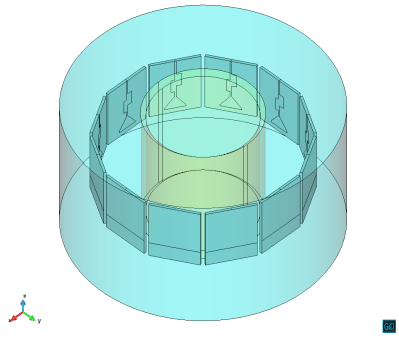

(a) 3D cad of MWI laboratory model in case of marmalade jar

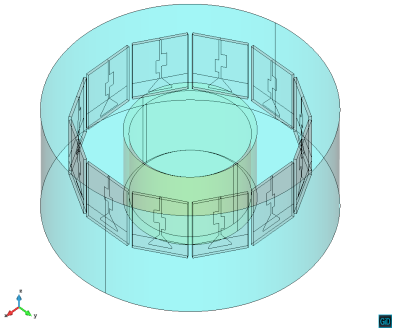

(b) 3D cad of MWI laboratory model in case of hazelnut cream jar

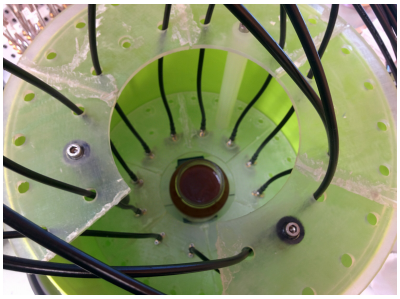

(c) 12 Antennae holder

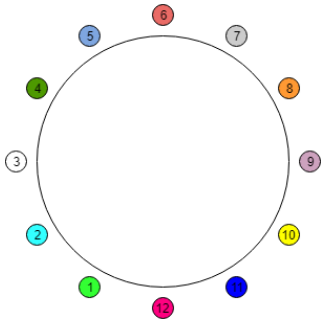

(d) Reference for 12 Antennae position

Figure 8.4

- Hazelnut cream volume

  Jar radius: 3.5 cm

  Jar height: 5 cm

  Jar material: Glass-pet plastic

- Antennae number: 12

The low frequency simulations are carried out for the following values, taking as reference the measure S_{11} parameters reported in figure (4.15). The expected penetration depth at the higher frequency is 1.15 cm with a resolution of 0.55.

Frequency	S_{11} $[dB]$
$2.75GHz$	-6.862
$3.25GHz$	-3.254
$6.25GHz$	-22
$6.75GHz$	-40.1
$8.00GHz$	-9.7

8.2.2 Ultra wide band monopole testing model

Here is showed the model (figure 8.5a) used with the ultra high band monopoles to calculate the field inside the jar for higher frequencies values. As presented in fig.(8.5b) in these

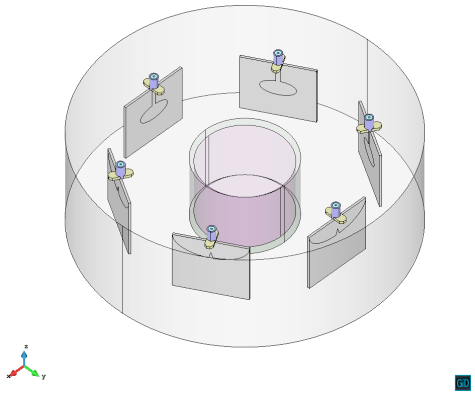

(a) 3D cad of MWI laboratory model in case of marmalade jar

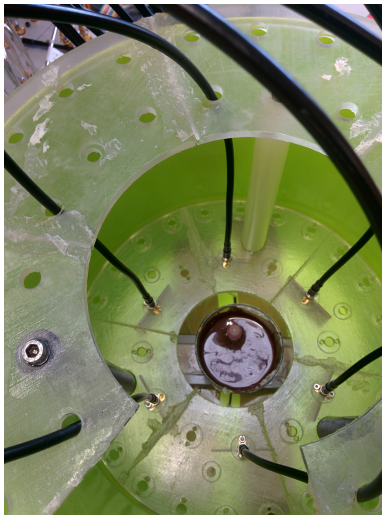

(b) Antennae holder

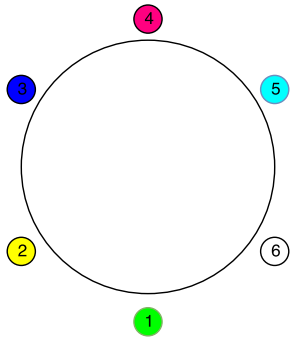

(c) 6 antennae positioning example

Figure 8.5

laboratory tests 6 antennae can be hosted by the holder because their larger dimensions. In this case some of the measured frequencies, referencing to the graphic in (4.33) are in table 8.1. The characteristics of the prototype in this case are:

Frequency	S_{11} $[dB]$
$7.75GHz$	-20.1
$9.50GHz$	-25
$10GHz$	-20
$11GHz$	-19

Table 8.1

- Antennae-jar distance: 4 cm
- Antennae number: 6

Moreover for these measures the data inputs are calibrated using the procedure described in section 6.2 and a multi frequency reconstruction by TSVD are performed (6.3) to obtain cleaner output detections.

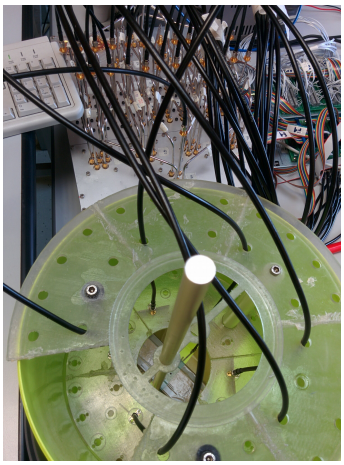

Figure 8.6: Calibration setup

8.3 Tests results

During tests same reference coordinates systems are considered and the to reconstruct the detection is used the field slide in front of the radiated region of the antennae. It is important underline that a 3D reconstruction of the entire target is also possible.

8.3.1 Narrow band monopoles mounted prototype measurements

In this situation, the detection is simpler because the antennae number is 12 and with it the system is surely able to have a good data acquisitions. Here are reported few results obtained in case of jam target because, as already seen in the respective simulation, it doesn't offer good possibility to obtain a correct detection, in contrast with the hazelnut cream.
As first approach the correctness of the system measures can be studied considering the

transmission path plot between some antennae, as example reported in figures(8.7). The transmission path is the wave traveled route between two different antennae. If there is a difference between the case of inclusion and its absence, the system should "see" the object.

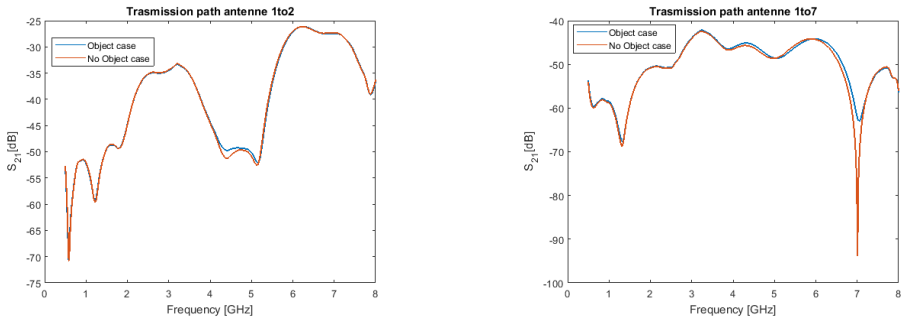

(a) Transmission path between near antennae

(b) Transmission path between far antennae

Figure 8.7: Transmission path example for cylindrical inclusion

8.3.2 Orange marmalade laboratory test results

With this setup(figure(8.4a)) the marmalade is investigated at low frequency only and for one case, because, as already explained its water content doesn't make the field able to penetrate the jam at higher frequencies.

Measure results at 2.75 GHz with cylindrical inclusion

Here a cylindrical inclusion of 1 cm diameter is searched inside the marmalade jar. The results, listed in figures (8.8), don't give any detection as expected and shown by the simulations.

These results state that it is useless increase the frequency with this type of material.

8.3.3 Hazelnut cream laboratory test results at 2.75 GHz

In this section the obtained results, exploring the cream, are presented varying the frequency values. As expected the results are encouraging. Increasing the frequency the system increases the detection quality thanks to the expected resolution values that are more similar to the inclusion dimensions, since the monopole is quite adapted at the working frequency.

Measure results with cylindrical inclusion

System setup is shown in figure (8.9) and the obtained results are in fig.(8.10)

In this first presented situation the system has a correct detection, but in a wrong position. This might be due to the position's coordinate of the object that can be at a multiple of $\lambda/4$ for this frequency, provoking the the wrong multiple position detection.

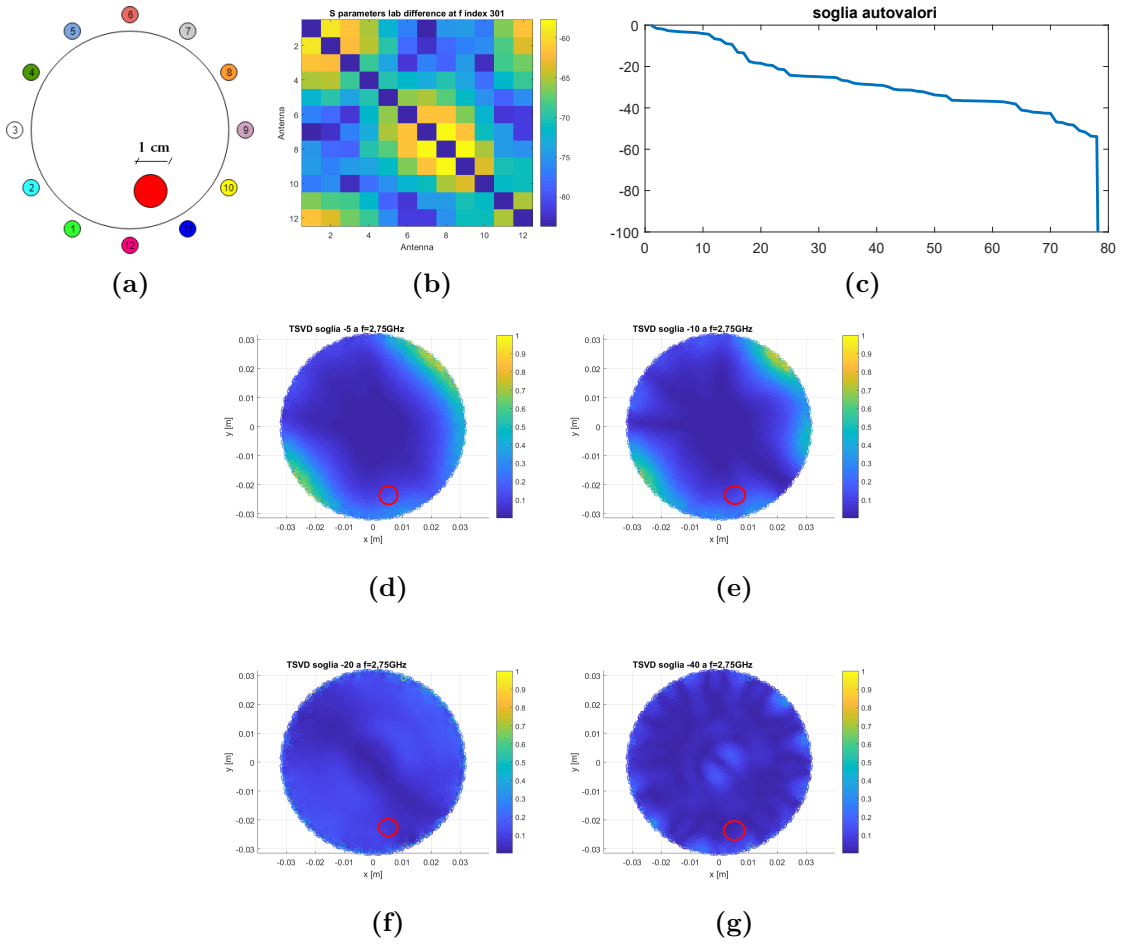

(a) (b) (c)

(d) (e)

(f) (g)

Figure 8.8: Measure TSVD outputs

Measure results with cylindrical inclusion in a different position

The inclusion position is moved in front the antenna number 3 as reported in figure (8.11a). The system in this case, thanks to the inclusion shift, gives good detection around the data threshold of -20 as shown in fig. (8.11f).

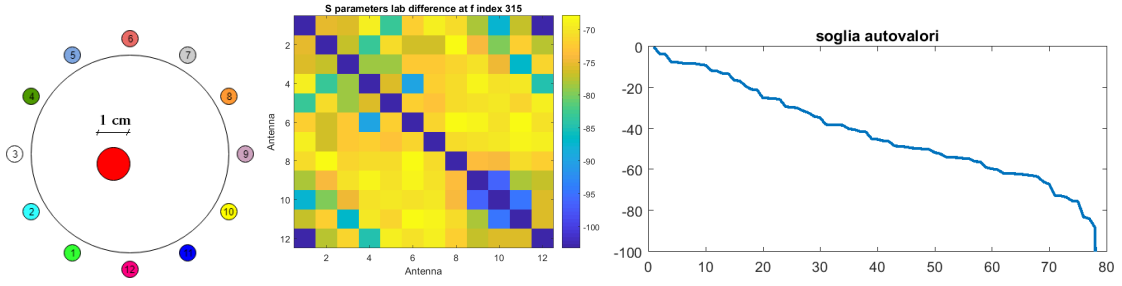

(a) (b) (c)

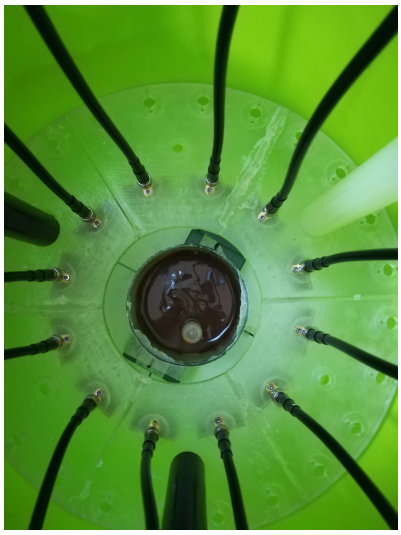

Figure 8.9: Jar positioning with the cylindrical inclusion

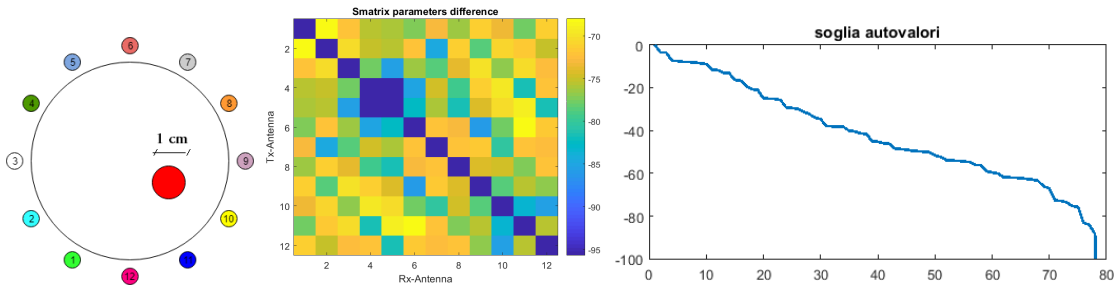

(a) **(b)** **(c)**

Measure results with plastic red cup inclusion

The detection of the small cup, photographed in fig.(8.3b), starts to be correct at -20 threshold for the input data of TSVD. As expected the detection at low frequency is quite hard inside the cream because its dispersive behavior at these values.

Measure results with plastic sample inclusion

This section contains the smaller inclusion between the considered ones, resulting in hardest detection to perform. Anyway it is also correctly detected as in the previous cases, but not independently from the data input quantities.

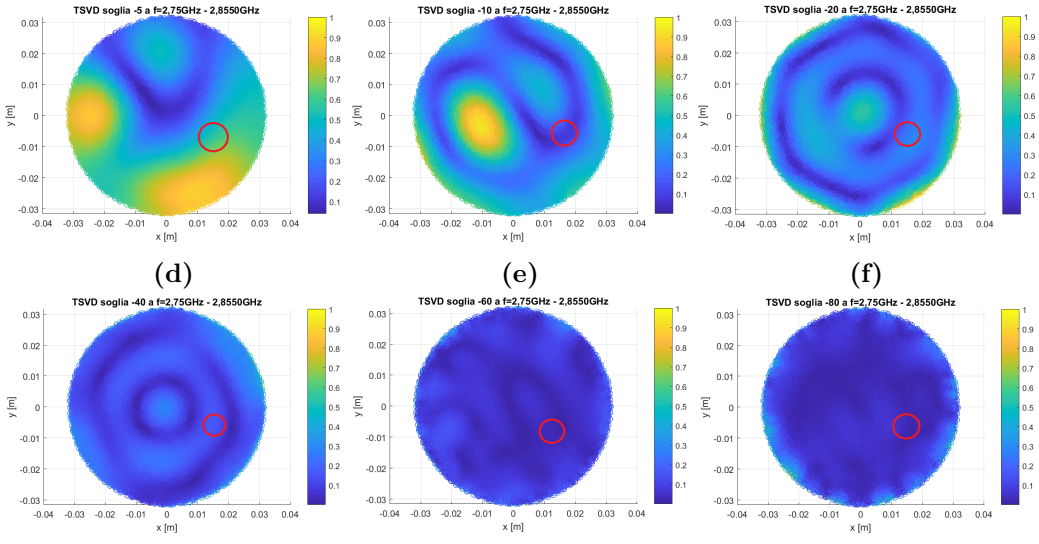

Figure 8.10: Measure TSVD outputs

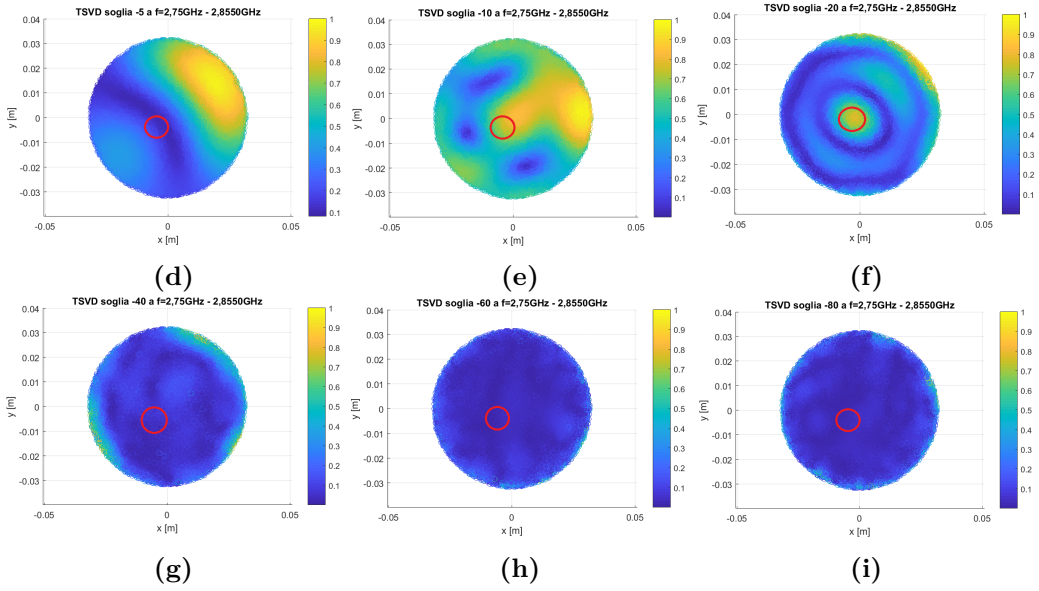

Figure 8.11: Measure TSVD outputs

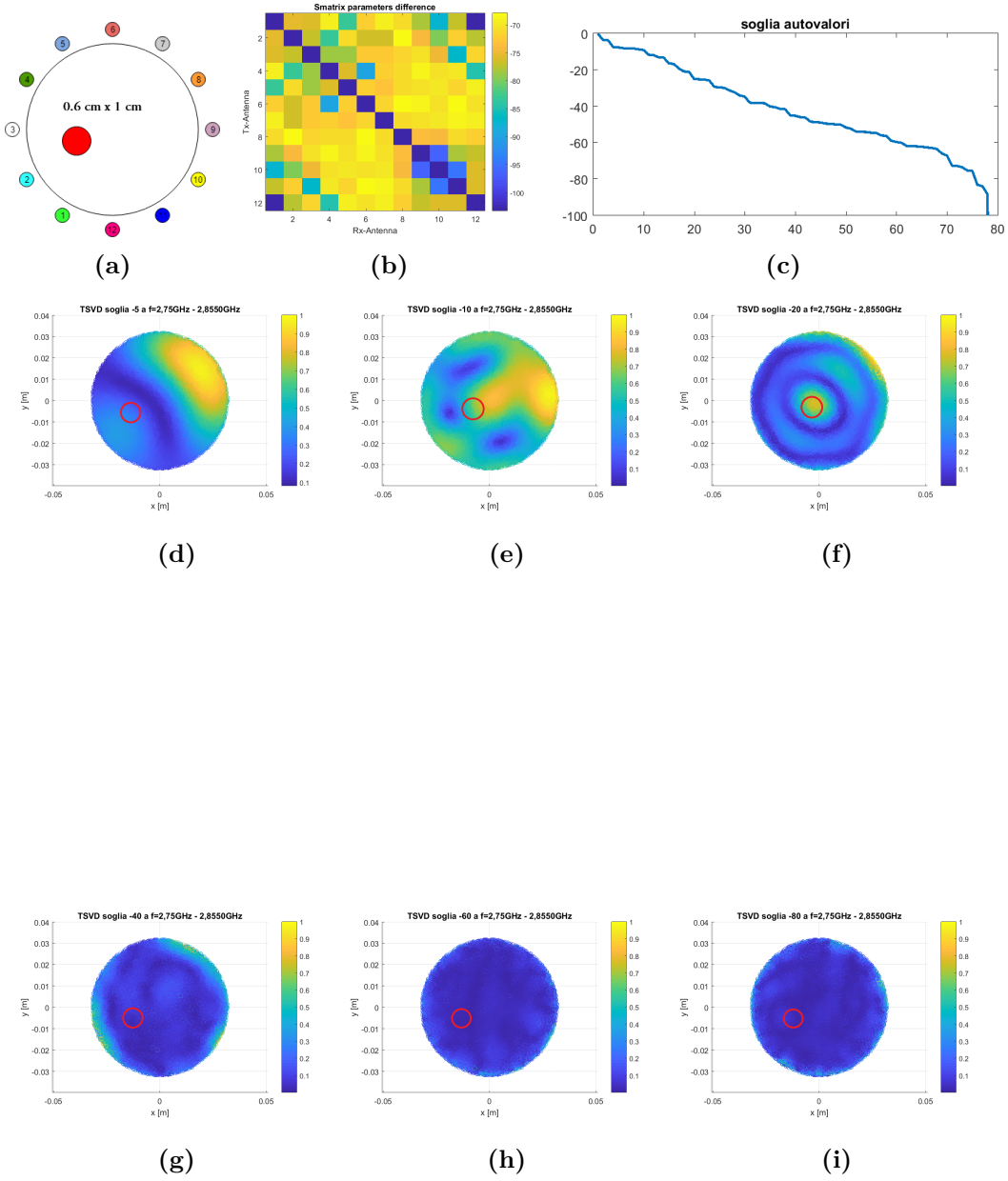

Figure 8.12: Measure TSVD outputs

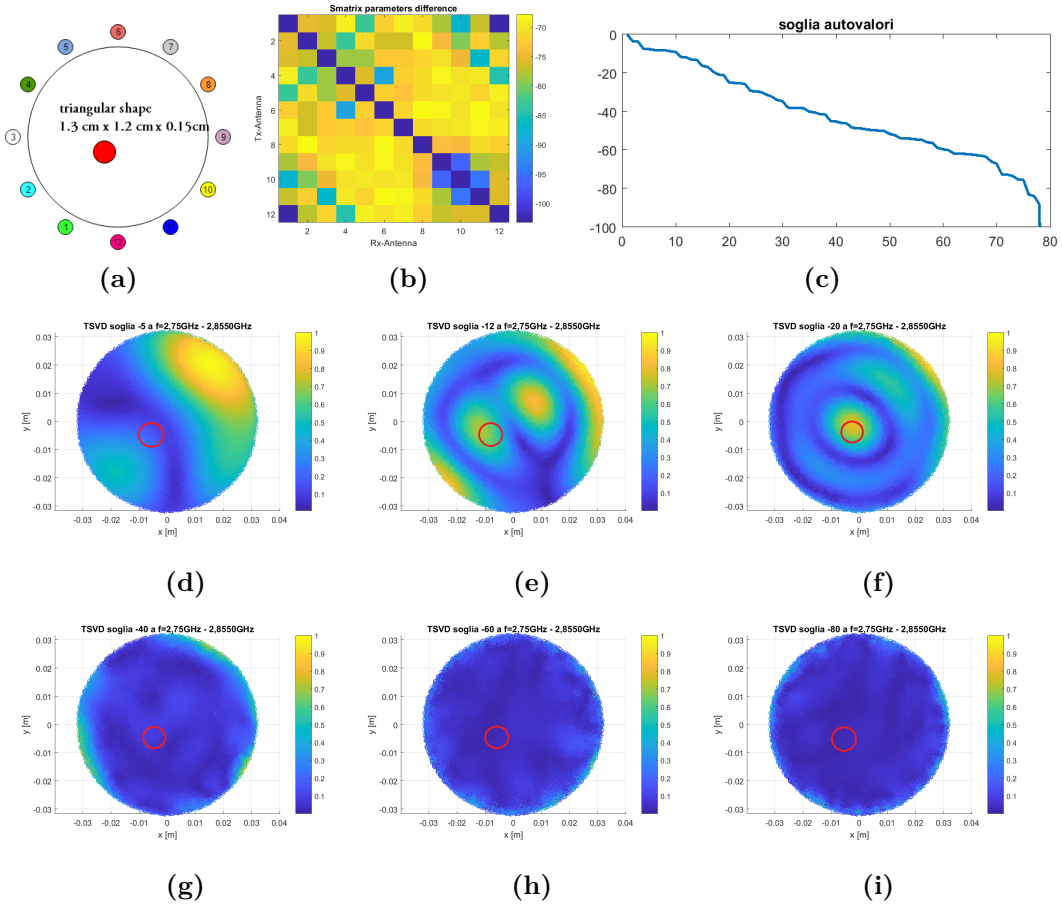

Figure 8.13: Measure TSVD outputs

8.3.4 Hazelnut cream laboratory test results at 3.25 GHz

At this frequency, the antennae are much less adapted, showing a S_{11} parameter equal to ≈ -3.254 dB. So worst results are expected.

Measure results with cylindrical inclusion

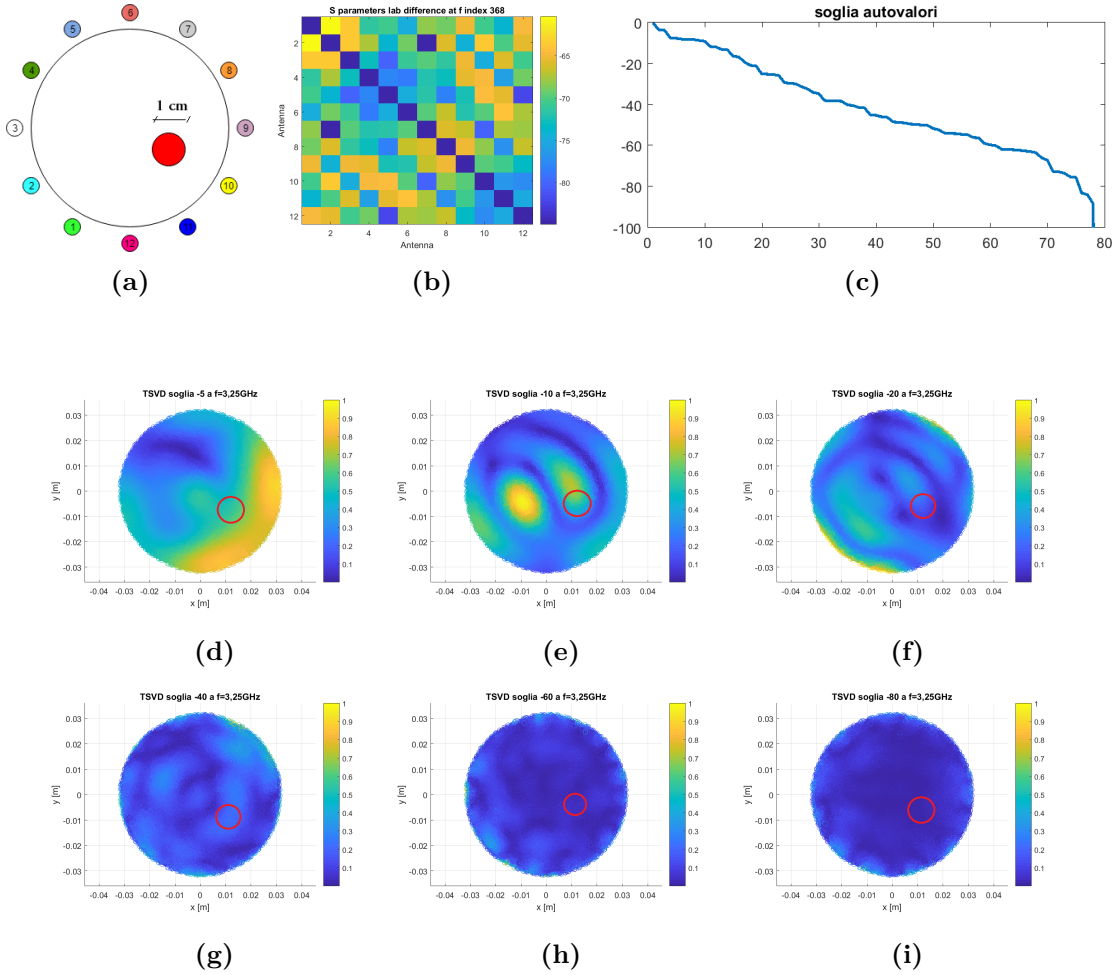

(a) (b) (c)

(d) (e) (f)

(g) (h) (i)

Figure 8.14: Measure TSVD outputs

Measure results with cylindrical inclusion in a different position

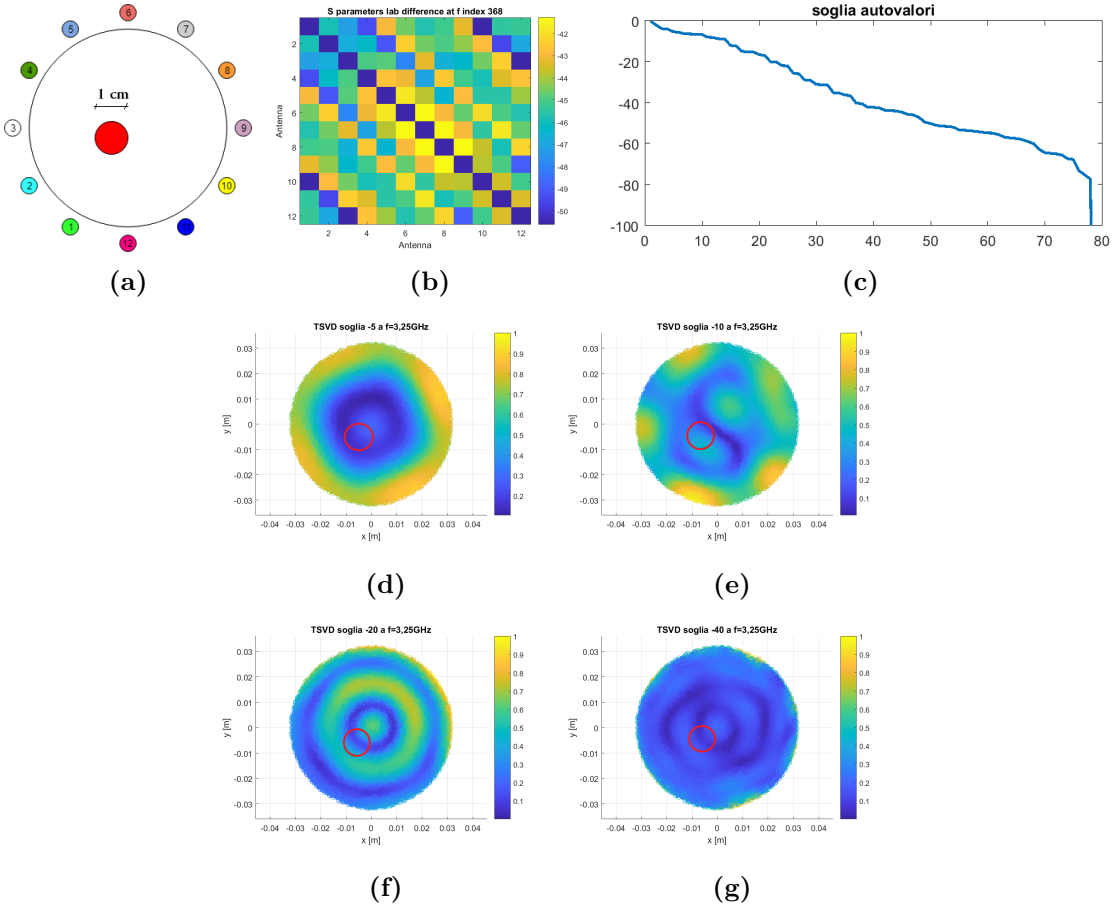

(a) (b) (c)

(d) (e)

(f) (g)

Figure 8.15: Measure TSVD outputs

Measure results with plastic red cup inclusion

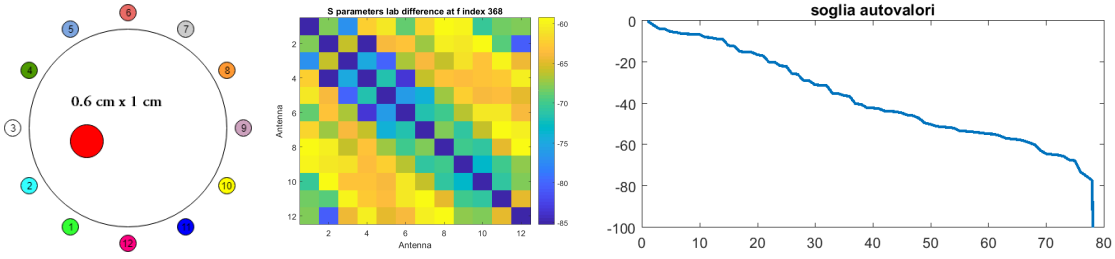

(a) (b) (c)

Figure 8.16

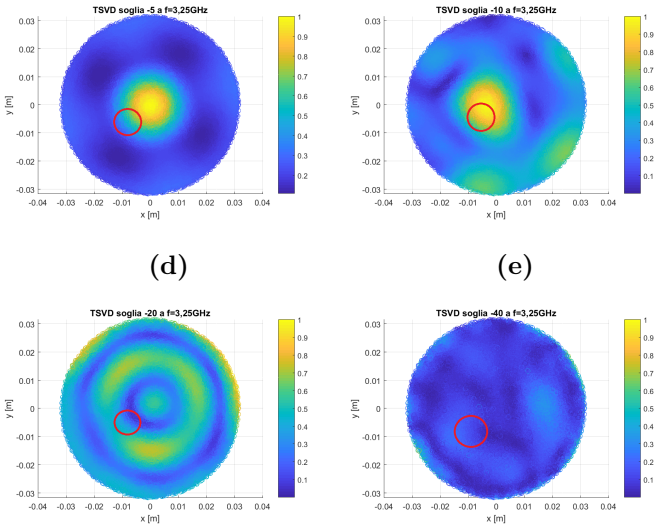

(d) (e)

(f) (g)

Figure 8.16: Measure TSVD outputs

Measure results with plastic sample inclusion

Even though the antenna adaptation is so low the detection seems correct.

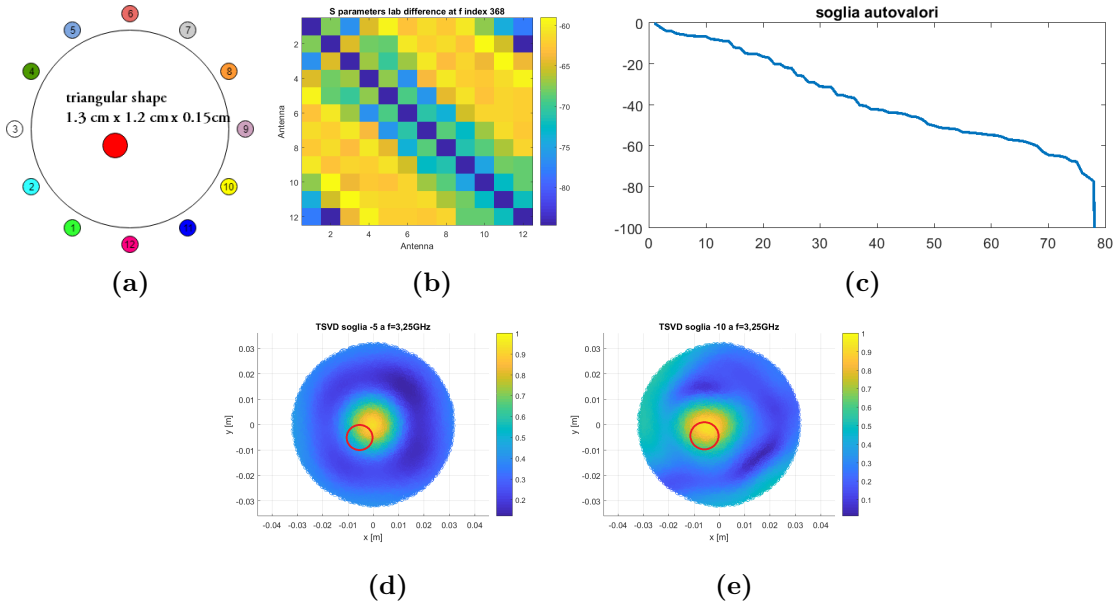

(a) (b) (c)

(d) (e)

Figure 8.17

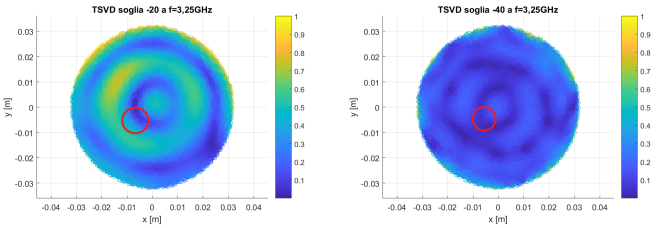

(f) (g)

Figure 8.17: Measure TSVD outputs

8.3.5 Hazelnut cream laboratory test results at 6.25 GHz

At this frequency, this monopole type is characterized by S_{11} equal to -22 dB. Here the detection shows good result, stating the importance to have a good adaptation at the working frequency. In this case the detection starts to be stable, because the detection is the same at more threshold values.

Measure results with cylindrical inclusion

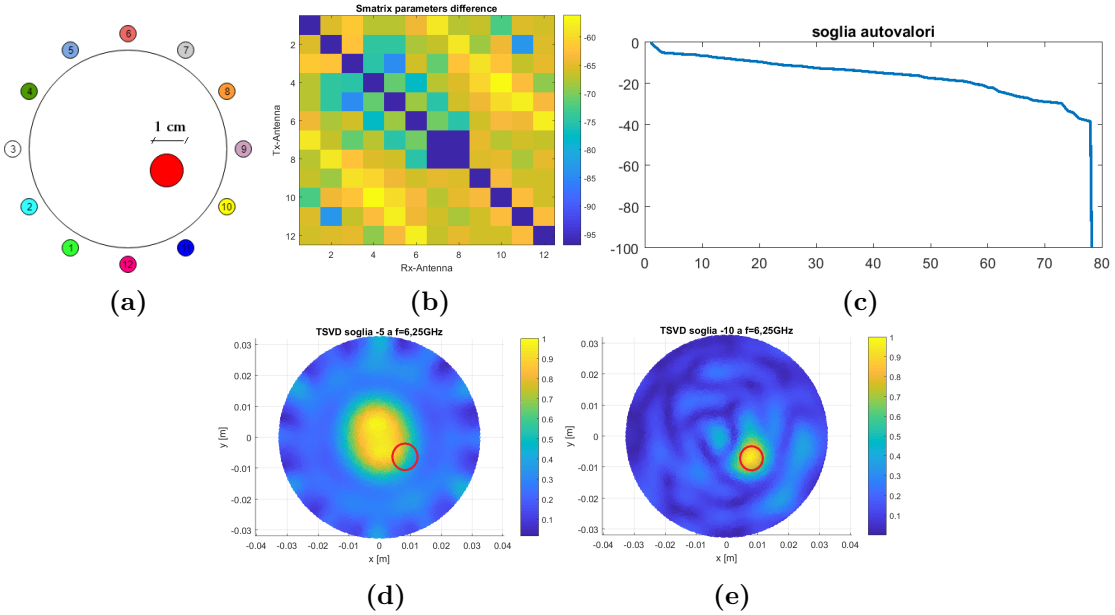

(a) (b) (c)

(d) (e)

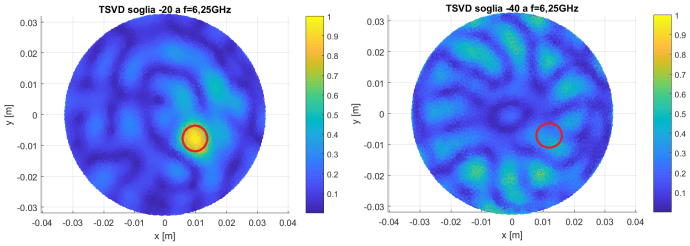

(f) (g)

Figure 8.18: Measured TSVD test

Measure results with cylindrical inclusion in a different position

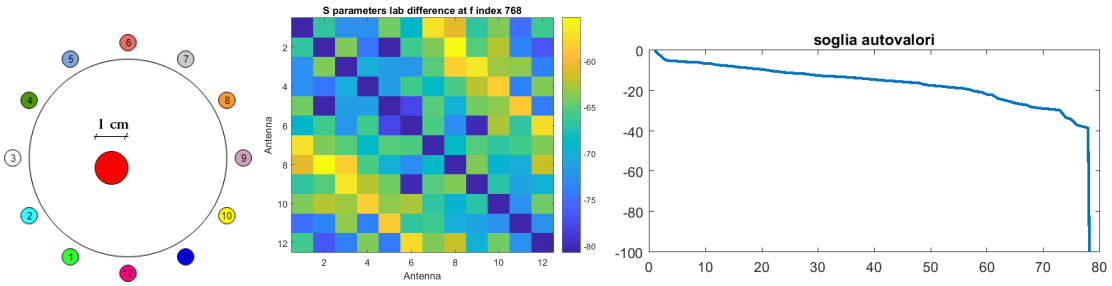

(a) (b) (c)

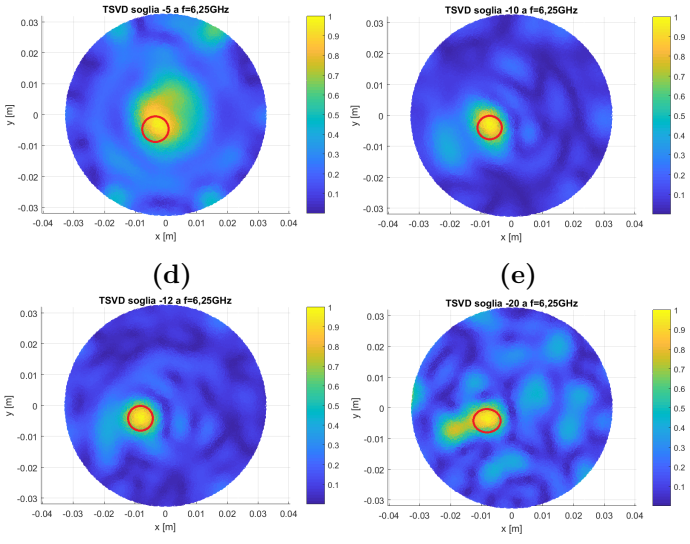

(d) (e)

(f) (g)

Figure 8.19: Measured TSVD test

Measure results with plastic red cup inclusion

Although the acceptable S_{11}, now the dimensions the inclusion (shown in figure (8.3b)), start to be to much smaller of the expected resolution. This is probably why the object position isn't correct: the input informations of the detection algorithm are not enough to correctly locate the foreign corp.

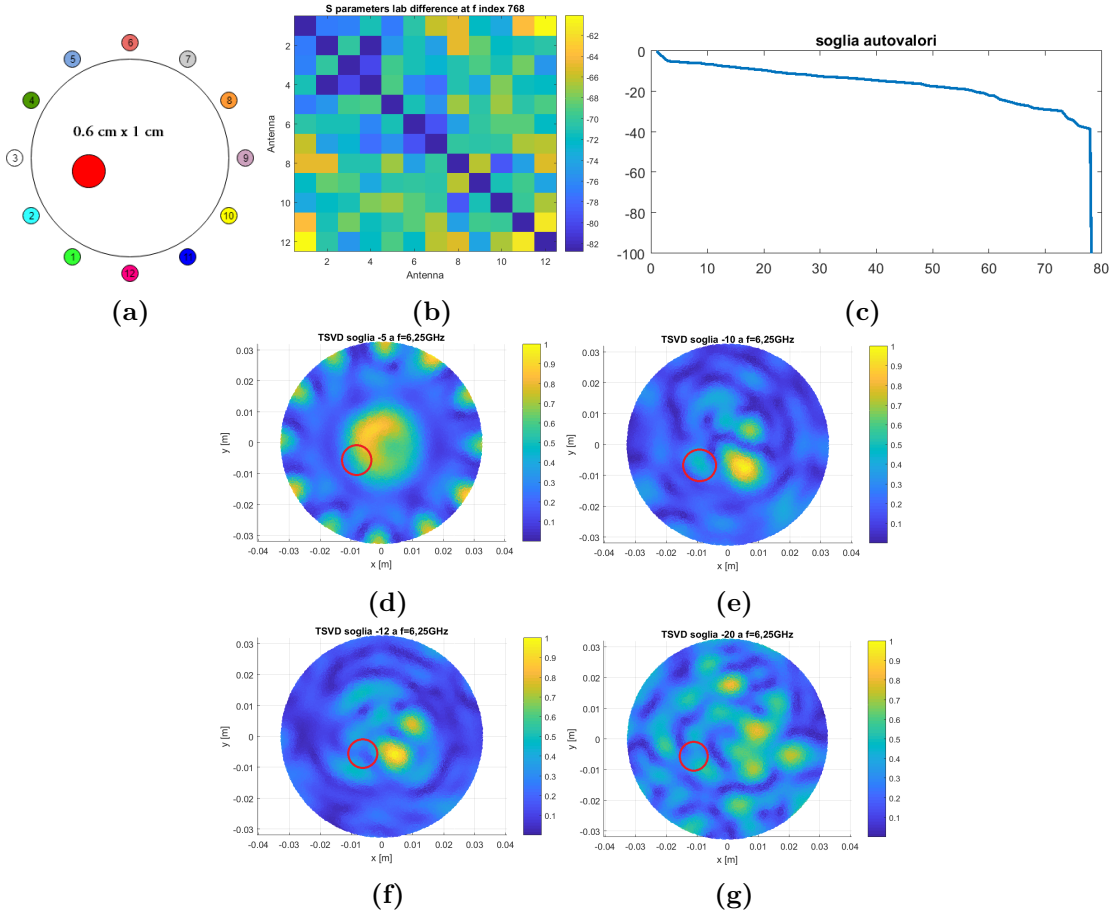

Figure 8.20: Measured TSVD test

Measure results with plastic sample inclusion

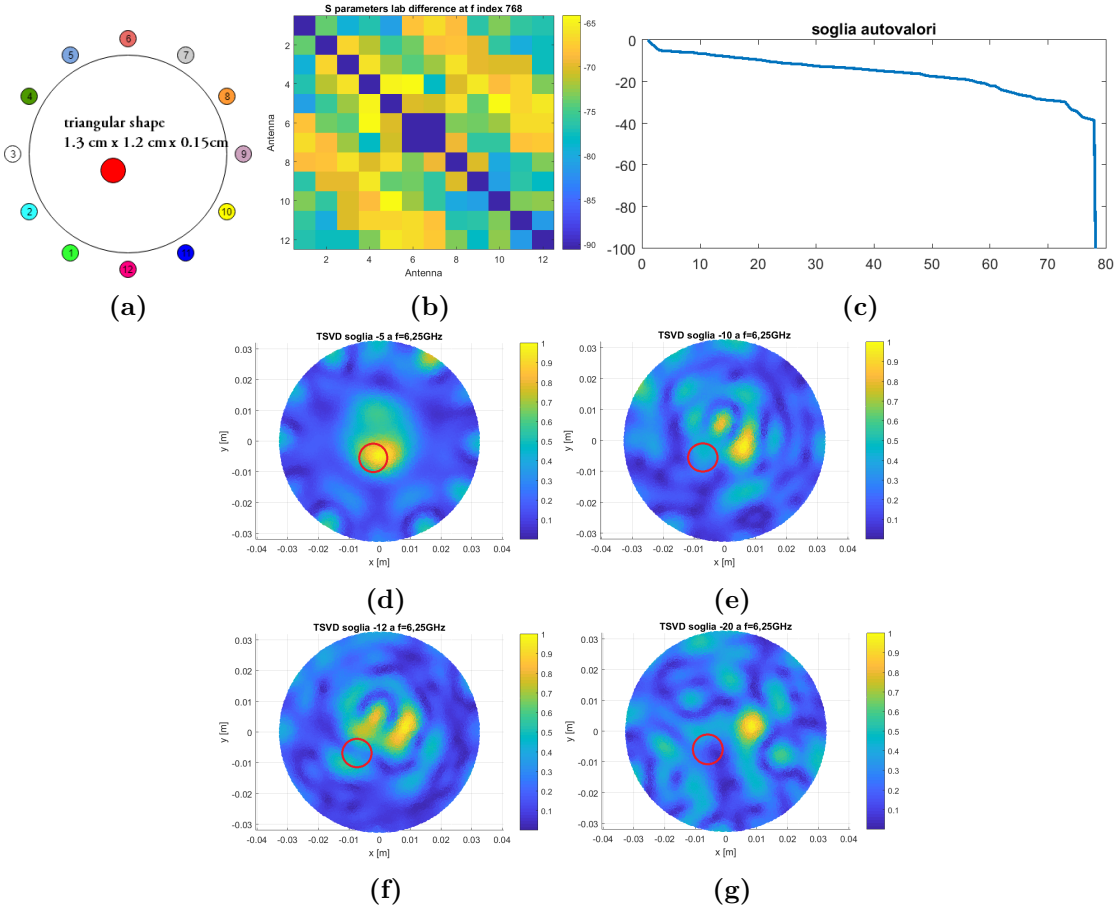

Figure 8.21: Measured TSVD test

8.3.6 Hazelnut cream laboratory test results at 6.75 GHz

At this frequency the antenna S_{11} is $\approx$ -40.1 dB, that ensures correct detection with all cases. This is important to understand that the antenna self scattering parameter is one of the main features to have in order to get a correct and stable detection. Anyway the detection can fails in case of too small inclusion dimensions that are no more compatible with the expected resolution at this frequency. Here the necessity to increase the explored frequency range.

Measure results with cylindrical inclusion

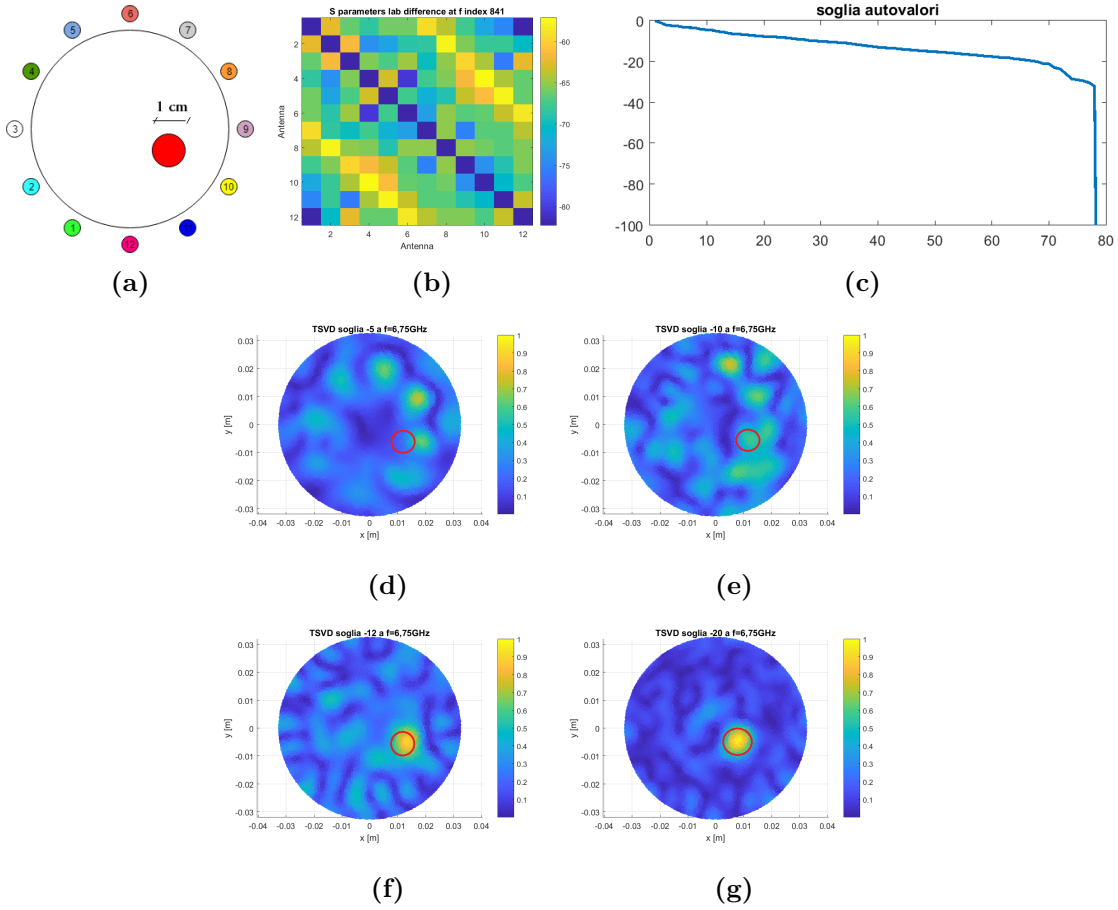

(a) (b) (c)

(d) (e)

(f) (g)

Figure 8.22: Measured TSVD output

Measure results with cylindrical inclusion in a different position

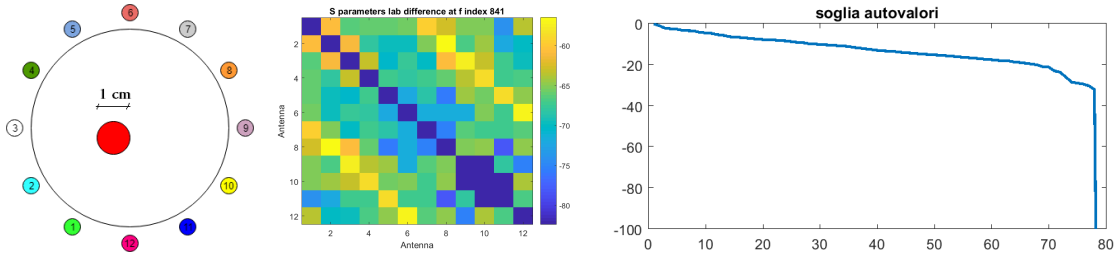

(a) (b) (c)

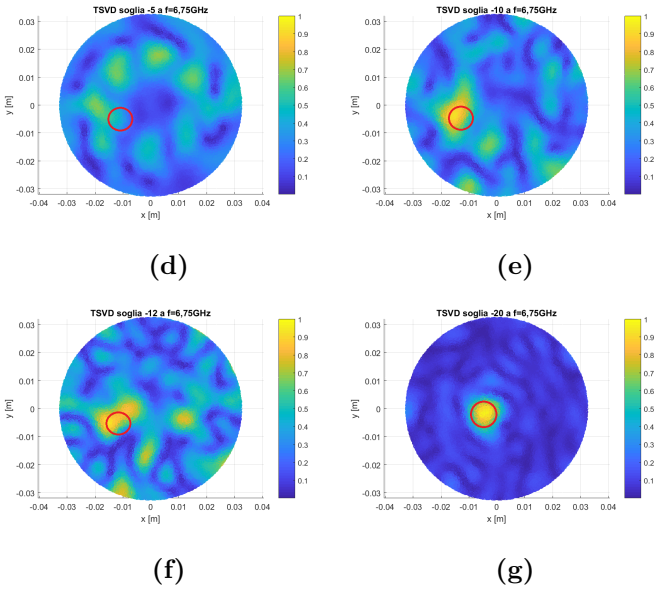

(d) (e)

(f) (g)

Figure 8.23: Measured TSVD output

Measure results with plastic red cup inclusion

Considering the eigenvalue plot of figure (8.23c), the detection is correct around the points before the jumps, where the main informations are contained. After the jump, as the figure (8.24g) show, the detection is loose because the added data information around these threshold values are only noise contributions.

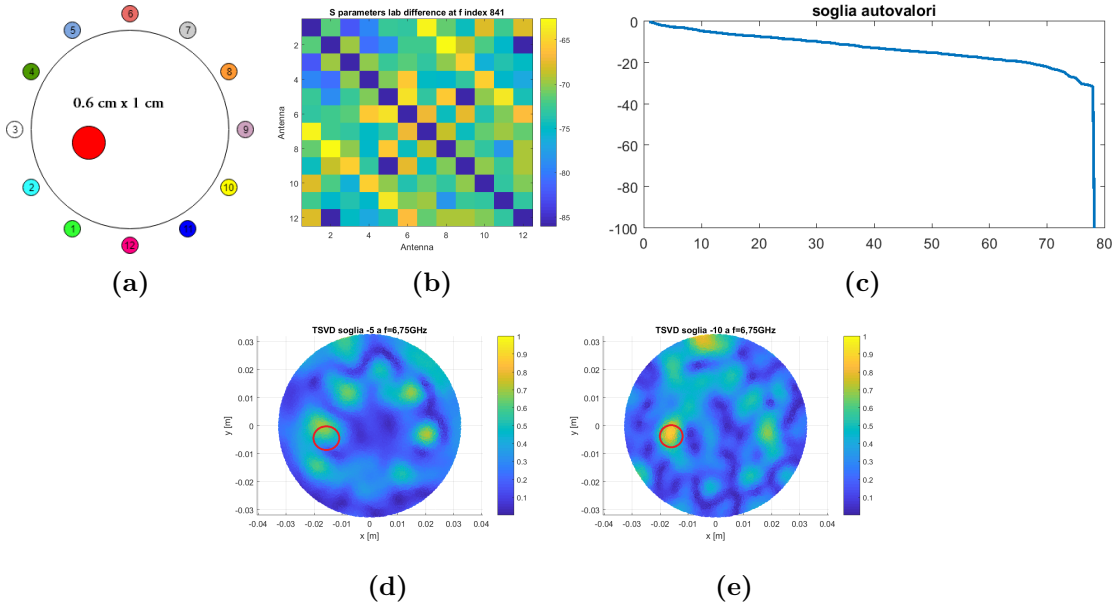

(a) (b) (c)

(d) (e)

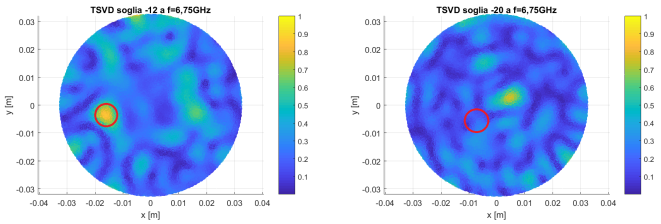

(f) (g)

Figure 8.24: Measured TSVD output

Measure results with plastic sample inclusion

Trying to detect this sample the system gives not so accurate and cleaned results, as figure (8.25) shown.

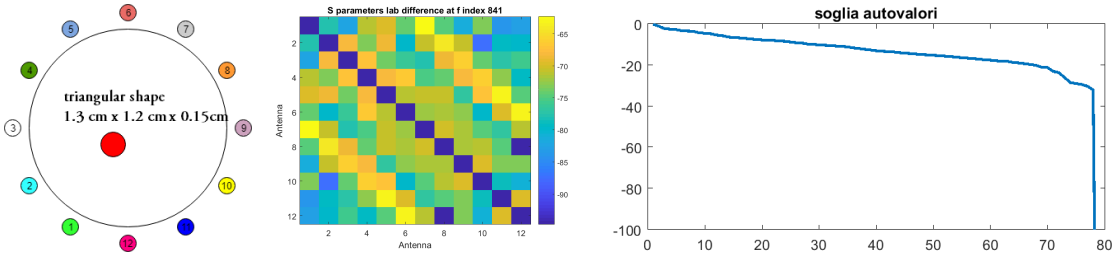

(a) (b) (c)

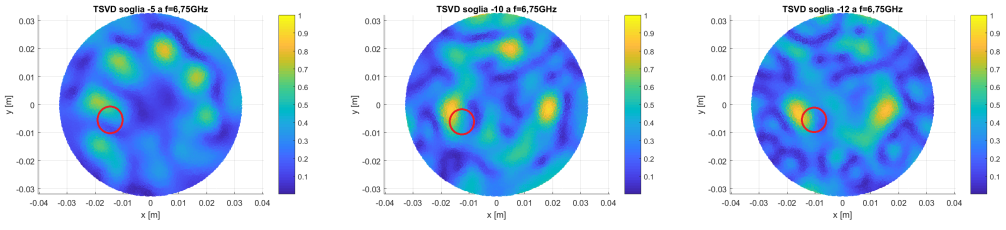

(d) (e) (f)

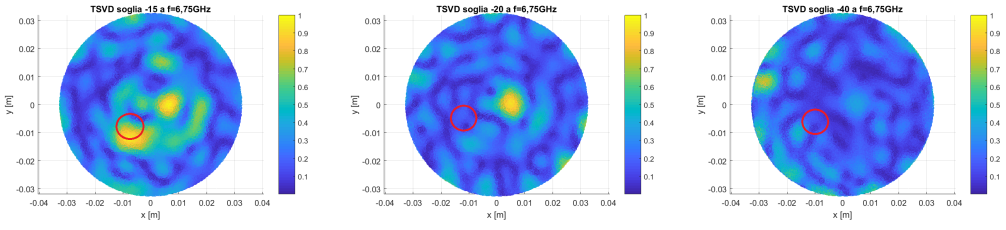

(g) (h) (i)

Figure 8.25: Measured TSVD results

Trying instead a first calibration attempt normalizing the TSVD input using the following rule a bit cleaner output(listed in figure (8.26)) is obtained.

$$\Delta E_s^{norm} = \frac{\Delta E_s}{S_{noObj}} \tag{8.1}$$

Comparing the respective threshold plots, example with fig.(8.26b,8.25e), the detection

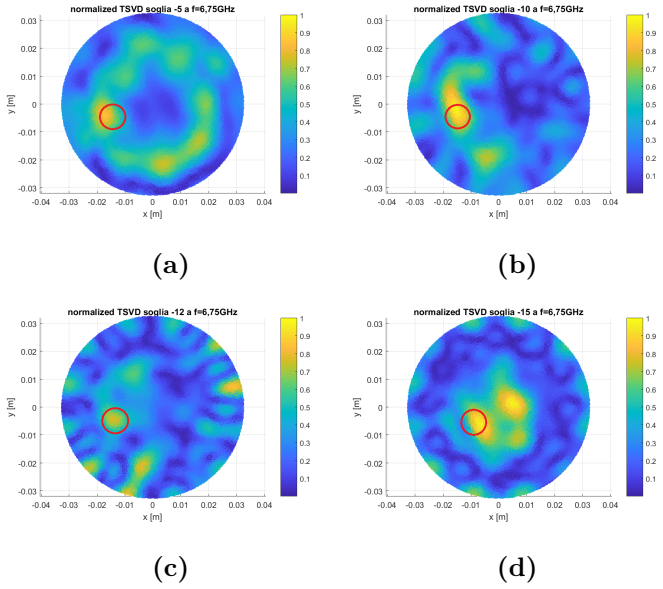

(a) **(b)**

(c) **(d)**

Figure 8.26: Measured TSVD results with normalized input

is quite cleaner and it can be considered a correct one, such as in figure (8.26a). These threshold values are also compatible with the eigenvalues plot (fig.(8.25c)), where after these values only noise is added to the main informations.

8.3.7 Hazelnut cream laboratory test results at 8 GHz

The self scattering parameter of the antenna at 8 GHz is -9.7 dB. So the expected results are worst then the previous case, because the system is now more sensitive to the noise dues to the error into the jar positioning, even if the resolution is increased. So the detection quality depends on right positioning of the jars, that has to be in the same spot for each measurement, in order to not introduce unwanted mismatch on the reconstruction algorithm, that can be the cause of unwanted scatterer reconstructed locations, as for example in figure (8.27). In fact in fig.(8.28), that represents the same inclusion situation, but in a different position, the detection gives nice looking results. Anyway with this S_{11} value, in the harder detection situations, there is the need to increase the frequency on order to increase the resolution.

Measure results with cylindrical inclusion

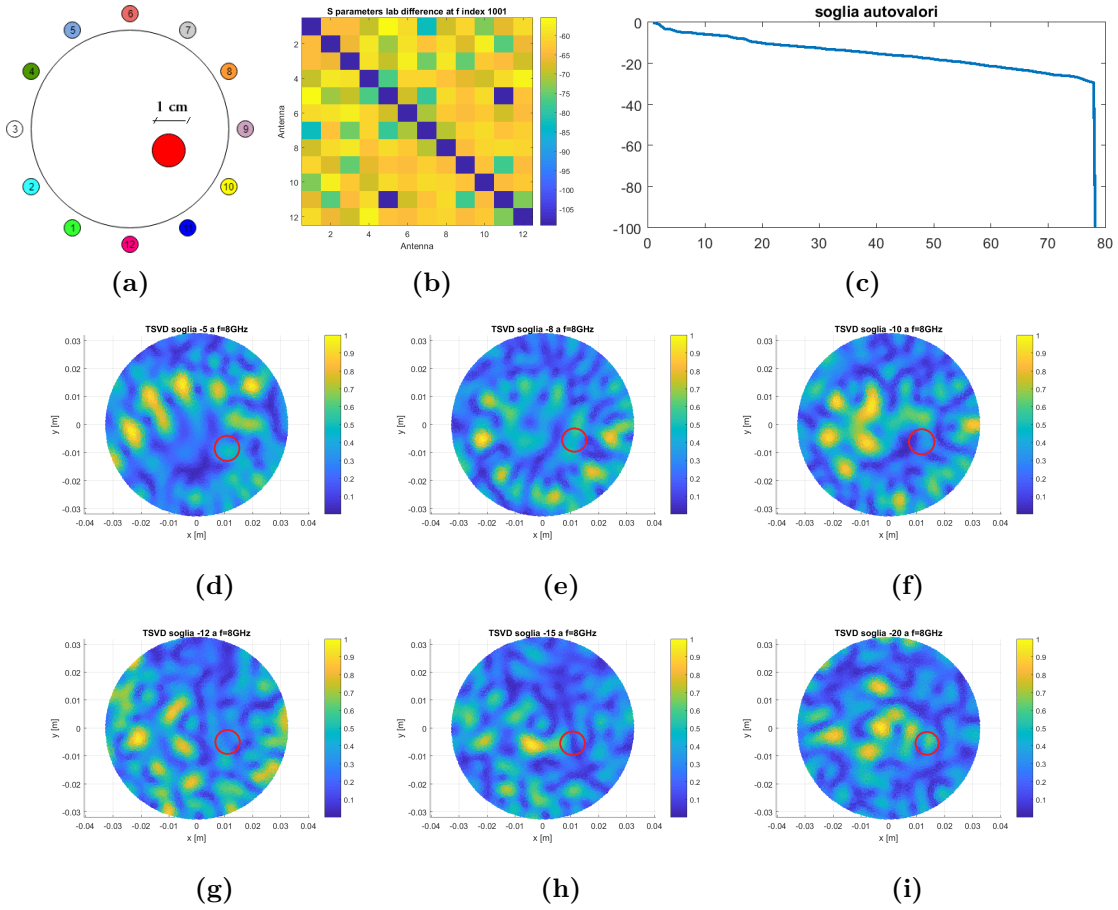

Figure 8.27: Measured TSVD output

Measure results with cylindrical inclusion in a different position

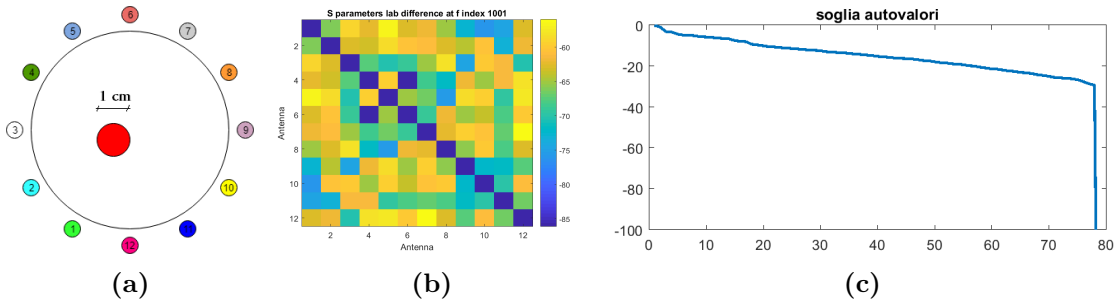

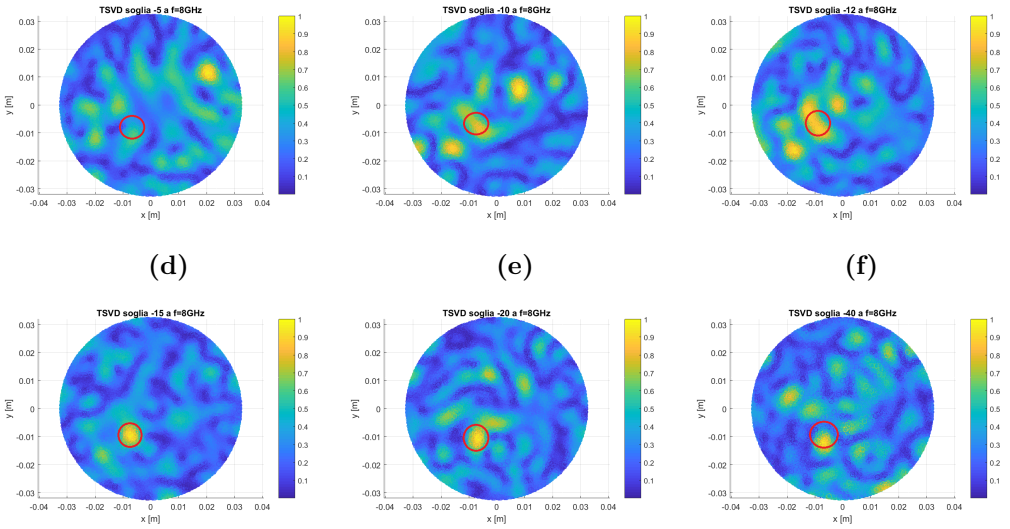

(d) (e) (f)

(g) (h) (i)

Figure 8.28: Measured TSVD output

Measure results with plastic red cup inclusion

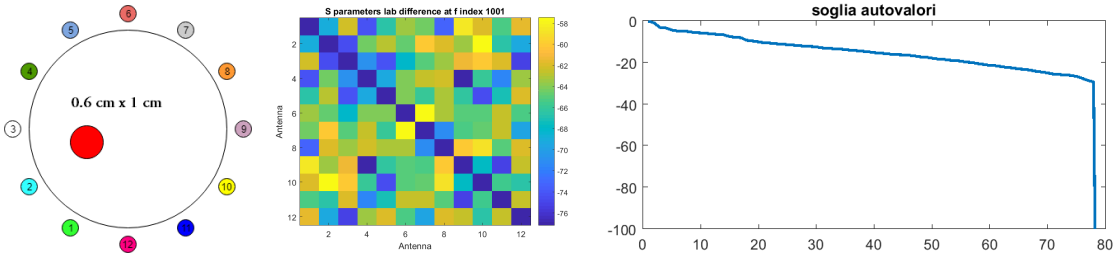

(a) (b) (c)

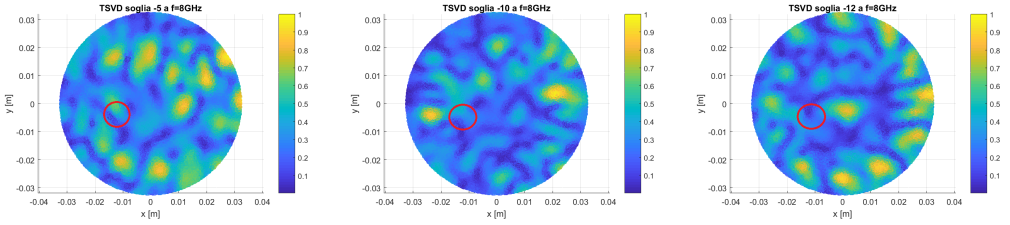

(d) (e) (f)

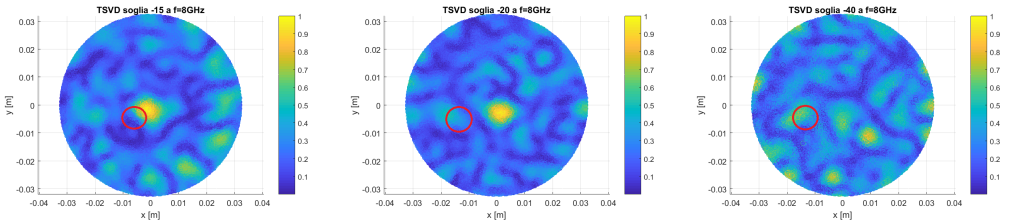

(g) (h) (i)

Figure 8.29: Measured TSVD output

Measure results with plastic sample inclusion

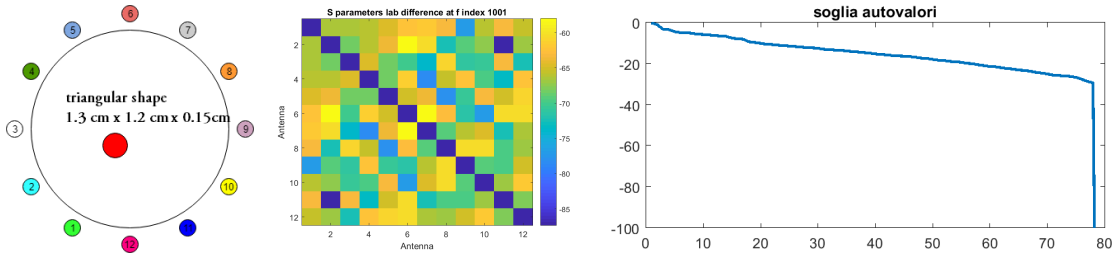

(a) (b) (c)

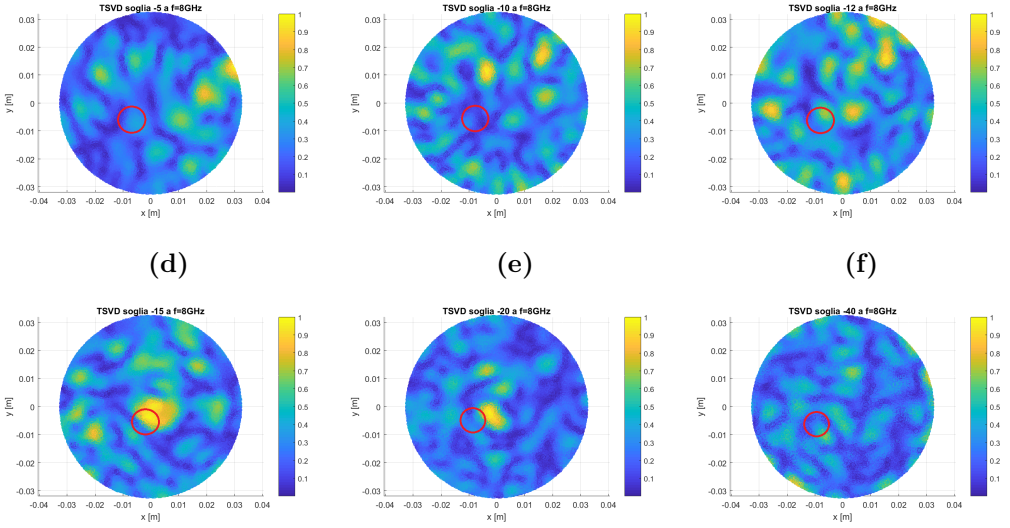

(d) (e) (f)

(g) (h) (i)

Figure 8.30: Measured TSVD output

8.3.8 Ultra wide band monopoles mounted prototype measurements

New measurements are carry out with 6 antennae. Lowering their number can leads to a minor quality on the detections because the system might be more sensitive to the background and jar mismatch position noise. As already made for the prototype with narrow band monopole, the transmission path of near and far antennae can be plotted in order to see if the system "see" something along the path that links the two monopoles. The paths in case of positioned object and its absence are quite different meaning that

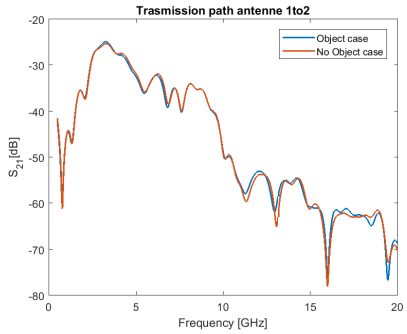

(a) Transmission path between near antennae

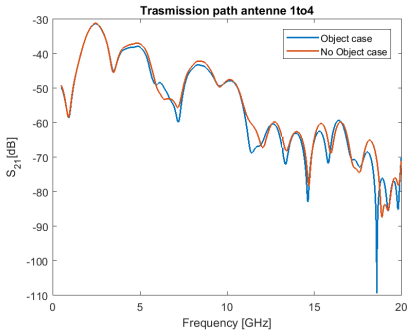

(b) Transmission path between far antennae

Figure 8.31: Transmission path example for cylindrical inclusion

the system detects the variation caused by the intrusion. In the following results the interaction matrix plots aren't reported because considering the low information levels, they are quite useless. In fact the eigenvalue plots show that the relevant informations are entirely confined inside the -8 values, that means poor acquired data. This fact states that the detection for these cases will be probably incorrect. With these antennae the measurement frequency is grown until 11 GHz, optimal value for the detection inside the hazelnut cream. After the mono-frequency TSVD application, to increase the quality of the output detections a multi-frequency TSVD approach is introduced, that uses information data of each involved frequency to get higher informations in order to reconstruct the output image.

8.3.9 Hazelnut cream laboratory test results at 7.75 GHz

Measure results with cylindrical inclusion

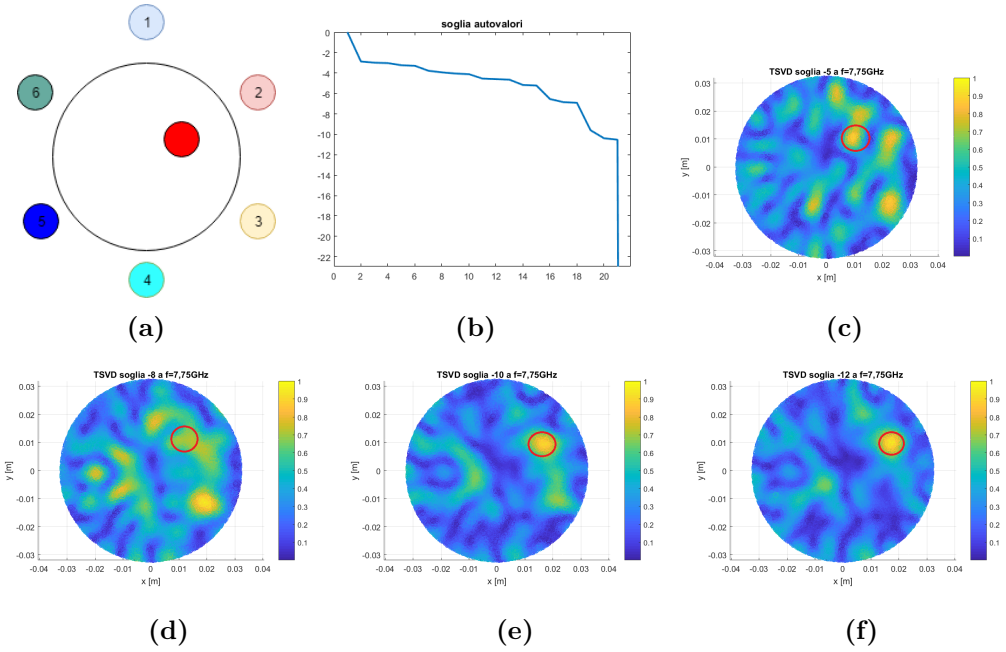

(a) (b) (c)

(d) (e) (f)

Figure 8.32: Measured TSVD output

In this case the detection is quite stable, even though the low available data.

Measure results with cylindrical inclusion in a different position

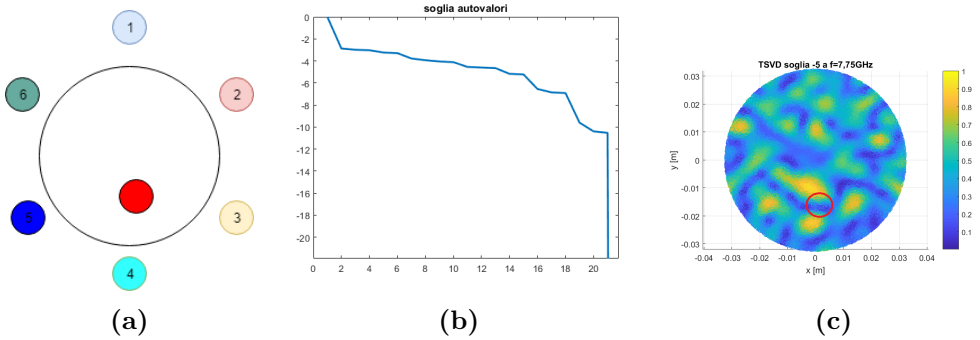

(a) (b) (c)

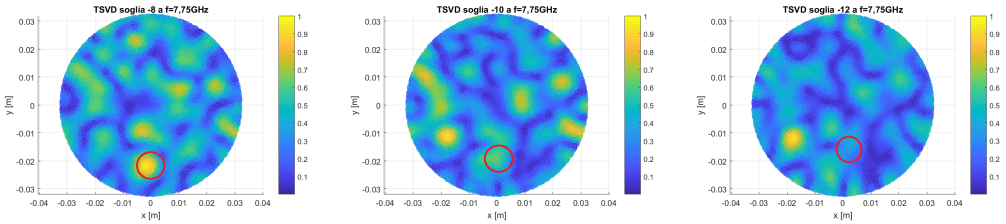

(d) (e) (f)

Figure 8.33: Measured TSVD output

Measure results with plastic red cup inclusion

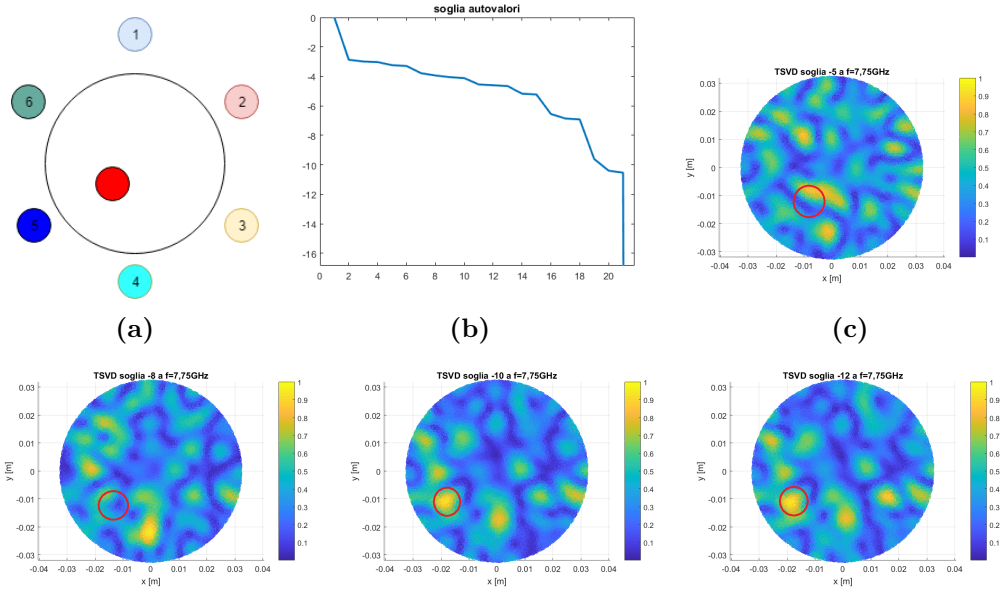

(a) (b) (c)

(d) (e) (f)

Figure 8.34: Measured TSVD output

Measure results with plastic red cup inclusion at different position

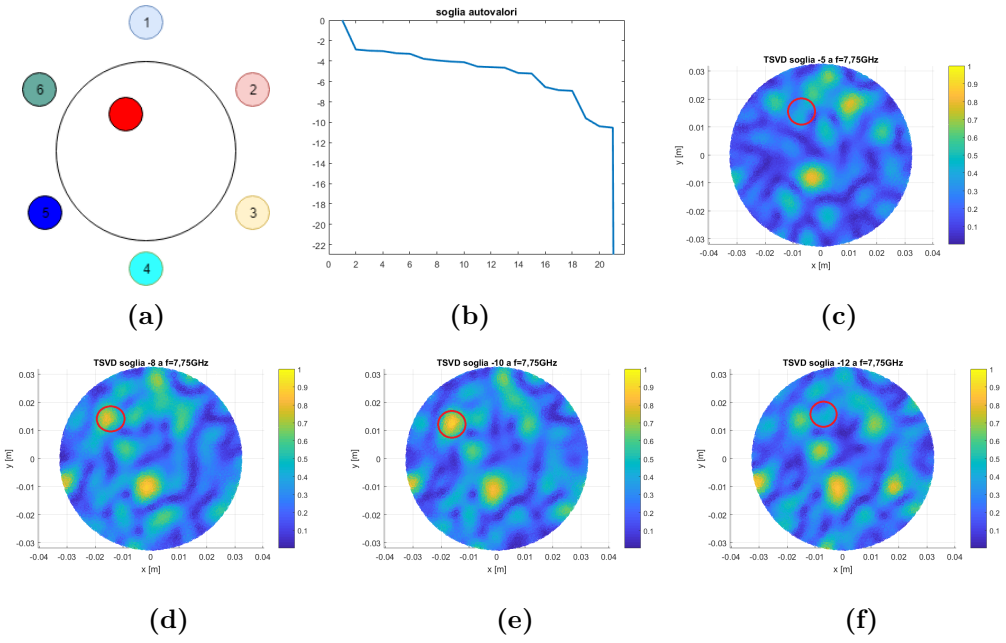

(a) **(b)** **(c)**

(d) **(e)** **(f)**

Figure 8.35: Measured TSVD output

Application of the input calibration

In this section, in order to get better detection results the proposed calibration[14] in section 6.2 is applied on the case in 8.3.9, with the cylindrical inclusion in the first position, using the empty tank scatterer measure as a reference scenario. The quality results increases, but it is present a phantom detection too dues the sub-sampling in the antenna number (as confirmed in Chapter 8.4).
The obtained results underlines the presence of the error dues to the number of the antennae too small. This underlines the need to increase the antennae and their self scattering parameters (S_{11}) in order to get better sensibility.

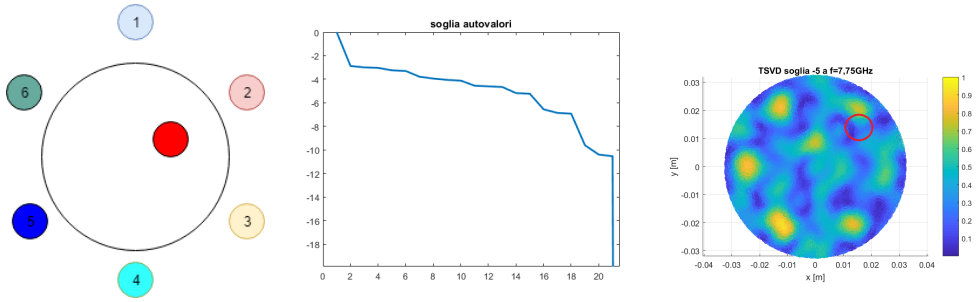

(a) **(b)** **(c)**

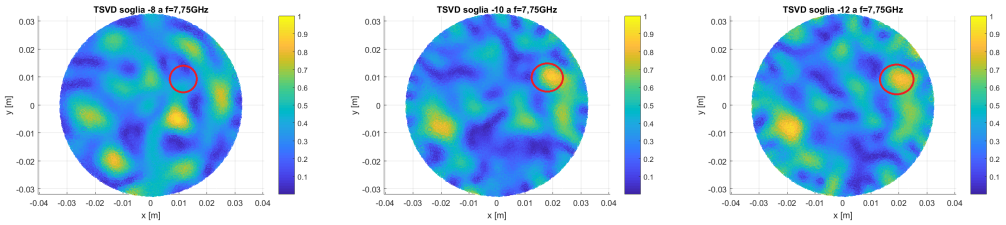

(d) **(e)** **(f)**

Figure 8.36: Measured TSVD output

As already written , the calibration underlines the false detection. Anyway is important to note that every *phantom inclusion* keeps its position on the circumference which radius is defined by the position of the real inclusion.

8.4 Antennae sub-sampling studies

In order to understand the sensibility of the system with the antennae number in the ultra wide band monopoles MWI prototype, two cases between the narrow band monopole situations are considered, that are 8.3.6 and 8.3.7. To be comparable with the UWB monopole number, the antenna are sub-sampling with a step of one antenna distance, in order to select 6 antenna as in the UWB cases. The sub-sampling of antennae was performed reading the collected S parameters, one every one values, saving a 6x6 matrix, instead of a 12x12 one of the original case.
These tests are performed to understand if the inclusion positioning problem encountered in section 8.3.8 are due to a lower number of antennae, which influences the information quantity. Fewer are the antennae, lower is the information acquired leading a possible detected position mismatch.

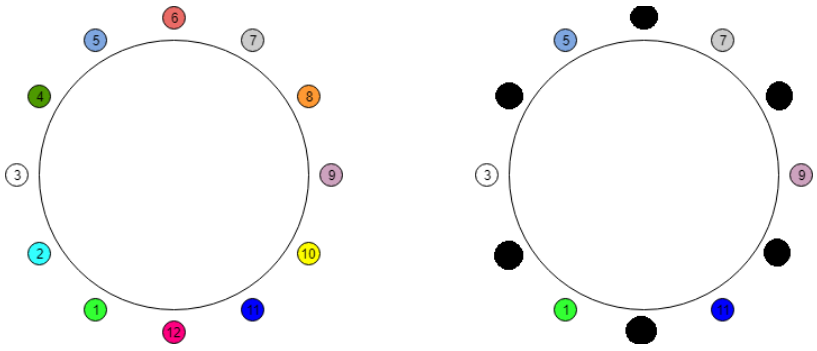

(a) Original 12 antennae positioning

(b) Sub-sampling positioning

Figure 8.37: Antenna positioning before and after the sub-sampling

The results suggest that the low number of considered antennae can lead to positioning errors, since they haven't got a well self scattering parameter at the working frequency.

8.4.1 Hazelnut cream laboratory test results at 6.75 GHz subsampling to 6 antennae

At this frequency the narrow monopoles exhibit S_{11} parameter around -40 dB, that is pretty high, ensuring a correct detection in the 12 antennae case (8.3.6). These results have to be compared to these in section8.3.6, where the detection is correct.
In this case, considering the high S_{11} value, the detection is quite correct, but the decrease

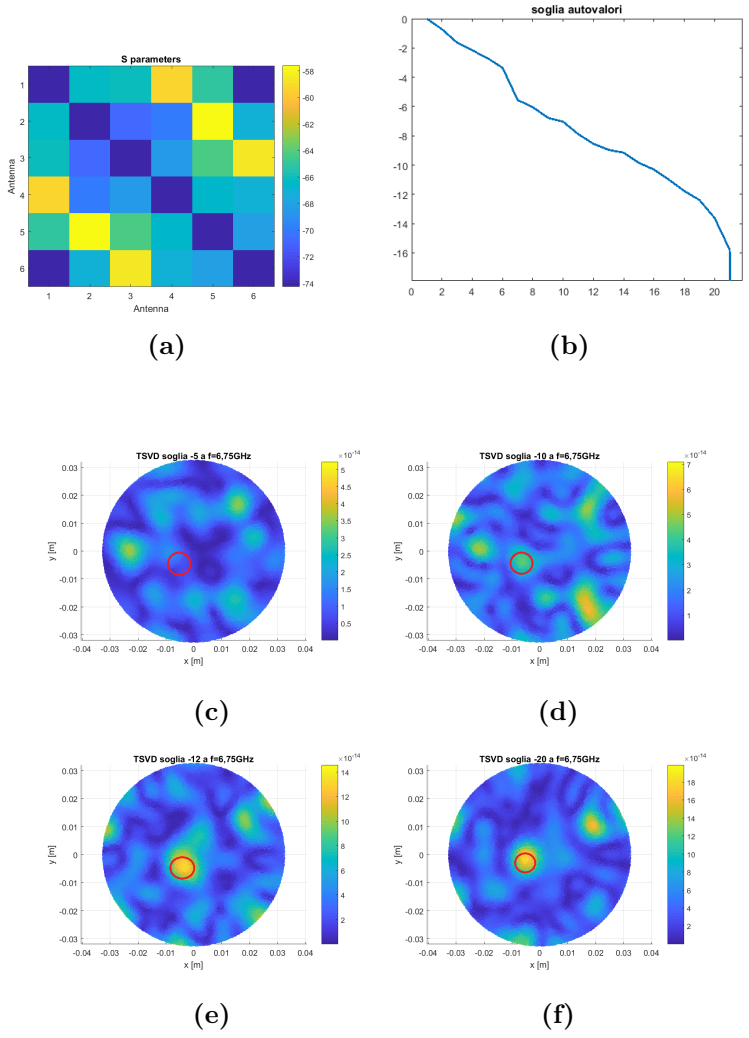

Figure 8.38: Measured TSVD output

of the monopole numbers leads too information looses that will cause the creation of a "phantom" detection at the symmetrical effective position of the inclusion. so this lack of information is the cause of wrong inclusion positioning inside the detection outputs.

8.4.2 Hazelnut cream laboratory test results at 8 GHz sub-sampling to 6 antennae

Here the antenna S_{11} is lower, ≈ -9.7 dB, meaning that the system need more information to get a correct detection. The original case is studied in section 8.3.7, where the detection is correct for higher data information quantities than the previous case.

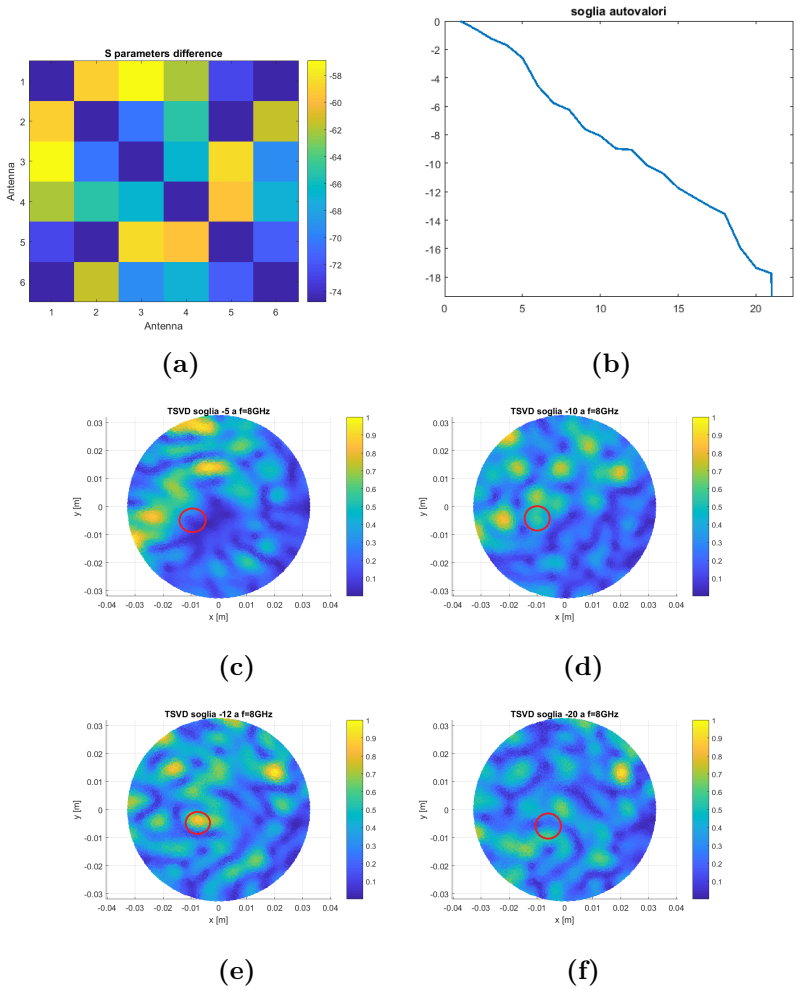

Figure 8.39: Measured TSVD output

Here the lower S_{11} and the lower number of antennae lead to an incorrect detection because the artifact values totally mask the inclusion, that as already written is at the symmetrical position respect to the inclusion.

These results state that in case of low number of antennae, the S_{11} must be much higher to get a well-posed detection.

Chapter 9

Conclusion

The work of this thesis aimed to study the UWB imaging technology in food detection application and three dimensional reconstruction of the target. It is well suited to food safety problems, because it is non-ionizing not producing any related radiation problems, that are typical of other technologies such as X-rays, mains source of the user's complaints about the food and operators safety. Another advantage is in the low cost equipments, that makes this technology suitable of manufacturers interests. To evaluate its capability the entire model was simulated, expanding the explorable frequencies range to increase its sensitivity and accuracy, proposing an ultra wide band antenna. These monopoles were put around the target to collect the scattering parameters, used to solve the inversion problem for the image reconstruction by TSVD, starting from the obtained field from the finite element method propagation problem solving and these measured parameters. The fields inside the target are obtained from a FEM simulation in order to preserve the targets and the non invasive propriety. The presented results state the encouraging capability of the MWI system in case of different situations and inclusions. Finally to validate these simulations, laboratory tests were performed showing promising results, but underlining also the results dependence to the number of considered antenna and target position accuracy, problems that can be overcome using input data calibration methods. In this way the system shows promising results detecting also provided plastic sample as in a real situation of about 1.3 cm x 1.2 cm x 0.15 cm.
Future improvements consist in defining better calibration methods for the input data organizations and trying configurations more suitable for a manufactures production lines.

Appendix A

Reading and selection electromagnetic field code

Here some MATLAB code lines are reported. This code is used to read and select the field region to apply the inversion algorithm to reconstruct the image by TSVD. The code reads the obtained VTK files from the FEM solver. The selection is based on the selected material and barycenter coordinates of the mesh tetrahedrons, points where the detection will be reconstructed. The commented lines, 49 to 51 , are the old used code, based on a "for cycle" to select and calculate the barycenter values. New code, line 38, it is based on the fact that MATLAB is optimized to work with a matrix environment. The new lines have increased the calculation and selection speed of about 80%.

```
1
2  %npoints = ;
3  %ncells = ;
4  %nfiles = ;
5
6  %%data load
7  load('E_Field_ALL.mat')
8  [ncells nfiles] = size(Ex_complex_all);
9  [npoints usl] = size(cells);
10
11 FileName = 'mode.dat';
12 fileID = fopen(FileName,'r');
13
14 tline = fgetl(fileID);
15 tline = fgetl(fileID);
16 tline = fgetl(fileID);
17
18 clear dataaux1
19
20 dataaux1(1:npoints,1:3) = fscanf(fileID,'%f',[3 npoints]).';
21
```

```
verts = dataaux1;

tline = fgetl(fileID);
tline = fgetl(fileID);
tline = fgetl(fileID);

tline = fgetl(fileID);
tline = fgetl(fileID);

clear dataaux1
dataaux1(1:ncells,1:5) = fscanf(fileID,'%f',[5 ncells]).';

elems = dataaux1(:,1:4);
materialElem = dataaux1(:,5);

%%%%%%
barycenter_all(:,:) = (verts(elems(:,1),:)+verts(elems(:,2),:)+verts(elems
    (:,3),:)+verts(elems(:,4),:))/4;
%%%%%%%

%Field selection
 %radius selection
%    radio_cent = sqrt(barycenter_all(:,1).^2 + barycenter_all(:,2).^2);
%Material and z coord selections
selected = find(barycenter_all(:,3) > 0.01 & barycenter_all(:,3) < 0.03 &
    materialElem==2 );

%old code

%     for i=1:size(selected)
%         barycenter_sel(i,:) = (verts(elems(selected(i),1),:)+verts(elems(
    selected(i),2),:)+verts(elems(selected(i),3),:)+verts(elems(selected(i)
    ,4),:))/4;
%
%     end

barycenter_sel = barycenter_all(selected,:);

selected_cells = cells(selected,:);
selected_points = points;


Ex_complex_selected = Ex_complex_all(selected,:);
Ey_complex_selected = Ey_complex_all(selected,:);
Ez_complex_selected = Ez_complex_all(selected,:);

```

```
64
65 save_filename = ['E_Fieldz_slice_selected','.mat'];
66
67 save(save_filename,'Ex_complex_selected','Ey_complex_selected','
       Ez_complex_selected','barycenter_sel','selected_cells','selected_points
       ','-v7.3');
```

Appendix B

False positive test

This appendix describes the false-positive tests, used to understand if the detections are correct or are simply due to errors caused by non ideal behavior of the system.

B.1 Test description

The false positive tests are made using as targets:

- MWI application on the same jar without any inclusions rotating it between the two measures
- MWI application on different jars

These kind of tests are useful to understand if, in case of no foreign object presence inside the jar, the system will give a correct "clean jar" detection, since the detected values, dues to the jars differences, are around the noise level. Example of jars difference must be searched inside the position inaccuracy, different food content quantities that can lead to some unwanted scatterer region, which the algorithm might consider as an inclusion. The problem rise when this false detection obscures the real one or, if not present, signals a detection, when it doesn't be.

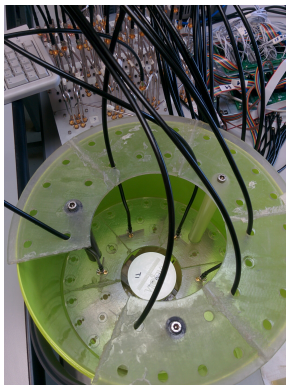

Figure B.1: False positive laboratory test

B.2 Results

B.2.1 Same jar

Here the same jar measures taken at different time are considered. As the figure (B.2) shows the MWI reveals some artifacts that can be caused by differences between each antennae, non ideal components and noise background. By the way its levels are around 10^{-10} that is at least one, two order of magnitude lower than a correct detection values.

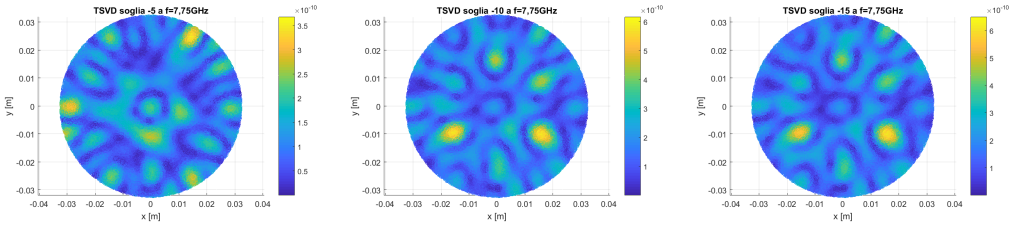

(a) **(b)** **(c)**

Figure B.2: TSVD output example in a false positive test with the same considered jar

B.2.2 Different jars

In this case two different jars are considered in order to be closer to a real situation, where different pots are investigated. Also in this case the "detected" artifacts have levels around the $10^{-9} \div 10^{-10}$

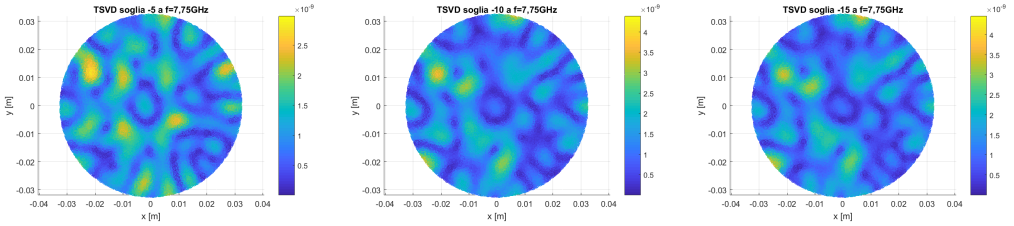

(a) **(b)** **(c)**

Figure B.3: TSVD output example in a false positive test with different jars

The two results in figures (B.2 and B.3) show that the MWI system is characterized by robustness against unwanted noise detection.

Appendix C

Three dimensional reconstruction

The MWI presented results can be three dimensional reconstructed via MATLAB script, reported below, used to make readable the TSVD results from a 3D viewer, Paraview.

To demonstrate the well suited 3D visualization the entire jar reconstruction is made using the output obtained in 8.3.7, in particularly at 8.30h.

The reconstruction are shown in figures (C.1).

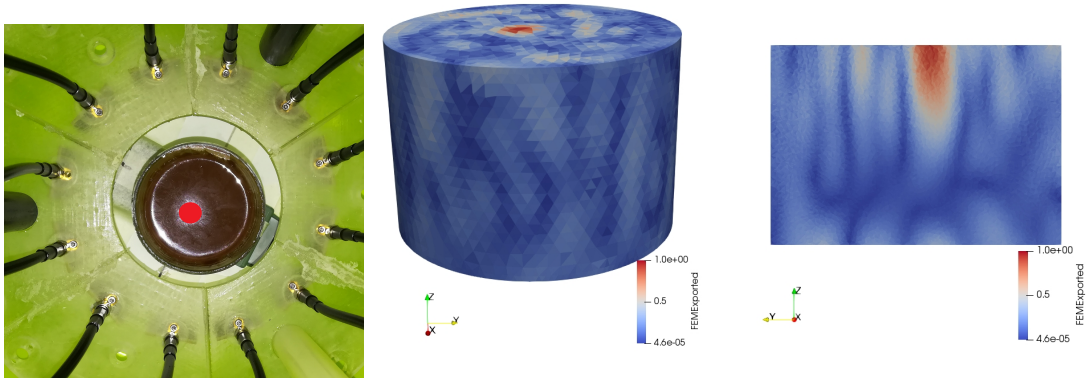

(a) View of jar set-up **(b)** View of the entire jar **(c)** X cut of the jar

Figure C.1: Reconstruction example

In the plot is clearly visible the maximum dues to the inclusion presence, that represents exactly the TSVD output. Anyway the inclusion shape accuracy depends from the information acquired by the TSVD, that is conditioned by the number of considered antenna. So In case where their number is low the inclusion shape will be not defined in a clearly way, but only a maximum range values region will be displayed.

```
1
2  % close all;
3  clear all;
4  % clc;
5
6  %input data
7  fileID = load('field');
8  filename = 'E.vtk'; %VTK ooutput
9
10 [ncells nfiles] = size(fileID.Ez_complex_selected);
11 [npoints usl] = size(fileID.selected_points);
12
13 fid = fopen(filename, 'w');
14 % VTK files contain five major parts
15 % 1. VTK DataFile Version
16 fprintf(fid, '# vtk DataFile Version 3.0\n');
17 % 2. Title
18 fprintf(fid, 'Ez_slice.vtk from Matlab\n');
19 % ASCII
20 fprintf(fid,'ASCII\n');
21 fprintf(fid,'\n');
22 %POINTS
23 fprintf(fid, 'DATASET UNSTRUCTURED_GRID\n');
24 fprintf(fid, ['POINTS ' num2str(npoints) ' double\n']);
25
26 coord(1:npoints,1:3) = fileID.selected_points(1:npoints,1:3);
27 fprintf(fid,'%f %f %f\n',coord');
28 fprintf(fid,'\n');
29
30 %CELLS  clm=4 + 1 mesh type cell – tetrahedron
31 tmp=sprintf('%d %d',ncells,ncells*5);
32 fprintf(fid, ['CELLS ' num2str(tmp) '\n']);    %numero celle   dim matrice
33 tip(1:ncells,1:1)=4;
34 tip(1:ncells,2:5) = fileID.selected_cells(1:ncells,1:4);
35 fprintf(fid,'%d %d %d %d %d\n',tip');   %
36
37 fprintf(fid,'\n');
38
39 %CELL_TYPES
40 fprintf(fid, ['CELL_TYPES ' num2str(ncells) '\n']);    %cells number
41 teen(1:ncells,1:1) = 10;
42 fprintf(fid,'%d\n',teen');
43 fprintf(fid,'\n');
44
45 %CELL_DATA
```

```
46 fprintf(fid, ['CELL_DATA ' num2str(ncells) '\n']);
47 fprintf(fid, ('SCALARS FEMExported double\n'));
48 fprintf(fid, ('LOOKUP_TABLE default\n'));
49
50 fileID2 = load('TSVDoutput.mat'); %TSVD output load
51 E_output = fileID2.RI;
52
53 field(:,1) = fileID2.RI;
54 fd=abs(field./max(field));
55 fprintf(fid,'%d\n',fd);                                    %format
56
57 disp('VTK antenna created')
58
59 fclose('all');
```

Bibliography

[1] Stephen F. Adam. *Microwave Theory and Applications*. Prentice Hall, 1969.

[2] Sultan Almazroui. *Microwave imaging for security applications*. PhD thesis, University of Sussex, November 2015.

[3] Greg Amorese. Lcr / impedance measurement basics.

[4] Constantine A. Balanis. *Advanced Engineering Electromagnetics*. Wiley, 1989.

[5] H. L. Berman and G. F. Warnke. Use of infrared techniques in industrial instrumentation. *IRE Transactions on Industrial Electronics*, PGIE-11:15–20, Dec 1959.

[6] M. R. Casu, M. Vacca, J. A. Tobon, A. Pulimeno, I. Sarwar, R. Solimene, and F. Vipiana. A cots-based microwave imaging system for breast-cancer detection. *IEEE Transactions on Biomedical Circuits and Systems*, 11(4):804–814, Aug 2017.

[7] Quansheng Chen, Chaojie Zhang, Jiewen Zhao, and Qin Ouyang. Recent advances in emerging imaging techniques for non-destructive detection of food quality and safety. *TrAC Trends in Analytical Chemistry*, 52:261 – 274, 2013. Modern Food Analysis and Foodomics.

[8] CIMNE. Gid the personal pre and post processor. `https://www.gidhome.com/`. Accessed: 2017-12-12.

[9] confructa medien GmbH FRUIT PROCESSING magazine. Fruit-processing. `https://www.fruit-processing.com/`. Accessed: 2017-12-12.

[10] Robert W. Cootney. Ultrasound imaging: Principles and applications in rodent research. *ILAR Journal*, 42(3):233–247, 2001.

[11] Ashim K. Datta. *Handbook of Microwave Technology for Food Application (Food Science and Technology)*. CRC Press, 2001.

[12] M Edwards. *Detecting foreign bodies in food*. CRC Press, 04 2004.

[13] Food Standards Scotland (FSS) Food Standards Agency (FSA). Annual report of incidents. `https://www.food.gov.uk/about-us/data-transparency-accounts/busreps/miscbusrep`. Accessed: 2017-12-12.

[14] C. Gilmore, P. Mojabi, A. Zakaria, M. Ostadrahimi, C. Kaye, S. Noghanian, L. Shafai, S. Pistorius, and J. LoVetri. A wideband microwave tomography system with a novel frequency selection procedure. *IEEE Transactions on Biomedical Engineering*, 57(4):894–904, April 2010.

[15] Mark Graves, Alex Smith, and Bruce Batchelor. Approaches to foreign body detection in foods. *Trends in Food Science and Technology*, 9(1):21 – 27, 1998.

[16] Bhag Singh Guru and Hüseyin R. Hiziroglu. *Electromagnetic Field Theory Fundamentals*. Cambridge University Press, 2004.

[17] Ana M. Herrero. Raman spectroscopy a promising technique for quality assessment of meat and fish: A review. *Food Chemistry*, 107(4):1642 – 1651, 2008.

[18] B. B. Hu and M. C. Nuss. Imaging with terahertz waves. *Opt. Lett.*, 20(16):1716–1718, Aug 1995.

[19] National Instruments. Introduction to network analyzer measurements, fundamentals and background.

[20] Princeton Instruments. Raman spectroscopy basics.

[21] Jian-Ming Jin. *Theory and Computation of Electromagnetic Fields*. Wiley-IEEE Press, 2010.

[22] Jianming Jin. *The Finite Element Method in Electromagnetics*. Wiley-IEEE Press, 3rd edition, 2014.

[23] V. Klema and A. Laub. The singular value decomposition: Its computation and some applications. *IEEE Transactions on Automatic Control*, 25(2):164–176, Apr 1980.

[24] Mathworks. Matlab. `https://it.mathworks.com/`. Accessed: 2017-12-12.

[25] MiBraScan. Mibrascan - microwave brain scanner for cerebrovascular diseases. `https://mibrascan.polito.it/`. Accessed: 2017-12-12.

[26] Micenea. Micenea - microwave imaging for combined early diagnostics of breast cancer. `http://www.micenea.it/`. Accessed: 2017-12-12.

[27] Peter Monk. *Finite Element Methods for Maxwell's Equations (Numerical Analysis and Scientific Computation Series)*. Clarendon Press, 2003.

[28] Sandeep Kumar Palaniswamy, Malathi Kanagasabai, Shrivastav Arun Kumar, M. Gulam Nabi Alsath, Sangeetha Velan, and Jayaram Kizhekke Pakkathillam. Super wideband printed monopole antenna for ultra wideband applications. *International Journal of Microwave and Wireless Technologies*, 9(1):133–141, 2017.

[29] Paraview. Paraview. `https://www.paraview.org/`. Accessed: 2017-12-12.

[30] S. Ryynänen. The electromagnetic properties of food materials: A review of the basic principles. *Journal of Food Engineering*, 26(4):409 – 429, 1995.

[31] R. Scapaticci, O. M. Bucci, I. Catapano, and L. Crocco. Robust microwave imaging for brain stroke monitoring. In *2013 7th European Conference on Antennas and Propagation (EuCAP)*, pages 75–78, April 2013.

[32] R. Scapaticci, O. M. Bucci, I. Catapano, and L. Crocco. Differential microwave imaging for brain stroke followup. *International Journal of Antennas and Propagation*, 2014:1–11, 2014.

[33] Rosa Scapaticci, Loreto Di Donato, Ilaria Catapano, and Lorenzo Crocco. A feasibility study on microwave imaging for brain stroke monitoring. *Progress In Electromagnetics Research B*, 40:305–324, 2012.

[34] O. Schimmer, F. Daschner, and R. Knochel. Uwb-sensors in food quality management; the way from the concept to market. In *2008 IEEE International Conference on Ultra-Wideband*, volume 2, pages 141–144, Sept 2008.

[35] J. D. Shea, B. D. Van Veen, and S. C. Hagness. A tsvd analysis of microwave inverse scattering for breast imaging. *IEEE Transactions on Biomedical Engineering*, 59(4):936–945, April 2012.

[36] Errede Steven. Elementary microscopic theory of dielectrics - lecture notes 12, 2007.

[37] CTS STUDIO SUITE. Cts studio suite. `https://www.cst.com/`. Accessed: 2017-12-12.

[38] Richard Syms and John Cozens. *Optical Guided Waves and Devices*. McGraw-Hill, 1992.

[39] Agilent Technologies. Network analyzer basics.

[40] O. V. Tereshchenko, F. J. K. Buesink, and F. B. J. Leferink. An overview of the techniques for measuring the dielectric properties of materials. In *2011 XXXth URSI General Assembly and Scientific Symposium*, pages 1–4, Aug 2011.

[41] Bo Thide. *Electromagnetic Field Theory*. Dover Pubns, 2011.

[42] J. A. Tobon V., E. A. Attardo, G. Dassano, F. Vipiana, M. R. Casu, M. Vacca, A. Pulimeno, and G. Vecchi. Design and modeling of a microwave imaging system for breast cancer detection. In *2015 9th European Conference on Antennas and Propagation (EuCAP)*, pages 1–2, May 2015.

[43] J. A. T. Vasquez, F. Vipiana, M. R. Casu, M. Vacca, and A. Pulimeno. Microwave imaging for early breast cancer detection: Experimental testing of a low-cost portable system. In *2016 IEEE International Symposium on Antennas and Propagation (APSURSI)*, pages 1479–1480, June 2016.

[44] D.R. Wilton. Chapter 1.5.5 - computational methods. In Roy Pike and Pierre Sabatier, editors, *Scattering*, pages 316 – 365. Academic Press, London, 2002.

[45] François ZUBER. Détection des corps étrangers dans les produits alimentaires. *Techniques de l'ingénieur Agroalimentaire : risques, sécurité, qualité et environnement*, base documentaire : TIB427DUO.(ref. article : f1210), 2007. fre.